EXERGY ANALYSIS OF A PULSE DETONATION ENGINE LINEAR POWER GENERATOR

by

ABDULRAHEEM TEMITOPE BELLO

Presented to the Faculty of the Graduate School of

The University of Texas at Arlington in Partial Fulfillment

of the Requirements

for the Degree of

DOCTOR OF PHILOSOPHY

THE UNIVERSITY OF TEXAS AT ARLINGTON

May 2016

Dedicated to Musilimot Ogunbambi.

Acknowledgements

First of all, I would like to thank Prof. Frank Lu, for his guidance, patience, kindness, and the opportunity to work at the Aerodynamics Research Center. For helping me to grow as an individual and as a research scientist. I would like to thank Prof. Donald Wilson for introducing me into the ARC family, and for supporting my Master's research. I would like to thank Prof. Daejong Kim, for his helpful insights on how to improve the systems analysis component of my research. I would like to thank Prof. Hyejin Moon, for helpful conversations about my research's thermodynamic analysis. I would also like to thank Prof. Rasool Kenarangui, for providing me with more background on electrical systems analysis component of my research.

I greatly appreciate the technical staff of the Mechanical and Aerospace Department, who helped make this work possible. I would like to thank David Carter for helping me ensure that my experiments were conducted safely. I would also like to thank Kermit Beird and Sam Williams in the Woolf Hall Machine Shop, who machined critical components for my experiment, and were always willing to help make modifications on short notice.

I would like to thank Ricardo Jamaica, Bryan Lucas, Robert Warwick, Steven McDonald and Gilberto Olvera the undergraduate LSAMP students who worked with me over the years to build my experimental setup. I would like to thank the entire ARC family who were always willing to lend a helping hand to move heavy equipment, and were accommodating of my experiments in our shared laboratory space.

I would like to thank the University of Texas at Arlington's Office of Technology Management for supporting my research with an award from the Technology Acceleration Program (TAP) fund sponsored by the National Institute of Standard and Technology (NIST) and the Technology Manufacturing Extension Manufacturing Partnership. I would also like to thank UTA administrators for supporting and allowing me to pursue my entrepreneurial efforts.

Finally, I would like to thank my friends and family; my parents for being so supportive and encouraging in all my endeavors, and my brothers for always keeping me grounded. Alhamdulillahi!

April 29, 2016

Abstract

EXERGY ANALYSIS OF A PULSE DETONATION ENGINE

LINEAR POWER GENERATOR

AbdulRaheem T. Bello, PhD

The University of Texas at Arlington, 2016

Supervising Professor: Frank Lu

The fuel efficiency of a power generator is a key metric for evaluating its performance. The common engineering practice is to determine the thermal efficiency of the system by applying the conservation of energy also known as the first law of thermodynamics. However, for heat engine power generators, and other thermal systems, the thermal efficiency is not sufficient for detailed system performance analysis. Exergy analysis, which applies both the first and second law of thermodynamics, enables the determination of the directionality of thermal processes, and the system's available work. This more complete thermodynamic analysis approach is applied to a pulse detonation engine coupled to a linear power generator which is abbreviated as PDE-LPG.

Analytical and experimental studies of a pulse detonation engine (PDE) were performed focused on power generation. Analytical studies include the development of a one-dimensional model based on the wave processes in a cycle of the PDE, to elucidate its performance during operation in the fully- and partially-filled mode. A novel thermodynamic cycle is developed to describe the operation and performance of the PDE-

LPG. The energy and exergy efficiency of the proposed PDE-LPG cycle is compared to the efficiencies of the Brayton, Otto, Diesel, and ZND cycles.

An experimental facility was developed to demonstrate the operation of a PDE with a linear power generator. A diverging nozzle and a piston-spring system were designed and installed at the PDE exit to accelerate the exhaust products, and to improve the transmission of gas momentum to the generator. These components were integrated to produce electrical power. The results of the PDE's specific impulse, nozzle performance, and generator current and voltage were measured. The chemical, thermal, mechanical, and electrical energy across each subcomponent was measured, and the energy and exergy efficiencies of the experimental PDE-LPG facility are presented.

ENTREPRENEURIAL EFFORTS AND CONFLICT OF INTEREST STATEMENT

In conjunction with my doctoral work, I have formed and incorporated a start-up company named Afthon, which is commercializing detonation-based power generators related to my doctoral work. This startup has achieved moderate success. In the spring of 2014, Afthon was selected to compete in the prestigious Rice University Business Plan Competition. In spring 2015, Afthon competed in several business plan competitions including the ASME-ISHOW, the Next Play venture tournament at Davidson College, the Resnick Institute's FLoW competition, MIT's Clean Energy Prize, and UT Austin's Global Venture Labs Investment Competition. The Afthon team was selected as one of the Kairos Society's 2014 50 emerging entrepreneurs. In March 2015, I represented the Afthon team at the Stu Clark Investment Competition in Winnipeg Canada, and won second place in the logo pitch competition.

Afthon has received Stage 1 and Stage 2 grants from VentureWell totaling $25,000 that were awarded to the University of Texas Arlington (UTA) as well as the final Stage 3 grant. In spring 2016, this startup company also received a $50,000 NSF I-CORPS grant that was awarded to UTA. My doctoral work was not funded by Afthon, but was partly funded through a grant from UTA's Technology Acceleration Program mentioned in the acknowledgements section.

In 2014, a conflict of interest (COI) management plan was established for all members of Afthon with ties to UTA. This plan was reviewed and endorsed by UTA's COI committee. The COI plan is reviewed annually and managed by UTA's Director of Regulatory Services through the Office of Research Administration. My COI plan

endorsed by the COI committee requires that my doctoral committee be notified of these entrepreneurial activities related to my doctoral work.

TABLE OF CONTENTS

LIST OF ILLUSTRATIONS

LIST OF TABLES

Table Page

Nomenclature

a	=	sound speed
A	=	area
BWR	=	back work ratio
c_P	=	specific heat at constant pressure
c_v	=	specific heat at constant volume
e	=	internal energy
f	=	fuel-air ratio
ff	=	fill fraction
$\vec{F}$	=	force
g	=	acceleration due to gravity
h	=	enthalpy
h_{PR}	=	fuel lower heating value
I	=	current
j	=	mass flux density
L	=	length
LHV	=	Lower Heating Value
M	=	Mach number
p	=	pressure
P	=	power
$\tilde{q}$	=	specific heat
Q	=	heat
QF	=	quality factor
r	=	compression ratio
r_c	=	cutoff ratio
R	=	gas constant
R^2	=	regression fit value
s	=	specific entropy
S	=	entropy
t	=	time
T	=	temperature
u	=	velocity
V	=	voltage
W	=	work
x	=	displacement
z	=	vertical displacement
γ	=	specific heat ratio
ζ	=	damping ratio
η	=	efficiency
μ	=	chemical potential
ν	=	specific volume

ξ	=	specific exergy
Ξ	=	exergy
ρ	=	density
χ	=	specific exergy destruction
ω_n	=	natural frequency

Subscripts

0	dead state
1,a	initial states
2	compressor exit
3	turbine inlet
4	turbine exit
act	actual value
avg	average value
CJ	Chapman-Jouguet
ch	chemical
E	electrical
Flow	flow work
is	isentropic value
ME	mechanical
rev	reversible
rms	root mean square
s	static
t	thermal
U	internal energy
I	first law
II	second law

Superscripts

*	choked flow condition

CHAPTER 1

Introduction

1.1 Motivation

Detonation engines have been investigated due to their higher cycle performance in comparison to their deflagration counterparts [1]. The primary distinction in the nature of detonation combustion in contrast to deflagration combustion is the presence of a shockwave. This shockwave compresses the fuel-oxidizer mixture very rapidly allowing a detonation to release the same amount of internal energy similar to a deflagration, but at a higher pressure and temperature. Previous investigators have shown that the energy and exergy efficiencies of detonation-based heat engine cycles are over 20% better than their deflagration counterparts for equivalent initial pre-compression [2]. This raises the question: can a detonation-based power generator be developed to demonstrate the predicted higher first- and second-law efficiencies?

In addition, detonation engines have been proposed for aerospace air-breathing and rocket applications, due to higher theoretical thermodynamic cycle efficiencies [1]. This higher thermodynamic efficiency is also beneficial for power generation. However, experimental realization of these higher thermodynamic cycle efficiencies has proven elusive. Several major challenges have plagued the development of a detonation engine for power generation. These challenges include: achieving reliable detonations for fuel-air operations, and the design of the thermomechanical system to convert the internal energy of the burned gases into mechanical work. Knowledge of the detonation cell size for various fuel oxidizer combinations and the use of DDT transition devices have made it

possible to achieve reliable detonations for a number of hydrocarbon fuels with air as the oxidizer [3].

A thermomechanical system capable of efficiently converting the internal energy of the burnt gases while withstanding the shock loading from a detonation wave has proven to be very challenging. There have been various attempts at efficiently producing work from detonation combustion using turbines which are driven by multi-tube pulse detonation engines (PDE) [4]. The exhaust flow of a detonation engine is inherently unsteady in contrast to conventional steady-flow combustors in turbine-based engines. However, these multi-tube PDE configurations aim to average the engine exhaust flow in order to simulate a steady exhaust flow similar to a conventional turbine combustor. These multi-tube pulse detonation engine turbine configurations are unable to average the exhaust flow due to very short over-pressure duration time of detonation combustion in the PDE, and the higher pressures generated by shock reflections on the turbine blades. Another shortcoming of this configuration is that the turbine blades are also subjected to large structural stresses due to repeated shock loading, and high heating of the thin turbine blades make them difficult to cool.

The PDE-turbine configuration may be acceptable for fundamentally demonstrating power generation, but engine development would require that the system is able to consistently produce power, and that the components are able to maintain their long-term structural integrity despite being subjected to repeated shock loading. Therefore, for practical reasons, a different approach for the thermomechanical system for a detonation based power generator makes uses of a reciprocating piston capable of withstanding repeated shock loading while producing mechanical power efficiently [33].

Exergy is the “available work” of an energy storage or transfer system. Exergy analysis allow for a common accounting metric of “available work” across complex thermomechanical systems [5-7]. This common accounting metric allows for the determination of where losses are present, and the identification of potential areas of efficiency improvements, while accounting for unavoidable energy losses due to the generation of entropy. In other words, exergy analysis applies both the first and second law of thermodynamics by accounting for the energy and entropy changes across each subsystem.

Exergy analysis has been applied in aerospace industry for the design optimization of vehicles and systems, taking into account the vehicle mission flight path. It has also been applied in the electric power generation industry in order to further optimize coal, diesel heat and power cogeneration plants operations [8]. Exergy analysis has been applied to the study of detonation engines for power generation [9]. Exergonomics analysis further extends the thermodynamics of exergy analysis to include the economic costs of using different fuels and their environmental pollution impact, in energy systems optimization [10].

1.2 Background

This dissertation focuses on the development of exergy analysis for a detonation-based power generator. Therefore, an understanding of detonation phenomena, pulse detonation engines, linear power generation, and exergy analysis is useful before detailed methodology is presented. Brief literature reviews on these four areas are also presented in this section.

1.2.1 Detonation Phenomena

The rapid release of energy by combustible materials has been observed since the 15th century. However, it was not until the development of photographic diagnostic tools in the late 19th century that scholars such as Mallard and Le Chatelier were able to determine that detonation was indeed a different and stable mode of combustion [11]. Since then, the study of detonation combustion has primarily evolved around explosive devices, and for prevention of mining and industrial explosions [12].

Detonation is a combustion process that involves a shock wave which adiabatically compresses and ignites the reactants, thereby rapidly releasing the chemical energy. The development of a theory to predict the rate of energy release of the detonations became of significant interest after its photographic discovery. A quantitative theory for predicting the detonation velocity was first developed separately by Chapman and Jouguet (CJ) who based their theory on the works of Rankine and Hugoniot that analyzed the conservation equations across a shockwave [11]. Chapman and Jouguet added heat release to this shock problem. CJ theory for detonation presents that the minimum velocity and minimum entropy solution are the equilibrium solution for the combustion products behind the shockwave of a detonation. However, neither Chapman nor Jouguet provided physical justification for these postulates. CJ theory does not require that the chemical kinetics of the combustion be taken into account, only that there is heat release behind a shockwave.

The modern definition of the detonation wave structure as comprising of a leading shock followed by a chemically reacting zone, which maintains the leading shock by generating thrust from the expansion of burned gases, was independently developed by Zel'dovich, von Neumann, and Döring (ZND) [11]. ZND theory requires integration across

the structure of the front, and the criterion used for iterating for the detonation velocity is the regularity condition at the sonic singularity, where the sonic condition is based on the frozen speed of sound. This is in contrast to the CJ criterion of minimum velocity, although both solutions still lie on the equilibrium Hugoniot curve. Also, using the ZND theory requires that the chemical kinetics be taken into account in solving for the detonation velocity.

The more common mode of combustion is deflagration, a subsonic wave sustained by chemical reactions that involve the heat transfer of burned products to ignite new reactants. In contrast to detonations, deflagration waves propagate at much lower velocities. The qualitative differences between detonations and deflagrations in gases are shown in Table 1.1 [13]. The subscript 1 is used for state variables of the unburned reactants, while the subscript 2 is used for the state variables of the burned products.

Table 1.1 Qualitative differences between detonations and deflagration in gases [13].

Parameter	Detonation	Deflagration
$\boldsymbol{u_1/a_1}$	5-10	0.0001-0.03
$\boldsymbol{u_2/u_1}$	0.4-0.7	4-16
$\boldsymbol{p_2/p_1}$	13-55	0.98-0.976
$\boldsymbol{T_2/T_1}$	8-21	4-16
$\boldsymbol{\rho_2/\rho_1}$	1.4-2.6	0.06-0.25

Table 1.1 shows that the combustion wave Mach number $M_1 = u_1/a_1$ of a detonation wave is at minimum two orders of magnitude higher than that of a deflagration wave. The velocity of the burned gases relative to the unburned gas is higher for a

deflagration in contrast to a detonation wave. However the pressure and density increase of the combustion products of a detonation wave is at least an order of magnitude higher than a deflagration wave due to the shock compression.

The sub-unity values of pressure and density ratios of deflagration highlight a key difference between detonation and deflagration. For detonation reactions the pressure and density of the products rise above the ambient conditions of the reactants, while for deflagration reactions the pressure and density of the products decrease below ambient conditions of the reactants. This key difference is also why detonation is synonymously referred to as "pressure gain combustion." Both deflagration and detonation waves release energy due to combustion, and as expected the temperature ratios of both reactions are of the same range in magnitude. However, it is important to note that the temperature ratio of a detonation reaction is typically 20% higher or more for equivalent reactant chemistry undergoing deflagration combustion, therefore the entropy of detonation reactions are lower.

Figure 1.1 shows a one-dimensional schematic of the detonation wave propagation within a tube. The same convention as in Table 1.1 is used, where subscripts 1 and 2 correspond to the state properties of reactant and product gases respectively. This figure shows the velocities of the gas products and reactants in the frame of a fixed shockwave, and the velocities in the frame of the fixed tube in the laboratory space.

In order to solve this problem the integrated conservation equations along with the equations of state of the products and reactants can be applied in order to derive the Hugoniot equation presented in equation 1.1. A detailed derivation of the Hugoniot

equation which describes the gas states across a propagating detonation wave is presented later in Chapter 2. The Hugoniot equation states that

$$e_2 - e_1 = \frac{1}{2}(p_2 + p_1)(v_2 + v_1) \tag{1.1}$$

where e are the internal energy, p are the pressures, and v are the specific volumes.

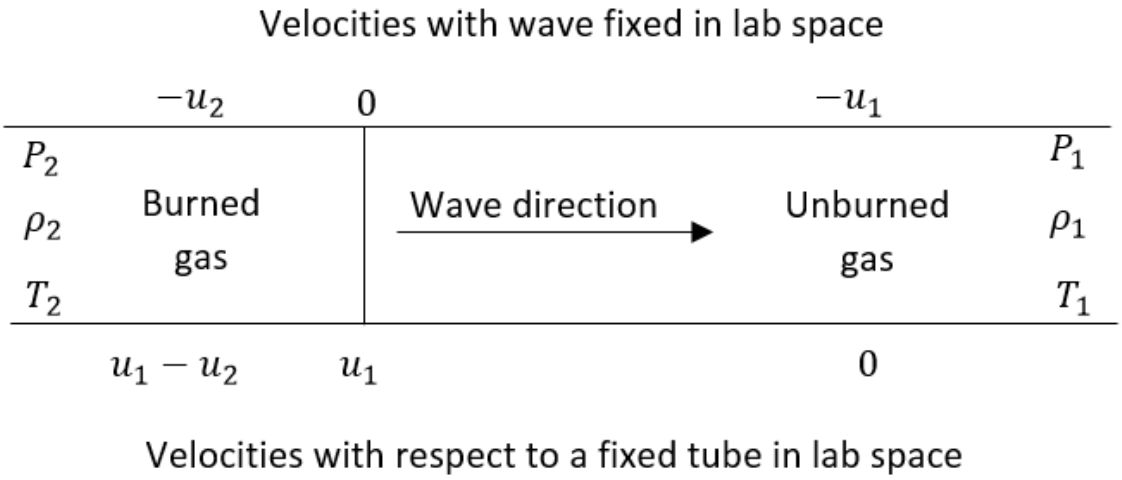

Figure 1.1: Schematic of detonation wave propagation.

The Hugoniot equation is valid for both shocks and detonations in all materials, as it does not include assumptions of perfect gas, or constant specific heat at constant pressure c_p and constant specific heat ratio γ. The Hugoniot equation can be plotted for any arbitrary value of internal energy, resulting in all the possible values of product pressure and specific volume, for a given value of reactant pressure and specific volume. However, not all the possible values of the burned gas velocities are physically valid in order to also achieve thermodynamic equilibrium. Therefore, it is important to establish which final values of pressure and specific volume solution on the reactive Hugoniot plot are physically valid. The Hugoniot relation is a hyperbolic equation and is plotted for a shock burned gas reactants in Figure 1.2.

The shock Hugoniot plotted in black corresponds to an internal energy increase of 0, for an initial reactant pressure and specific volume. This is the adiabatic solution for the Hugoniot equation. The reactive Hugoniot for stoichiometric hydrogen-air combustion is plotted in red. The possible solutions of the reactive Hugoniot can be divided into five regions, by plotting the pair of lines tangent to the reactive Hugoniot and originating from the initial condition, and the pair of horizontal and vertical lines intersecting the reactive Hugoniot and also originating from the initial condition.

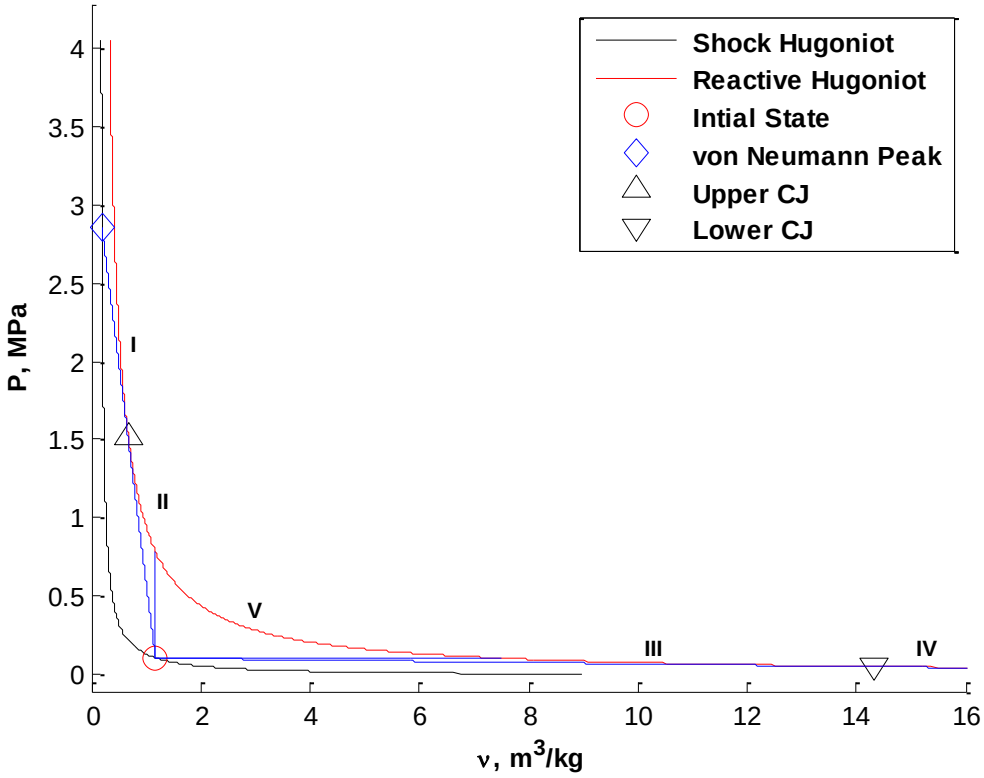

Figure 1.2: Real gas Hugoniot curves for stoichiometric H_2-air combustion.

The horizontal and vertical lines emanating from the initial condition correspond to lines of constant pressure and specific volume. The velocity obtained in region V, results in imaginary velocities, because it would require a compression wave to move in the negative direction, and therefore does not represent a real solution and can be eliminated.

Regions I and II represent the detonation branch of the reactive Hugoniot, while regions III and IV represent the deflagration branch of the reactive Hugoniot. The tangent points on the reactive Hugoniot correspond to the Chapman-Jouguet solutions for detonation and deflagration. The upper CJ solution corresponds to detonation while the lower CJ solution corresponds to deflagration.

Region I which extends above the upper CJ point corresponds to the strong detonation solution, predicts that the combustion product pressure is higher than the upper CJ value and that the reactants go from supersonic flow to subsonic flow in the fixed wave frame. The solutions in this region are physically possible but only in transient states since external effects quickly break down this state driving it to the stable upper CJ solution. Region II which extends between the upper CJ value and the line of constant volume heat addition corresponds to a weak detonation, since the product pressure is lower than the CJ value, resulting in the reactants going from supersonic flow to supersonic flow after passing through a normal shock. It is unphysical for flow to remain supersonic after passing through a normal shock, therefore the velocity solutions in region II are unphysical similarly to region V, and are eliminated from consideration.

Region III which extends between the lower CJ value and the line of constant pressure heat addition corresponds to a weak deflagration since the product pressure is higher than the predicted lower CJ value and results in the reactants travelling from subsonic to subsonic flow as they become products. All the velocity solutions in this region are physically valid, and correspond to laminar flame solutions. Region IV which extends below the lower CJ value corresponds to a strong-deflagration, since the product pressure is the lesser than the lower CJ value, and result in the reactants travelling from subsonic to

supersonic flow as they become products. The velocity solutions in this region are invalid, as it is not physically possible to have flow with heat addition proceed past the maximum entropy at sonic condition to become supersonic with lower entropy.

The upper CJ tangent line originating from the initial conditions intersects with the shock Hugoniot at a higher pressure referred to as the von Neumann peak. For a propagating detonation wave, the leading shock front compresses the reactant gases from the initial state along the shock Hugoniot to the von Neumann peak. The line segment between the von Neumann peak and the upper CJ point is a line of constant area heat addition, also referred to as Rayleigh flow. This line segment is relatively easy to draw in the p-v plots shown in Figure 1.2. However, this line of constant area heat addition is rarely drawn correctly in T-s plots of published literature on the detonation cycle [38, 39].

The relationships for the temperature T and entropy change Δs to the post-shock Mach number M of the reactants are given by

$$T = T^* \left[\frac{(\gamma+1)M}{1+\gamma M^2}\right]^2 \tag{1.2}$$

$$\Delta s = c_p \ln\left[M^2\left(\frac{\gamma+1}{1+\gamma M^2}\right)^{\frac{\gamma+1}{\gamma}}\right] \tag{1.3}$$

where T^* is the upper CJ temperature, γ is the post shock heat capacity ratio, and c_p is the specific heat at constant pressure.

It is important to note that the post shock Mach number of the reactants is subsonic, therefore heat addition which thermally chokes the flow is along the subsonic flow path of the Rayleigh line. Using equations 1.2 and 1.3, Figure 1.3 was plotted to show the Rayleigh line plotted for dimensionless enthalpy T/T^* and dimensionless entropy Δs, in the

subsonic and supersonic flow regimes. The plot shows that heat addition to a subsonic or supersonic flow drives the flow to become thermally choked with maximum entropy, hence having a Mach number of unity. The Rayleigh flow regime relevant to detonation combustion is that of subsonic flow heat addition.

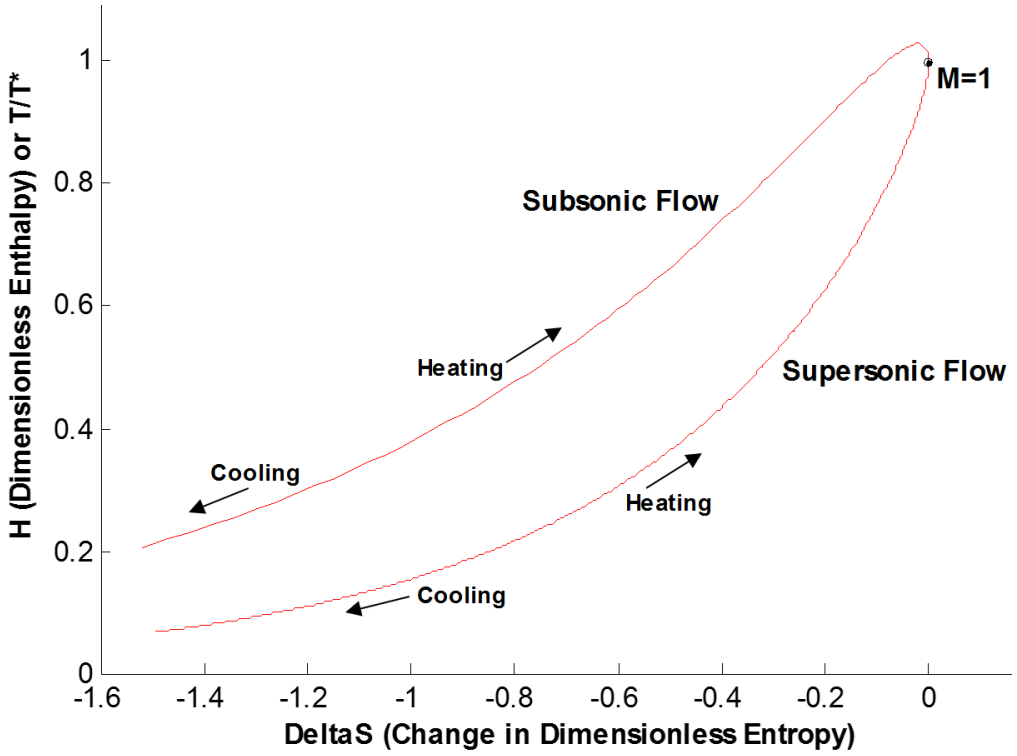

Figure 1.3: Rayleigh line plotted in dimensionless H-Δs.

A unique characteristic of detonation is that the combustion front is intrinsically unstable and has a transient three dimensional structure of transverse waves, even though it yields a steady average propagation velocity close to that derived from one dimensional CJ theory. The intersection of these transverse waves produces a "diamond" or "fish scale" pattern which can be recorded on smoked foil lining inside of a detonation tube. This technique is the standard used to measure the cell size of detonation waves. A theory

capable of correctly predicting the cell size based on the chemical kinetics of reactants remains an area of open research [14].

The detonation cell sizes for two fuels with oxygen and air are presented in Table 1.2. The table shows that the cell sizes for fuel-oxygen combustion is generally an order of magnitude lower than that of fuel-air combustion. The detonation cell size λ of a reaction is a key metric in determining the critical tube diameter required for a self-sustaining detonation wave to propagate within a confined area.

Table 1.2 Detonation cell size for two fuels with oxygen and air at STP (T = 293 K, p = 1 atm).

Mixture (φ = 1)	λ Width, mm	Reference
$2H_2 + O_2$	2.08	Denisov [15]
$2H_2 + O_2 + 3.71N_2$	15.1	Guirao [16]
$CH_4 + 2O_2$	4.8	Bauer [17]
$CH_4 + 2(O_2 + 3.71N_2)$	291.7	Moen [18]

Detonations can be initiated by various techniques such as the use of a deflagration-to-detonation transition (DDT) device, shock-induced detonation, detonation-induced detonation, and direct initiation. The most common of these detonation initiation techniques requires the use of a DDT device. Examples of DDT devices include Shchelkin spirals, orifice plates, grooves, and other obstacles. The effectiveness of various DDT devices has been studied by several investigators. The common metric used to identify the DDT device is its tube blockage ratio defined relative to the tube diameter. For example, various orifice rings were placed at equi-partitioned locations along tubes by Peraldi et al.

resulting in blockage ratios of $BR = 0.43$, 0.39, and 0.43 for 5, 15 and 30 cm diameter tubes respectively [19]. Note: The blockage ratio BR is defined as $BR = 1 - (d/D)^2$, where d and D are the inner diameters of the orifice rings and combustion tube respectively.

Shock-induced detonation is used in hypersonic facilities in order to generate the high enthalpy flows required to accurately simulate hypersonic flight in the wind tunnel [20]. Detonation-induced detonation is used to create an overdriven detonation, or to detonate a less energetic mixture with the propagation of a more energetic mixture, such as in studies performed by Li et al. where an overdriven detonation wave from propane-oxygen to is used to detonate propane-air mixture [21]. Direct initiation is generally created with the use of an explosive. This ignition technique is typically used in the study of the propagation and structure of spherical detonations [11].

Fundamental studies of detonation phenomena continue in order to prevent detonations in pipes and coal mines. There are still fundamental knowledge gaps in deflagration-to-detonation transition, and in particular quasi-detonations which have been studied in straight walled tubes [3]. For example in coal mines, current detonation mitigation techniques fail to account for the vortices induced by the flame-shock complex and the flame acceleration due to obstacles. In the case where the resultant flow is a quasi-detonation (strong-deflagration), the combustion zone maintains the turbulent-flame front in the absence of further turbulence generation from an obstacle such as a Shchelkin spiral, similarly to how the combustion zone maintains the shock front in a detonation wave.

1.2.2 Pulsed Detonation Engine (PDE) and Filling Techniques

In the past couple of decades, the development of detonation-based rocket and air-breathing engines has been explored by the aerospace community to advance the state-of-the-art of the thermal efficiency of propulsion devices [22, 23]. These efforts have included the development of engines such as the pulse detonation engine (PDE), the rotating detonation engine (RDE), and oblique shock wave detonation engine. The PDE is the most developed of these engines, and only within the past few years have these development efforts resulted in inflight aircraft and rocket demonstrators [24, 25]. There have also been research and development efforts to develop PDE-turbine systems for power generation [26, 27].

The PDE operates by using the leading shock of a detonation to generate high pressure without a compressor, or at least a small amount of pre-compression, in contrast to the large compressors found in turbojets and gas generators. A typical PDE configuration consists of a constant cross-sectional area straight thrust tube, which is sealed at one end and open at the other. Attached to the detonation tube are proper support systems which include control valves for purging, fuel and oxidizer filling, and an ignition system which provides the heat required for ignition. Most practical PDEs employ a deflagration-to-detonation transition (DDT) device which is typically a Shchelkin spiral in order to achieve reliable detonations [28]. A nozzle can also be attached to the PDE in order to improve its performance. Nozzle configurations for the PDE capable of significantly improving and optimizing its performance remain an open area of study [29]. In this study, a simple PDE coupled with a nozzle is used for development of exergy efficiency measurements.

The PDE cycle has four primary stages. They include the purge, fill, combustion and blowdown or exhaust stages. The stages of a regular PDE cycle are shown in Figure 1.4. This cycle begins with the purge stage, which requires the purging of the detonation tube typically with an inert gas such as air at ambient pressure condition p_0. This is then followed by the filling stage, where fuel and oxidizer are introduced into the tube at an initial pressure of p_1.

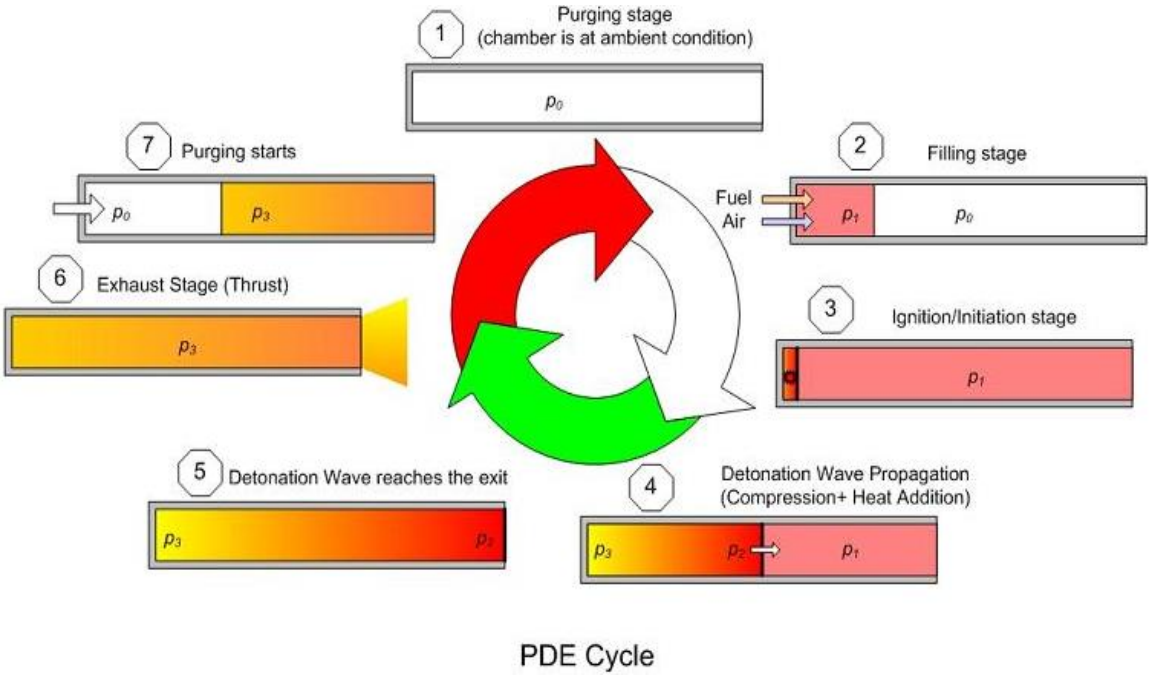

Figure 1.4: PDE cycle stages [30]

It is generally desired to fill the entire tube with fuel and oxidizer, at a pressure which typically matches the ambient pressure condition p_0. The fuel and oxidizer filling stage is followed by the combustion stage which includes the ignition of the combustible mixture in the detonation tube. The filling and ignition stages are typically timed such that no fuel and oxidizer escape the tube. The ignition creates a deflagration wave which transitions to a detonation wave with the help of a DDT device. The fully formed

detonation wave then travels down the length of the detonation tube, compressing the unburned gases ahead of the wave, before burning it in the reaction zone of the detonation wave to the CJ pressure p_2.

The burned gases behind the detonation waves are expand below the CJ pressure by a Taylor rarefaction wave. However, the closed wall of the detonation tube imposes the boundary condition of no flow through the wall, which causes the burned gases to stagnate at a pressure p_3. Several investigators have presented detailed analytical models for this thrust wall pressure in order to determine the specific impulse performance of the PDE [31]. A one-dimensional model of the thrust wall pressure based on the wave propagations within the detonation tube is also presented in this work.

The detonation wave propagates the length of the tube until it reaches the exit, completing the combustion stage. This causes an expansion wave to travel upstream through the detonation tube exhausting the chamber below sub-atmospheric pressures, and initiating the exhaust or blowdown stage. Some burned gases remain in the tube. Therefore a purge by an inert gas is performed to clear the detonation tube of burnt combustion products. This purging also cools the internal walls of the detonation tube which is exposed to high temperature combustion gases. The purge marks the beginning of a new cycle, and the aforementioned stages repeat.

The purging valves, filling valves, and ignition source are typically located by the closed end of the tube. It is also typical to find PDE configurations where the ignition source is located away from the closed end. Some investigators have reported performance improvement by locating the ignition source at the middle of the PDE and the PDE exit

[31]. The performance improvements occur because, although the DDT process in this configuration is delayed, a retonation wave travels back through the burned gases further compressing it, therefore resulting in a similar performance with the assumption that all of the gas in the detonation tube is detonated, even though some of the reactants underwent deflagration during to DDT process, while the stagnation pressure increases in the tube due to the shock reflection of the closed end.

A unique feature of the PDE in contrast to other combustion engines, is that the combustion chamber can be fully- or partially-filled with fuel and oxidizer while still maintaining the desired equivalence ratio. Figure 1.5 shows the filling characteristics of a fully- and partially-filled PDE.

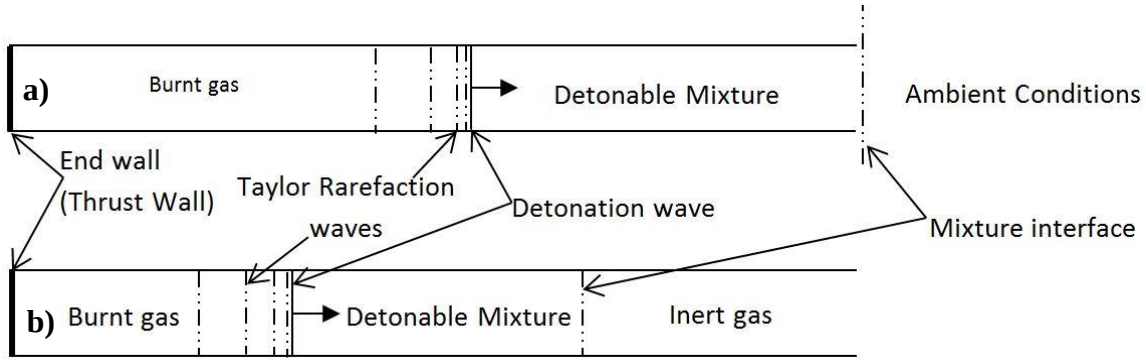

Figure 1.5: Filling characteristics of a PDE a) fully filled and b) partially filled.

Partially filling the thrust tube with a detonable mixture has been examined as a method for optimizing the performance of PDEs [31, 32]. The operation of a fully-filled PDE shown in Figure 1.5a, is simplified by assuming an instantaneous transition to a detonation wave traveling towards the open end of the thrust tube, followed by an unsteady Taylor rarefaction, and a reflected rarefaction wave for exhausting the tube. In this study,

the performance of a fully- and partially-filled PDE is examined analytically based on the characterization of the wave processes occurring in each cycle of operation.

In partial filling, as shown in Figure 1b, only the upstream portion of the tube is filled with reactive mixture while the rest is filled with an inert gas. For this analysis, the inert gas is air but it can be the burned gas in practice. The analysis of the partially-filled PDE is simplified via the same assumptions as the fully-filled PDE, but also includes the transition of the detonation wave to a transmitted shock wave, and the subsequent wave interactions. The initial conditions were for a stoichiometric oxyhydrogen mixture. From the analysis, the pressure history at the thrust wall for both the fully- and partially-filled PDE are characterized. Numerical studies of partial-filling have also aimed at predicting the thrust and specific impulse performance of a partially-filled PDE by assuming that the tube is homogeneously filled [32].

The equivalence ratio of the fuel to oxidizer can also be varied for PDE operation. It is generally desirable to operate the PDE near stoichiometric values, as it has a narrower range of feasible combustion equivalence ratio in contrast to deflagration for a similar mixture.

Another important parameter to consider in the operation of the PDE is the frequency of operation. The PDE frequency is the rate at which all four stages of the PDE cycle are repeated. The control of the PDE frequency is done by properly timing the purge valves, fill valves, and igniter system to operate at the desired frequency. High-frequency operation consumes more fuel per unit time, generating more heat loads and is generally desired for aerospace and power generation applications in order to produce more thrust or power.

1.2.3 PDE - Linear Power Generation

The PDE by definition produces energy pulses similar to a conventional internal combustion engines (ICE) such as the Diesel and Otto cycle engines. However, due to the presence of a shockwave travelling at supersonic speeds, the pressure loading rate in a PDE is over three orders of magnitude higher than that of its deflagration ICE counterparts. Therefore coupling a crankshaft to the PDE would likely result in the destruction of this crank-slider mechanism due to the infinite jerk present due to the impulsive acceleration.

Alternatively, several groups have made efforts in coupling the PDE to a turbine, but the pressure loading due to shockwave impingement on the turbine blades does not make this a structurally practical device [4]. Therefore previous efforts at UTA's Aerodynamics Research Center have focused on the coupling of this dynamic engine with a dynamic power generator [33]. These efforts culminated in the feasibility demonstration of electrical power generation by a PDE system coupled to a linear power generator.

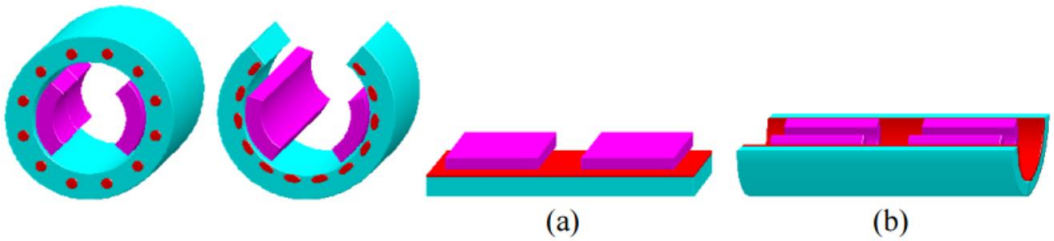

Figure 1.6: Creating a linear generator from its rotary counterpart (a) flat (b) tubular [54].

A linear power generator (LPG) is generally defined as a device that harnesses oscillatory linear motion to generate electrical energy. Figure 1.6 shows how one could create a flat or tubular linear power generator from its rotary counterpart. It operates on the same principles as its rotary counterpart. Faraday's law shows that an induced voltage from

a time changing magnetic field governs the operation of transformers, while the production of an induced force on a conductor within a magnetic field governs motor operation, and induced voltage on a conductor moving in a magnetic field governs generator operation. A magnetic circuit such as the LPG has flux, reluctance, and the magneto-motive force, analogous to current, resistance and voltage in an electric circuit [34].

The linear power generator has long been proposed as an alternative method to generate electricity as compared to the traditional rotary method. For example, wave energy harvesting stations are currently being used to harvest the natural energy of the rise and fall of waves [35]. The LPG has been demonstrated to achieve high efficiencies. For example, a 40 kW, 96% efficient linear alternator with a radially magnetized slider with maximum speeds of 2 m/s was demonstrated in 2001 by Sandia National Laboratories [36].

For comparison, consider the gas turbine generator configuration shown in Figure 1.7a which uses deflagration combustion of fuels such as natural gas to drive a turbine to generate electricity. In Figure 1.7b, the PDE is the combustor, and the turbine is replaced by the LPG referred to as the resonator. The gas turbine and PDE-LPG system can be operated with the same fuel-oxidizer mixture, but rather than using a deflagration combustion and a turbine for power generation, the PDE-LPG uses detonation combustion for improved thermal efficiency, and a resonator for power generation.

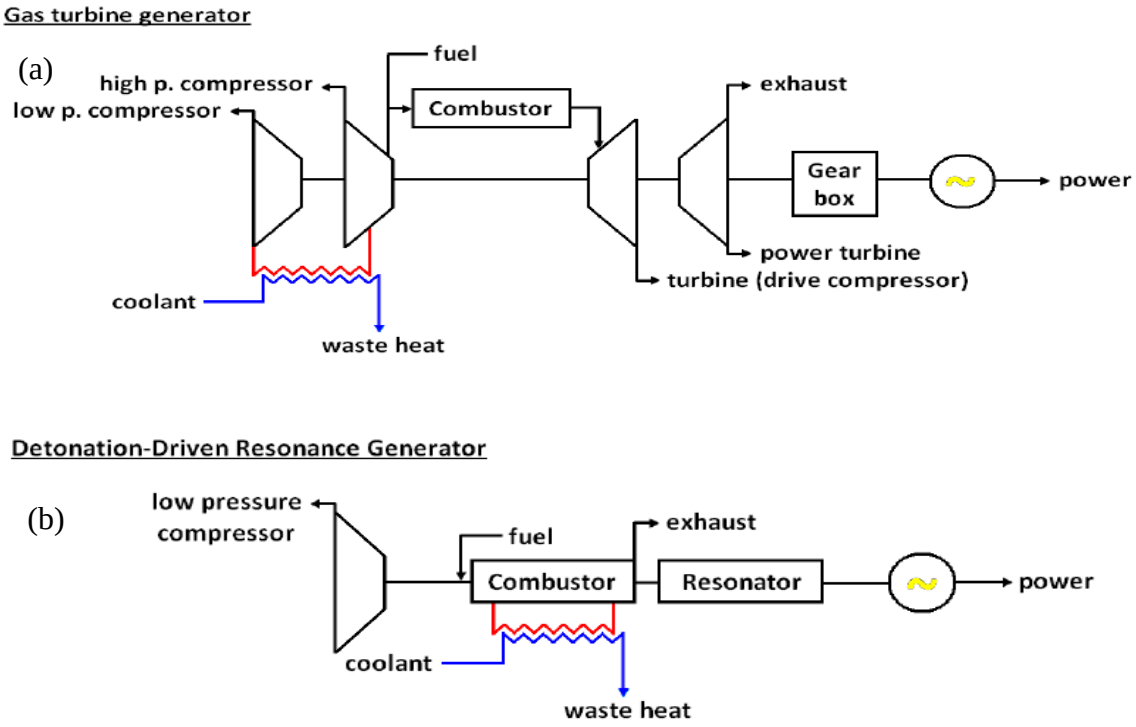

Figure 1.7: Main components of (a) a gas turbine generator and (b) a detonation driven resonance generator [33].

1.2.4 Heat Engine Energy and Exergy Efficiency Cycle Analysis

Designing engines for optimal overall system performance is a challenging task. Historically, energy-based analysis is used for the analysis of thermodynamic systems [5, 8]. Although this approach is sufficient in satisfying conditions imposed by the first law of thermodynamics, it does not constrain the feasibility of the system. Exergy-based analysis which utilizes both the first and second law of thermodynamics provides only the feasible states. This approach also provides a common accounting metric "exergy destruction" across the various processes [6, 7].

Cycle analysis comparisons of the PDE have been conducted in the past, but these efforts have used the constant volume compression, Humphrey cycle which ignores the

shock compression of the detonation wave, and assumes deflagration combustion at constant volume [37, 38]. Some authors have considered the ideal cycle of the PDE to be based on the ZND cycle, but they did not consider the non- equilibrium thermodynamics of the shockwave [39].

Energy analysis of pulse detonation turbine engine (PDTE) systems has been conducted by several investigators [40, 41]. Generally, the thermal efficiency results have been in the single digits ranging from 5-9%, much lower than the predicted theoretical thermal efficiency of 30% with no external pre-compression. The primary challenge identified with the PDTE system is that the turbine does not play a conventional role in the expansion of the burned gases similar to steady flow engines. Therefore the heat loses of the overall system are very high, and the internal energy generated from combustion is simply carried away by exhausting gases.

Exergy analysis incorporates the second law of thermodynamics, the conservation laws, and examines the maximum useful work that can be obtained from a system in a specified environment referred to as the dead state. This gives a process implied directionality and the solutions feasible and practicable bounds. There has been very limited work which examine the exergy performance of a PDE system. Bellini et al. have performed exergy analysis studies on electric power generation with a PDE, while examining the tube length and operational frequency [9]. Hutchins et al. have performed energy and exergy analysis for various hydrocarbon fuels with potential applications in air-breathing propulsion [38].

1.3 Research Objectives and Contributions

1.3.1 Objectives of Research

The primary objective of this research is to develop a methodology for determining the overall system energy and exergy efficiency of a pulse detonation engine linear power generator (PDE-LPG) system. The approach is both analytical and experimental. For this purpose, an analytical model of the PDE performance for varying detonation tube fill-fraction was developed. The experimental efforts included the building of a small-scale PDE-LPG test rig. This facility aimed to improve the performance PDE with a nozzle, coupled the PDE with a piston-spring system to efficiently produce work, and converted the produced mechanical work into electricity. The research objectives are listed below.

- Develop an analytical and experimental approach for the energy and exergy analysis of a detonation engine based power generator.
- Compare the analytical and experimental results of the effects of a partial-filling on PDE performance.
- Compare the thermodynamic cycles of the PDE and other heat engines through first and second law analysis.
- Develop a mobile PDE-LPG facility including all essential subsystems required for operation in order to study transfer of energy and exergy.
- Quantify system energy and exergy efficiencies through experiments with a small-scale PDE-LPG.
- Understand the practical limitations of a PDE-LPG in efficiently converting chemical exergy into electrical exergy.

- Understand the effect of a nozzle on the potential performance gains of a PDE.

1.3.2 Literature contributions

A few of the objectives of this research have been accomplished and have been presented in conference papers and in completed and soon-to-be-submitted journal papers. These publications include:

- Bello, R. T., and Lu, F. K., "Performance Model for Fully and Partially Filled Pulse Detonation Engine," *53rd AIAA Aerospace Sciences Meeting,* AIAA SciTech Paper 2015-1352, *5-9 January 2015, Kissimmee, Florida.*
- Joshi, D. D., Peace, J. T., Bello, R. T., Carter, D., and Lu, F. K., "Flow Visualization of the Exhaust Jet from a Pulse Detonation Engine by Mie Scattering," *30th International Symposium on Shock Waves,* 19-24 July, 2015, Tel Aviv, Israel.
- Bello, R., University of Texas at Arlington Master's Thesis; December 2012: "High Enthalpy Characterization of UTA Hypersonic Shock Tunnel"

Papers being prepared:

- Journal article on "Energy and Exergy Analysis of Detonation Engines for Power Production"
- Journal article on "Performance of Fully and Partially Filled Pulse Detonation Engine"
- Journal article on "Thermodynamic Cycle Analysis of Detonation Based Piston Engine"
- Journal article on "Exergy Analysis of Pulse Detonation Engine Linear Power Generator System"

CHAPTER 2

General Approach

This chapter describes the details of the methodology to improve PDE performance, to quantify and compare energy and exergy cycle efficiencies, and to compute the overall system energy and exergy efficiency from experimental data. In the subsequent sections the process of characterizing the chemical, thermal, mechanical, and electrical exergies, the performance of a partially-filled PDE, and ideal cycle analysis for the PDE-LPG cycle relative to other cycles are presented.

2.1 Methodology

Determining overall system efficiency lies in quantifying fuel energy input and the work output. Using this as a baseline for the total energy added across each level of energy conversion, the exergy transferred is quantified based on experimental readings. Similar to other power generators, the PDE converts chemical energy from fuel into enthalpy, from which a fractional amount is then converted to mechanical work and then finally into electrical energy. Unlike chemical energy which is quantified by mass (and energy) flow, there are currently no practical methods to directly measure the thermal efficiency of the PDE. Therefore, an effort is made to compute the work from pressure measurements on the prime mover, in order to compute the experimental thermal efficiency. The dynamics of the prime mover are characterized as a simple single degree of freedom (SDOF) system with viscous damping in order to determine the mechanical work, and therefore determine the mechanical efficiency. The uninstalled efficiency performance of the LPG was determined in separate experiments presented later in Chapter 3.

The performance of the PDE-LPG system was improved by attaching a diverging nozzle to the PDE exit. This device converts the enthalpy of the PDE exhaust into kinetic energy that can be readily transferred to the prime mover. The individual performance of the nozzle was evaluated based on the pressure profiles measured at the throat and exit of the nozzle, and is presented in Chapter 4.

The various types of energy types and transfer are presented in Table 2.1. This table shows that the fuel's chemical potential energy, is converted to internal energy stored in gases at high pressure, which pushes the piston-spring system that stores mechanical energy in spring compression, and finally the piston-spring system transfers its motion to a linear power generator which generates electrical energy.

Table 2.1 PDE-LPG energy types and characteristic experimental measurements.

Energy Type	**Chemical**	**Internal**	**Mechanical**	**Electrical**
Quality Factor	QF < 1	QF < 1	QF = 1	QF = 1
Energy-work	E ≠ W	E ≠ W	E =W	E =W
Source	Fuel	Gas Pressure	Springs	Linear Power Generator
Experimental Measurements	Mass flow rate	Stagnation Pressure	Spring Displacement	Voltage & Current

In exergy analysis, the quality factor of an energy type describes the ratio of the sources energy to exergy. A quality factor of unity, means that all the energy of this type is available work (or exergy). This is true for mechanical and electrical energy. A quality factor less than unity means that some but not all of the energy of this type can be converted to work, and applies for chemical and internal energy. Direct measurements of the electrical energy output of the generator and the mass flow rate into the PDE-LPG

generator system allowed for calculations of the overall system energy and exergy efficiency.

2.1.1 Chemical Exergy

The chemical exergy of a substance is the maximum amount of available work that can be extracted from the substance by bringing it from its local environmental state to the dead state; which is the equilibrium temperature, pressure, and chemical composition of the substance in the ambient conditions of the standard environment. The chemical exergy of substances of interest in this work, is that of fuels and the resultant combustion products. Therefore, it is of interest to determine the maximum work that could be extracted per mole of fuel if products and reactants are brought to chemical equilibrium with the standard environment. For complete combustion of one mole of a hydrocarbon $C_\alpha H_\beta$ with diatomic oxygen O_2:

$$C_\alpha H_\beta + \left(\alpha + \frac{\beta}{4}\right) O_2 \rightarrow \alpha CO_2 + \frac{\beta}{2} H_2O \tag{2.1}$$

The maximum available work for complete chemical combustion is the difference of the sum of the chemical potentials of the reactants from the sum of the chemical potentials of the products in the dead state. This relationship is presented below

$$W_{rev} = \xi_{ch} = \mu_{C_\alpha H_\beta} + \left(\alpha + \frac{\beta}{4}\right)\mu_{O_2} - \alpha\mu_{CO_2} - \frac{\beta}{2}\mu_{H_2O} \tag{2.2}$$

where W_{rev} is the maximum reversible work per mole of fuel, ξ_{ch} is the chemical exergy per mole of fuel, and μ are the chemical potentials. This relationship can be further simplified since the chemical potential of the fuel is the same as the Gibbs free energy, and

by normalizing the chemical exergy value with the fuel lower heating value (LHV). This results in an approximate relation between the chemical exergy ξ_{ch} and the LHV for gaseous hydrocarbons, derived by Moran [42]

$$\frac{\xi_{ch}}{\mathrm{LHV}} \cong 1.033 + 0.0169\frac{\beta}{\alpha} - \frac{0.0698}{\alpha} \tag{2.3}$$

The fuel lower heating value assumes that the final state of H_2O products from the combustion is gaseous, while the fuel higher heating value (HHV) assumes that the final state of H_2O products from combustion is liquid. The equation 2.2 is also valid for hydrogen which corresponds to $\alpha = 0$ and $\beta = 2$. Equation 2.1 applied to hydrogen corresponds to the stoichiometric combustion that was used for all the experiments in this work. For the overall PDE-LPG system energy and exergy analysis, the mass flow rate for various fill fractions was used in conjunction with the LHV assumption. The fuel chemical exergy was computed from equation 2.2.

2.1.2 Thermal Exergy

The thermal exergy ξ_t or exergy of enthalpy of the PDE-LPG facility, comprises of the sum of the internal exergy ξ_U and the flow work ξ_{Flow} [5]. The thermal exergy is the maximum available useful energy that can be extracted from the exhaust stream of burnt combustion products of the PDE as it reaches thermal, mechanical, and chemical equilibrium with the environmental dead state, and is given by

$$\xi_t = \xi_{Flow} + \xi_U \tag{2.4}$$

$$\xi_t = [pv - p_0 v]_{Flow} + [(e - e_0) - p_0(v - v_0) - T_0(s - s_0)]_U \tag{2.5}$$

where e_0 is the dead state internal energy, p_0 is the dead state pressure, v_0 is the dead state specific volume, T_0 is the dead state temperature, s_0 is the dead state specific enthalpy.

In the exergy analysis of the experimental data, the exergy of the internal energy was not accounted for due to a lack of a total temperature measurement required to calculate the entropy relative to the dead state temperature. However, the flow exergy was accounted for with stagnation pressure measurements relative to the dead state pressure of 1 atm. A generalized exergy balance across an arbitrary work or heat device is presented later in section 2.3.3.

2.1.3 Mechanical Exergy

The mechanical exergy ξ_{ME} of the PDE-LPG facility, comprises of the spring energy that arises from the motion of the piston compressing and extending attached compression springs. This spring energy can be converted entirely into work. In other words, the mechanical exergy from the system's spring energy is equal to kinetic energy itself. The mechanical exergy is the maximum available work that can be extracted from the spring as it reaches equilibrium with the dead state, which corresponds to no displacement and is therefore zero. The mechanical exergy is given by

$$\xi_{ME} = \frac{1}{2}\omega_n^2 x^2 \tag{2.6}$$

where ω_n is the natural frequency of the piston-spring system, and x is the displacement. For the mechanical exergy analysis of the PDE-LPG facility from experimental data, the displacement of the spring was directly measured. The effective spring constant was measured through separate experiments which allowed for the determination of the natural frequency of the system.

The force input from the PDE on the piston-spring system can be described as a short-duration impulse. The normalized response of the piston-spring system to impulsive loading was modeled for an underdamped and an overdamped case, and is presented in Figure 2.1. An impulse I consisting of a large force acting over a very short time, such as that delivered by the PDE onto the piston, acts similarly to giving the piston mass m an initial velocity of $\dot{x} = I/m$, but leaving it with an initial displacement of $x = 0$. For the underdamped piston-spring system the impulse response function is

$$x(t) = \frac{I}{m\omega_d} e^{-\zeta\omega_n t} \sin(\omega_d t), \quad \zeta < 1 \tag{2.7}$$

while, for the overdamped case, the impulse response function is

$$x(t) = \frac{I}{m\omega^*} e^{-\zeta\omega_n t} \sinh(\omega^* t), \quad \zeta > 1 \tag{2.8}$$

where $\omega_d = \omega_n\sqrt{1-\zeta^2}$, and $\omega^* = \omega_n\sqrt{\zeta^2-1}$, ω_d is the damped natural frequency, and ζ is the damping ratio [43].

The piston-spring system of the PDE-LPG facility operates in an underdamped mode the vibration, when the piston is simply supported on the bottom by ball bearings, and does not cover the PDE nozzle flange. This underdamped operation generates oscillatory motion that is mechanically transferred into the linear power generator. This underdamped operation also allows for the potential operation of the PDE-LPG at resonance through pulse-to-pulse interaction, which can drastically increase the response of the piston-spring system by an order of magnitude.

The piston-spring system can also be operated in an overdamped mode when the piston covers the PDE nozzle flange and is simply supported by set screw ball bearings

that roll in groves set in the PDE nozzle flange. The underdamped operation requires that the piston was placed farther away from the nozzle exit and therefore produced smaller displacements in contrast to the overdamped mode which produced larger peak displacements, but which did not yield oscillatory motion after the spring returns the piston to its nominal position, or dead state. The normalized displacement responses $R(t)$ for an underdamped and overdamped piston-spring (SDOF) system are modeled in Figure 2.1a and 2.1b respectively.

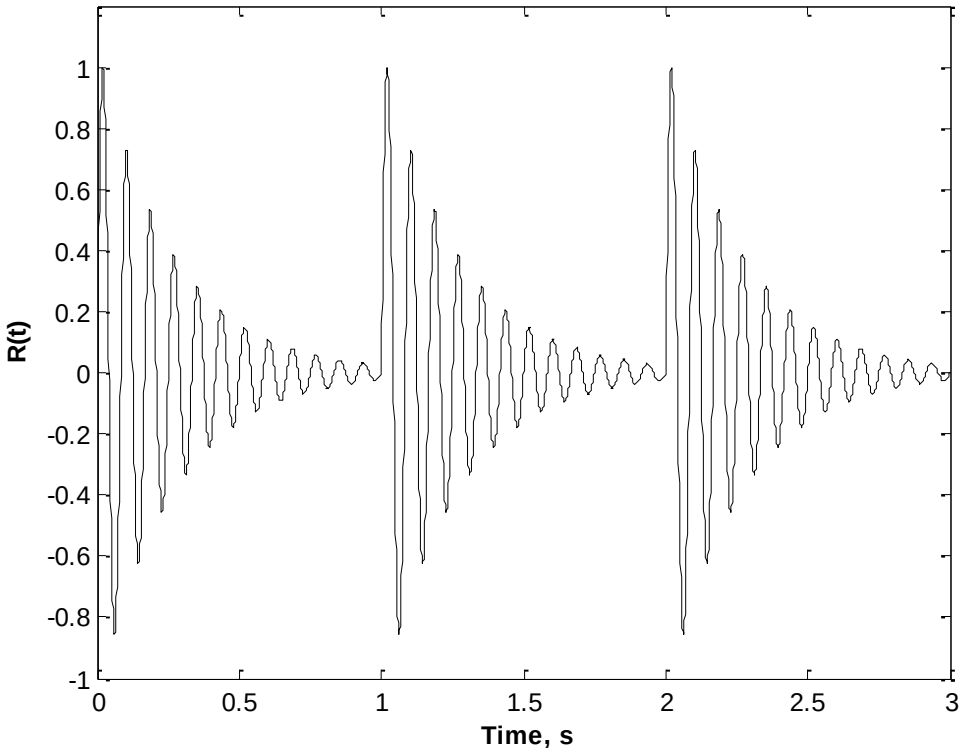

(a) Underdamped

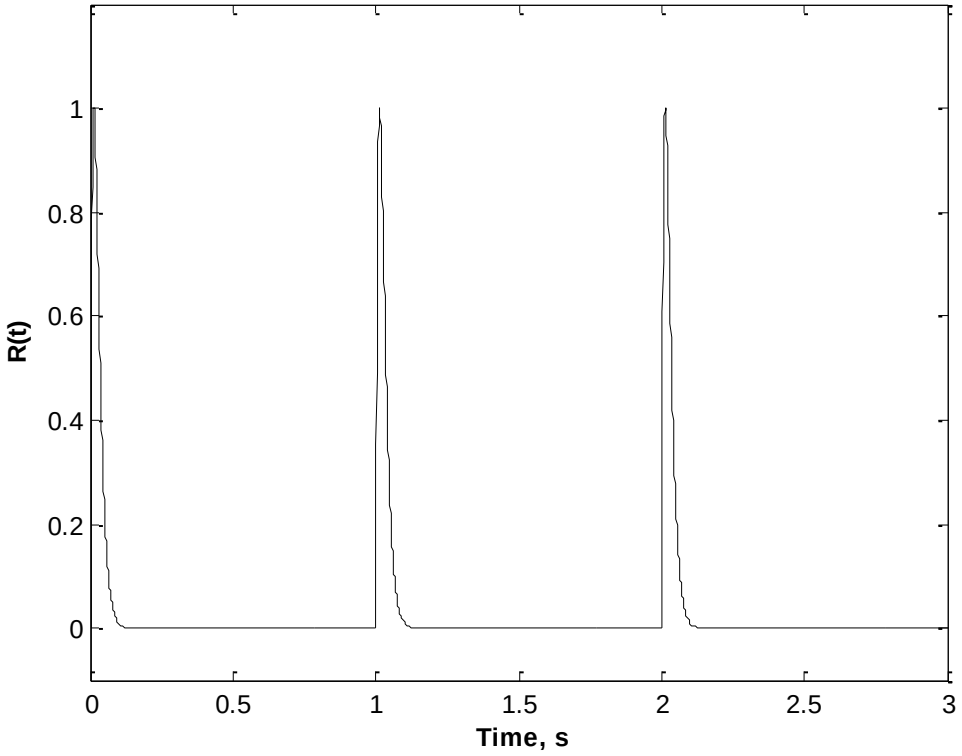

(b) Overdamped

Figure 2.1 Piston-Spring (SDOF) System Response to PDE impulse.

2.1.4 Electrical Exergy

The electrical exergy Ξ_E of the PDE-LPG facility comprises of the electrical energy generated by the electromotive force or voltage induced in the LPG stator windings by the motion of the LPG magnetic slider. The electrical energy can be entirely converted to work. In other words, the electrical exergy from the system's electrical energy is equal to electrical energy itself. The electrical exergy is the maximum available work that can be extracted from the LPG as it reaches equilibrium with the dead state, which corresponds to no induced voltage, and is therefore zero. The electrical exergy is given by

$$\Xi_E = P_{avg} t = I_{rms} V_{rms} t \tag{2.9}$$

where P_{avg} is the average power, I_{rms} is the root mean square current, and V_{rms} is the root mean square voltage.

For the electrical exergy analysis of the PDE LPG facility, the electrical current and voltage were simultaneously measured during the generator operation. From the time varying current and voltage, the root mean square current and voltage were computed over the same duration as the slider motion. The root mean square current and voltage values for an alternating current power generator corresponds to an equivalent DC voltage and current. The slider motion follows the displacement profile of the piston-spring system for an overdamped response to a PDE impulse shown in Figure 2.1(b). The electrical energy per pulse was directly computed by numerical trapezoidal integration of the time varying power over the duration of the slider motion.

2.2 PDE Filling

One of the ways that the performance of the PDE can be altered is by controlling the amount of fuel and oxidizer that is introduced into the detonation tube. Completely filling the detonation tube with a detonable mixture is referred to as the fully-filled PDE, partially filling the detonation tube with a detonable mixture is referred to as a partially-filled PDE, and overfilling the detonation tube with a detonable mixture is referred to as an over-filled PDE. Partial filling has been explored as a way to improve the performance of the PDE in comparison to the fully-filled operation, while over-filling the detonation tube has been shown to be the less fuel efficient mode of operation. Wave diagrams for the fully and partially filled cases, and the corresponding thrust wall pressure performances are presented in this section.

2.1.1 Fully-Filled PDE

The fully-filled PDE cycle requires that the thrust tube be completely filled with a detonable mixture of gases as illustrated in Figure 1.5a. This allows the detonation wave to travel the entire length of the tube, filling the entire volume with a transient high-pressure combustion exhaust. This generates the maximum thrust and mixture specific impulse. The wave diagram of a single cycle for a fully-filled PDE of stoichiometric oxy-hydrogen mixture at STP is shown in Figure 2.2.

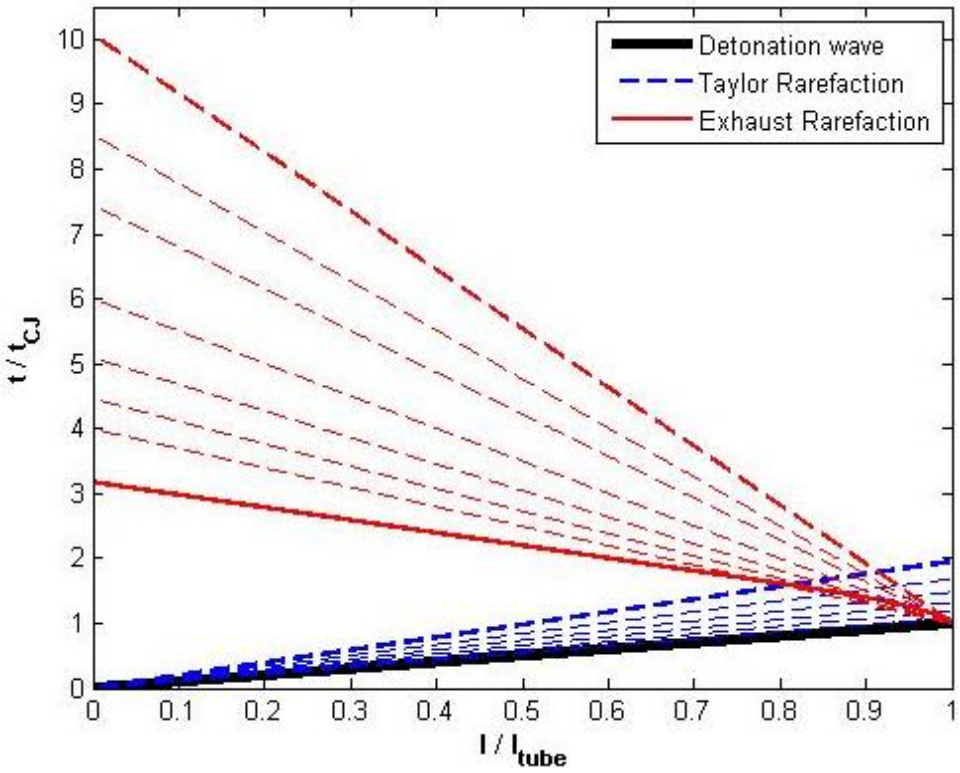

Figure 2.2 Wave diagram for fully-filled PDE.

This cycle is characterized by a Chapman-Jouguet detonation, a Taylor rarefaction, and an exhaust rarefaction. Since there is no inherent length scale in these idealized wave processes, the length scale is non-dimensionalized by the length of the tube. For convenience, the time is non-dimensionalized by the duration of the detonation wave in the

tube. The incident Taylor rarefaction and exhaust rarefaction interact toward the end of the tube. These interactions are ignored since both waves are isentropic. For the purpose of this analysis, the process is terminated after one reflection since the subsequent reflections are extremely weak and the tube can be considered to have reached ambient pressure conditions.

The detonation wave is a discontinuous combustion wave. It consists of a shock wave sustained by a trailing combustion zone. The detonation wave can be treated similarly to a shock wave, since there exists a detonation adiabat analogous to the shock adiabat [44]. However the detonation wave is only stable at the Chapman–Jouguet point on the detonation adiabat. In the Chapman–Jouguet (CJ) theory, the detonation front is infinitesimally thin like a shock wave. Heat is released within the infinitesimally thin front and thus chemical kinetics are not considered in this theory. The shock adiabat can be derived starting from the continuity, momentum, and energy relations

$$\rho_1 u_1 = \rho_2 u_2 \equiv j \equiv \text{const.} \tag{2.10}$$

$$p_1 + \rho_1 u_1^2 = p_2 + \rho_2 u_2^2 \tag{2.11}$$

$$c_p T_1 + \frac{1}{2} u_1^2 = c_p T_2 + \frac{1}{2} u_2^2 \tag{2.12}$$

The gas state variables which the shock wave moves into are denoted by the subscript 1, while the gas behind the shockwave is denoted by the subscript 2. Using the continuity equation and the definition of specific volume $v = 1/\rho$, the velocities may be written in terms of j, the maximum flux density through the shockwave

$$u_1 = j v_1, \quad u_2 = j v_2 \tag{2.13}$$

Substituting equation (2.13) into the momentum equation and rewriting the equation in terms of the flux density results in

$$p_1 + j^2 v_1 = p_2 + j^2 v_2 \tag{2.14}$$

$$j^2 = (p_2 - p_1)/(v_1 - v_2) \tag{2.15}$$

Since j^2 is always positive, if $p_2 > p_1$, $v_2 > v_1$, or $p_2 < p_1$, $v_2 < v_1$. For a shock wave only the former case can occur ensuring an increase in entropy. Combining equations (2.12), (2.13) and (2.15) yields (2.17)

$$u_1 - u_2 = \sqrt{(p_2 - p_1)(v_1 - v_2)} \tag{2.16}$$

$$e_1 - e_2 + \frac{1}{2}(p_2 + p_1)(v_1 - v_2) = 0 \tag{2.17}$$

These relations are valid for the thermodynamic properties of the two sides across a discontinuity including detonation waves. The detonation adiabat lies above the shock adiabat due to the increase in the heat function e of gases crossing the combustion zone of the detonation wave. The resultant equation 2.17 is the Hugoniot equation discussed earlier in Chapter 1.

The rarefaction wave is formed as the gas expands from a high pressure to a low pressure, and serves as a mechanism for information transfer about boundaries or discontinuities to the surroundings. The leading edge of the rarefaction wave travels at the local speed of sound, while its tail velocity decreases in magnitude to $u_{tail} = a - \frac{1}{2}(\gamma + 1)u_g$ where u_g is the gas velocity behind the discontinuity. The detonation wave is followed by a Taylor rarefaction in order to transfer information about the discontinuity to the gas behind the wave, and to match the thrust wall boundary condition $u_w = 0$.

At the instant the detonation wave reaches the end of the open end of the thrust tube, an unsteady, exhausting rarefaction is formed in order to transfer information to the local gas within the tube, and to match the exit pressure condition $p = p_{amb}$. This exhausting rarefaction travels toward the thrust wall, with the leading characteristic traveling at the sound speed of the gas behind the Taylor rarefaction. The trailing characteristics of the exhausting rarefaction reduce the pressure inside the thrust tube to pressures lower than the far field pressure condition. The exhausting rarefaction reflects off the thrust wall as another unsteady rarefaction toward the open end, etc. These are extremely weak Mach waves and are not considered in the analysis.

2.1.2 Partially-Filled PDE

The partially-filled PDE cycle requires the thrust tube be filled to a desired fill fraction of less than unity. For a one-dimensional problem the fill fraction is defined as

$$ff = \frac{\text{Length of tube filled with reactant}}{\text{Length of tube}} \tag{2.18}$$

In practice, the filled length must be longer than the DDT distance. In the partially-filled PDE, the detonation wave forms similarly to the fully-filled PDE, but transitions to a shock wave within the thrust tube at the mixture interface. Such a situation is depicted schematically in Figure 1.5b which shows a detonation wave propagating to the right toward the mixture interface. The lack of a detonable mixture in a portion of the thrust tube expectedly reduces the mixture specific impulse of the partially-filled PDE, but the additional shock compression of the purge gas increases the fuel specific impulse. The wave diagram of a single cycle for a half-filled PDE is shown in Figure 2.3. As for the fully-filled case, the wave diagram is presented in non-dimensional form.

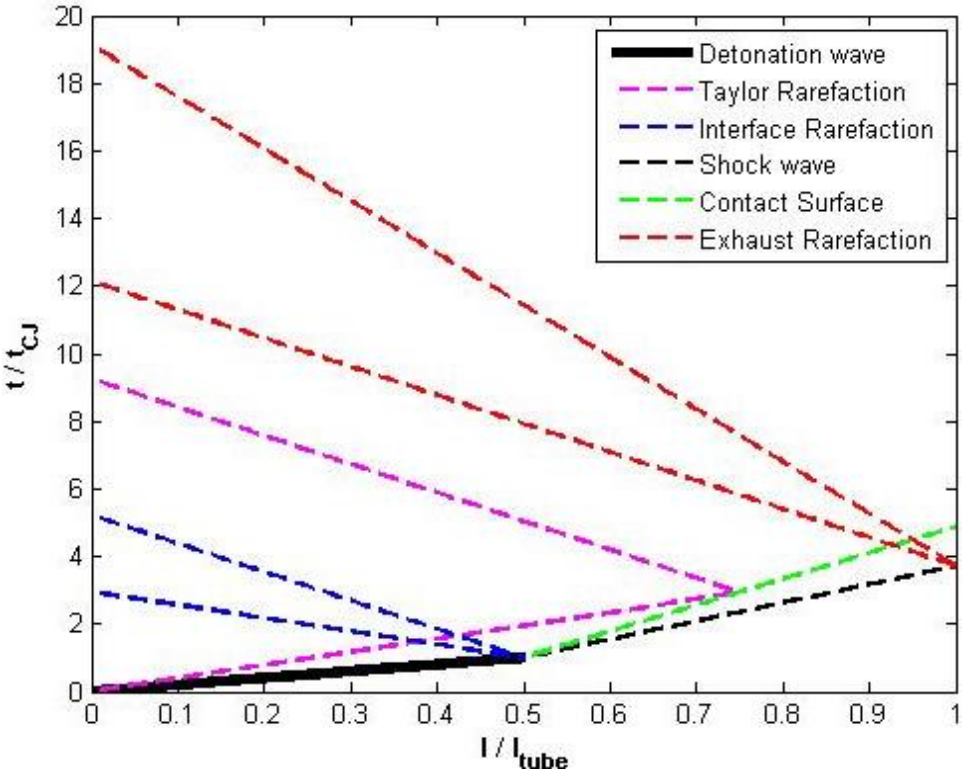

Figure 2.3 Wave diagram for partially-filled PDE.

The detonation wave comprises of a shock wave and the combustion zone, and requires a uniform combustible mixture in order to continue to propagate. In a partially filled PDE, the propagation of the detonation wave is terminated within the tube due to the lack of a combustible mixture needed to sustain the combustion zone. However, the shock wave from the detonation wave propagates into the region of inert gas. The Mach number of the transmitted shock, depends greatly on the properties of the inert gas, but is less than that of the incident detonation wave. In the wave diagram of Figure 2.3, the speed of the transmitted shock can be seen to be lower than the detonation wave. The expansion of the reactants into the inert section causes the mixture interface, also known as contact surface, to move to the right. The Taylor rarefaction that follows the detonation wave continues to propagate in the tube. The trailing edge intersection of the Taylor rarefaction with the

contact surface is shown in Figure 2.3. Intervening waves are not shown for simplicity. The unsteady waves in the Taylor rarefaction are partly reflected back upstream and partly transmitted through the contact surface. Only the reflection of the most downstream wave is shown in the figure. Note that these reflected and transmitted rarefaction waves are weak and they are neglected in the analysis. Finally, the transmitted shock exits the detonation tube, inducing an unsteady expansion wave to propagate upstream.

The Taylor rarefaction formed at the incidence of the detonation wave, continues to propagate after the detonation wave transitions to a shock wave. The Taylor rarefaction reflects off the contact surface between the combustion products and the gas behind the shock wave. This reflection is a weak wave, and its interaction with the gases is neglected, but is shown in Figure 2.3 for completeness.

2.1.3 Performance Parameters

Assessing the performance of the fully- and partially-filled PDE modes of operation is essential for choosing an appropriate approach for various detonation engine applications, namely, electrical power generation or aerospace propulsion. The pressure history at the thrust wall for the fully- and half-filled PDE with stoichiometric oxyhydrogen mixture is presented in Figures 2.4 and 2.5. The impulse of the PDE can be found by integrating the pressure history at the thrust wall over time. The fuel specific impulse and mixture specific impulse of the PDE are used as quantitative measures to evaluate the performance of the PDE.

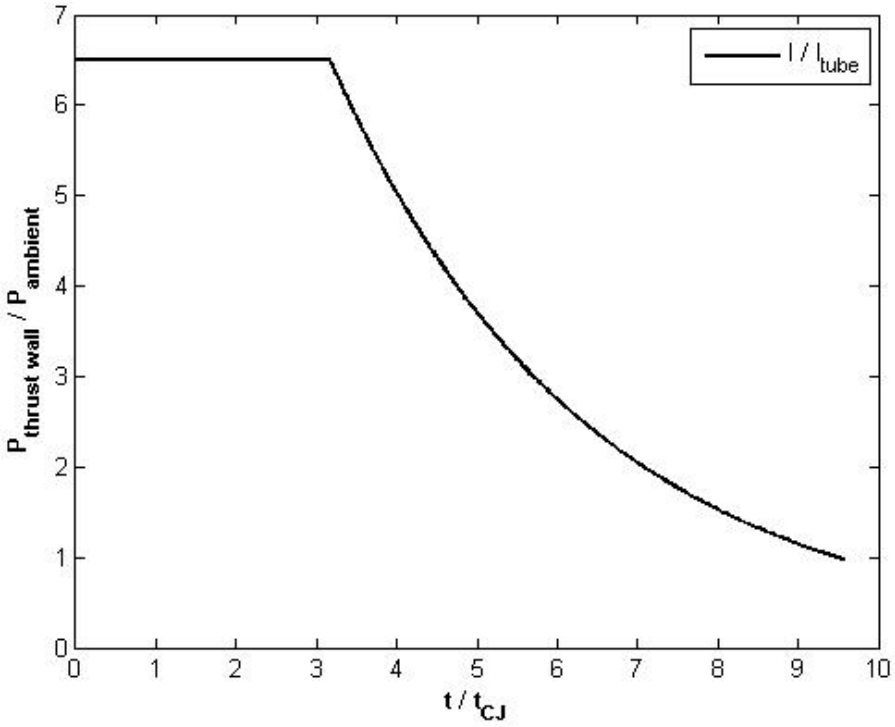

Figure 2.4 Thrust wall pressure history for fully-filled PDE of varying lengths.

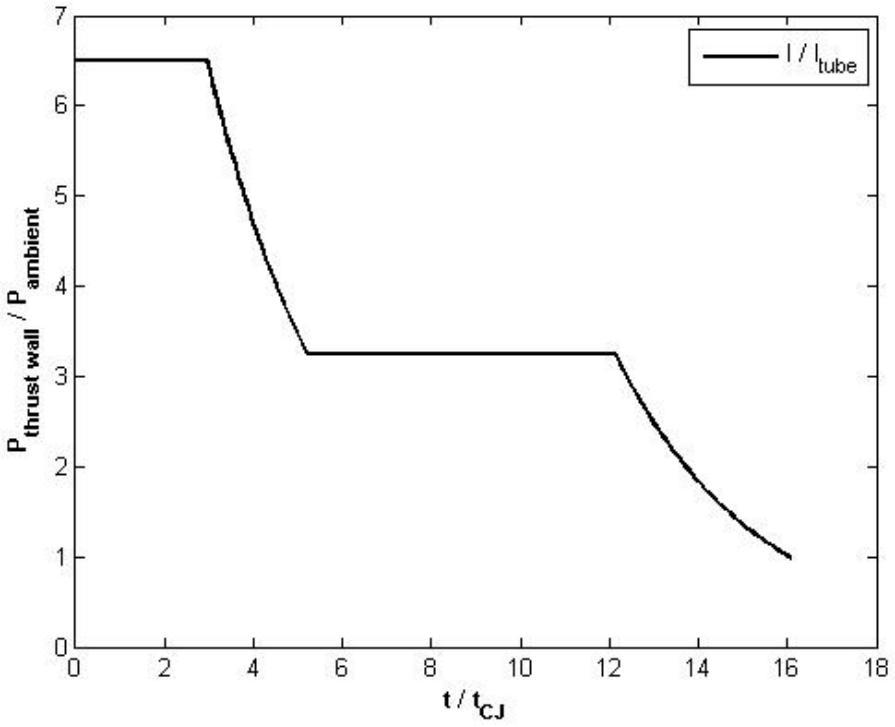

Figure 2.5 Thrust wall pressure history for half-filled PDE of varying lengths.

2.3 Exergy Analysis of Heat Engine Processes

Consider a closed thermodynamic cycle with a perfect gas as the working fluid that undergoes compression 1→2, heat addition 2→3, expansion 3→4, and heat rejection 4→1. This section describes the thermal efficiency and exergy of these work and heat processes.

2.3.1 Compression and Expansion

An isentropic process is one where the entropy remains constant. An adiabatic and internally reversible process results in zero net change in entropy, and is isentropic and optimally efficient. Many well-insulated systems such as compressors, nozzles and turbines operate nearly adiabatically. Additionally these systems, especially those with few moving parts, generate little friction and may be approximated as internally reversible. Isentropic compression or expansion of an ideal gas is

$$\frac{T_2}{T_1} = \left(\frac{p_2}{p_1}\right)^{(\gamma-1)/\gamma} = \frac{T_3}{T_4}$$

A performance metric for compressors is the compression pressure ratio

$$CPR = \frac{p_2}{p_1}$$

The efficiency of a compressor is defined as

$$\eta_{Comp,s} = \frac{\text{Isentropic work}}{\text{Actual work}} = \frac{h_{2,s} - h_1}{h_{2,act} - h_1} = \frac{T_{2,s} - T_1}{T_{2,act} - T_1} \tag{2.19}$$

for an ideal gas. Analogously, the efficiency of a turbine is defined as

$$\eta_{Turb,s} = \frac{\text{Actual work}}{\text{Isentropic work}} = \frac{h_3 - h_{4,act}}{h_3 - h_{4,s}} = \frac{T_3 - T_{4,act}}{T_3 - T_{4,s}} \tag{2.20}$$

such that states 1 and 3 are at the inlets, states 2,*act* and 4,*act* are at the exits, and states 2,*s* and 4,*s* are on the isentrope through to states 1 and 3 respectively for the compressor

and the turbine. The compressor is matched to the turbine, while the remainder of the work output drives a prime mover.

Shock compression is due to convergence of infinitesimal compression waves. For stationary shocks, the Rankine–Hugoniot relations show that flow through a weak shock is nearly isentropic. The efficiency of shock compression is generally defined similarly to the compressor efficiency in equation 2.19, such that state 1 is before the shock, state 2 is after the shock, and state 2s is on the isentrope through state 1. Unsteady, uniform flow with no heat transfer or work is assumed across the shock wave.

2.3.2 Heat Addition and Rejection

Heat can be added or rejected through a constant temperature, constant pressure, constant volume, or constant area process typically referred to as isothermal, isobaric, isochoric, or Rayleigh flow processes. There is no efficiency associated with heat addition and rejection processes because all heat transfer is always assumed to be done for adiabatic systems. For simplicity, air standard cycles are assumed, that is, it is assumed that air is the working gas. A combustor exit temperature is presumed known consistent with the Chapman–Jouguet deflagration or detonation temperature. The combustor pressure loss is disregarded for this analysis.

2.3.3 General Exergy Balance across a Work or Heat Device

The general equations of state at the inlet and outlet for an arbitrary work/heat device are assumed to be at initial state a and b, while the reference environment dead state is 0. The equation of state at a is defined as

$$h_a = c_P(T_a - T_0)$$

and the exergy is

$$\xi_a = (h_a - h_0) + gz_a + \frac{1}{2}(u_a)^2 - T_a(s_a - s_0)$$

The change in exergy across the device is $\Delta\xi_{a\to b}$ and the entropy generated across a device is defined as

$$(s_{Gen})_{a\to b} = s_b - s_a = c_p \ln\left(\frac{T_b}{T_a}\right) - R_{Air} \ln\left(\frac{p_b}{p_a}\right) \tag{2.21}$$

The exergy destruction across the device is defined as

$$(x_{Dest})_{a\to b} = T_0\left(s_{gen}\right)_{a\to b} \tag{2.22}$$

where T_0 is the reference temperature.

2.4 Ideal Thermodynamic Cycle Analysis

By definition, the second law efficiency of a heat engine is the quotient of its cycle efficiency and the ideal efficiency,

$$\eta_{II} = \frac{\eta_I}{\eta_{\text{Carnot}}} \tag{2.23}$$

where the Carnot cycle efficiency is the ideal efficiency. A Carnot cycle engine cannot be built in practice because all real processes generate entropy and are therefore not fully reversible. The Carnot cycle assumes that all four phases (isentropic compression, isothermal heat addition, isentropic expansion, and isothermal heat rejection) in its cycle are reversible processes. Based on this concept of a second law efficiency, a benchmark is established for comparing all heat engines in order to garner insights on their performance [45]. It is worthwhile to perform this comparison through construction of the *p*–*v* and *T*–*s* plots for comparing the three deflagration cycles of interest, namely, the Brayton, Otto and Diesel cycle, against the detonation cycles Zel'dovich–von Neumann–Döring (ZND) and the proposed PDE-LPG cycle. The reference Carnot cycle is included for completeness.

In this analysis, the initial isentropic compression 1→2 is from 1 to 10 atm is uniform for all the cycles considered. Heat addition is through stoichiometric methane–air combustion. Methane is the fuel of choice, serving as a generic hydrocarbon. Finally, the *p*–*v* and corresponding *T*–*s* plots for the Carnot, Brayton, Otto, Diesel, ZND, and PDE-LPG cycles are presented in this section. The heat addition from a stoichiometric methane-air mixture is used for the cycles. An air standard process is assumed for all the cycles where the specific heat ratio $\gamma = 1.4$. The plots for the non-Carnot cycles include the Carnot cycle data that provide a vivid comparison of their relative work outputs.

2.4.1 Carnot Cycle

The Carnot cycle is referred to as the optimal heat engine cycle as it provides the upper limit for the thermodynamic efficiency. In the *p*–*v* and *T*–*s* cycle diagrams for the Carnot cycle shown in Figure 2.6, the working fluid at ambient conditions 1 undergoes isentropic compression 1→2, isothermal heat addition 2→3, isentropic expansion 3→4, and is returned back to ambient condition through isothermal heat rejection 4→1.

The definition of the first law efficiency for a heat engine is

$$\eta_{I-\mathrm{HE}} \triangleq \frac{\Delta W}{Q_{\mathrm{added}}} = 1 - \frac{Q_{\mathrm{rejected}(4\to1)}}{Q_{\mathrm{added}(2\to3)}} \tag{2.24}$$

that is, the quotient of the net work and the heat added, and can be re-expressed as the difference between unity and the quotient of the heat rejected and the heat added as shown in equation 2.24. For the Carnot cycle, heat is added and rejected through isothermals. Therefore, the first law efficiency for a Carnot cycle is

$$\eta_{I-\mathrm{Carnot}} = 1 - \frac{Q_{4\to1}}{Q_{2\to3}} = 1 - \frac{T_1(S_4 - S_1)}{T_3(S_3 - S_2)} = 1 - \frac{T_1}{T_3} \tag{2.25}$$

For any reversible heat engine, as energy is added or rejected, the entropy increases or decreases accordingly as

$$\Delta S_{2\to3} = -\frac{Q_{2\to3}}{T_H} \qquad \text{or} \qquad \Delta S_{4\to1} = -\frac{Q_{4\to1}}{T_C} \tag{2.26}$$

Since no entropy is stored in the working fluid over a cycle, the net entropy production for any heat engine cycle is

$$\frac{Q_{4\to1}}{T_1} - \frac{Q_{2\to3}}{T_3} \geq 0 \to \frac{Q_{4\to1}}{Q_{2\to3}} \geq \frac{T_1}{T_3} \tag{2.27}$$

This inequality can be modified into the heat engine efficiency equation and it becomes clear that the equality represents the reversible Carnot cycle

$$\eta_{I-\text{HE}} = 1 - \frac{Q_{\text{rejected}(4\to1)}}{Q_{\text{added}(2\to3)}} \leq 1 - \frac{T_1}{T_3} = \eta_{I-\text{Carnot}} \tag{2.28}$$

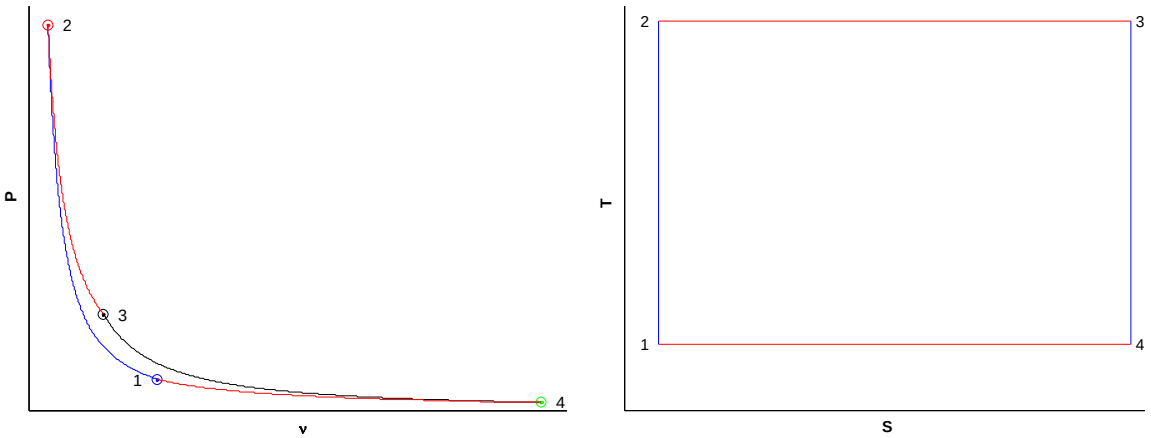

(a) *p*–*v* diagram. (b) *T*–*s* diagram.

Figure 2.6: Carnot cycle.

Applying the second law reveals that the Carnot efficiency is the upper limit for any heat engine operating between the hot and cold temperature reservoirs T_3 and T_1 respectively. The subsequent heat engine cycle diagrams for the Brayton, Otto, Diesel, and ZND cycles are therefore plotted within their corresponding Carnot cycles.

2.4.2 Ideal Brayton Cycle

The Brayton cycle is an all-gas cycle where air and combustion gases are the working fluid with a steady-flow engine consisting of an axial compressor, a deflagration combustor and a turbine. For simplicity of analysis, the composition changes in the combustion gases are neglected, and the air standard cycle is used. The air standard cycle replaces the combustion process with a constant pressure control volume that accepts heat, and maintains air as the working fluid through the entire cycle. Since the environment closes all combustion gas processes, the inlet and exhaust states are joined by an isobaric line. The *p*–*v* and *T*–*s* diagrams for a Brayton cycle are shown in Figure 2.7. The working fluid at the ambient condition 1 undergoes isentropic compression (1→2), isobaric heat addition (2→3), isentropic expansion (3→4), and is returned back to ambient condition through isobaric heat rejection (4→1). The Brayton cycle is a steady flow and steady state system. Therefore the maximum operating cycle temperature T_3 is limited by materials constraints.

The Brayton cycle diagrams are plotted within their Carnot cycles, which graphically represent the deviation from the maximum efficiency. It can be seen in Figure 2.7 (a) that on the same scale, the compression in the Carnot cycle produces a much larger pressure than the Brayton cycle. Increasing the CPR for the Brayton cycle generally increases the ideal cycle efficiency. Further, heat from the exhaust gases can be used to increase the working fluid energy post compression through a regeneration cycle, provided that $T_4 > T_3$.

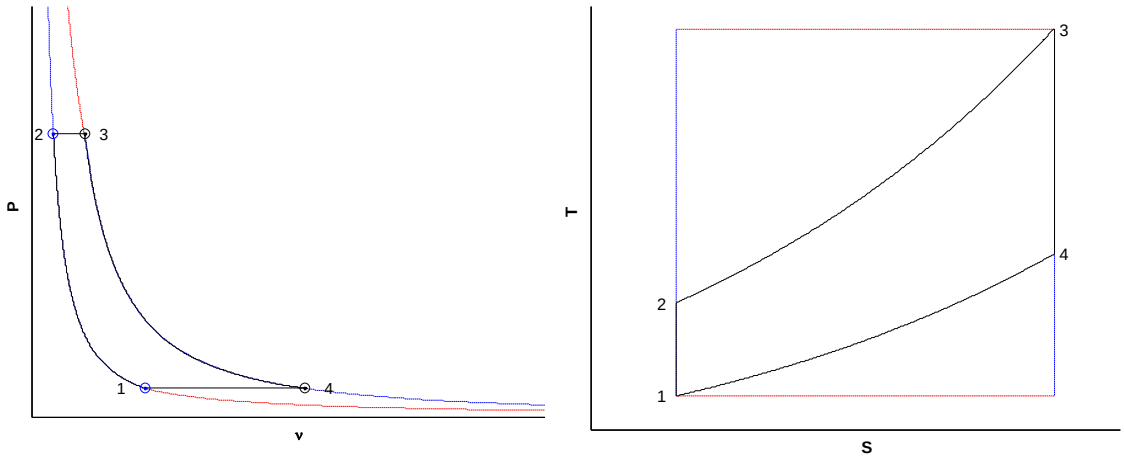

(a) *p–v* diagram. **(b) *T–s* diagram.**

Figure 2.7 Brayton cycle.

The ideal air standard Brayton cycle consists of isobaric heat addition and rejection, and isentropic compression and expansion. It follows that $p_4/p_3 = p_1/p_2$. Therefore the Brayton thermal cycle efficiency can be expressed as

$$\eta_{I-\text{Brayton}} = \frac{(h_3 - h_4) - (h_2 - h_1)}{h_3 - h_2} = \frac{c_p(T_3 - T_4) - c_p(T_2 - T_1)}{c_p(T_3 - T_2)} = 1 - \frac{(T_4 - T_1)}{(T_3 - T_2)} \tag{2.29}$$

which for an ideal gas is further simplified to

$$\eta_{I-\text{Brayton}} = 1 - \frac{T_1}{T_2} = 1 - \left(\frac{p_2}{p_1}\right)^{(1-\gamma)/\gamma} = 1 - r^{(1-\gamma)/\gamma} \tag{2.30}$$

where $r = p_2/p_1$ is the CPR.

Another way to describe the performance of the Brayton cycle is the back work ratio; the ratio of the compressor work required to generate the corresponding turbine work. The back work ratio is

$$\text{BWR} = \frac{\dot{W}_c/\dot{m}_2}{\dot{W}_t/\dot{m}_4} = \frac{h_2 - h_1}{h_3 - h_4} \tag{2.31}$$

It can be noted that a large portion of the turbine work is required to drive the compressor due to the higher specific volume of gas flowing through a compressor. This is in contrast to vapor pressure cycles with equivalent compression ratios. Typical back work ratios of gas turbines range from 40 to 80%, in contrast to 1 to 2% for vapor power plants.

2.4.3 Ideal Otto Cycle

The ideal Otto cycle is also an all-gas cycle where air and combustion gases are the working fluid in a reciprocating internal combustion engine consisting of a piston that moves within a cylinder fitted with intake and exhaust valves. To simplify the analysis the composition changes in the combustion gases are neglected, and the air standard cycle is used. The air standard Otto cycle assumes that heat addition occurs instantaneously within a control volume, and maintains air as the working fluid through the entire cycle. Since the stroke length of the piston is define the maximum volumetric compression or expansion, the inlet and exhaust states are joined by a constant volume line.

In *p*–*v* and *T*–*s* diagrams for the Otto cycle are shown in Figure 2.8. The working fluid at 1 undergoes, isentropic compression 1→2, isochoric heat addition 2→3, isentropic expansion 3→4, and is returned back to ambient condition through isochoric heat rejection 4→1. Similarly to the Brayton cycle, including the Carnot cycle operating at the same reservoir conditions shows a much larger CPR for the latter.

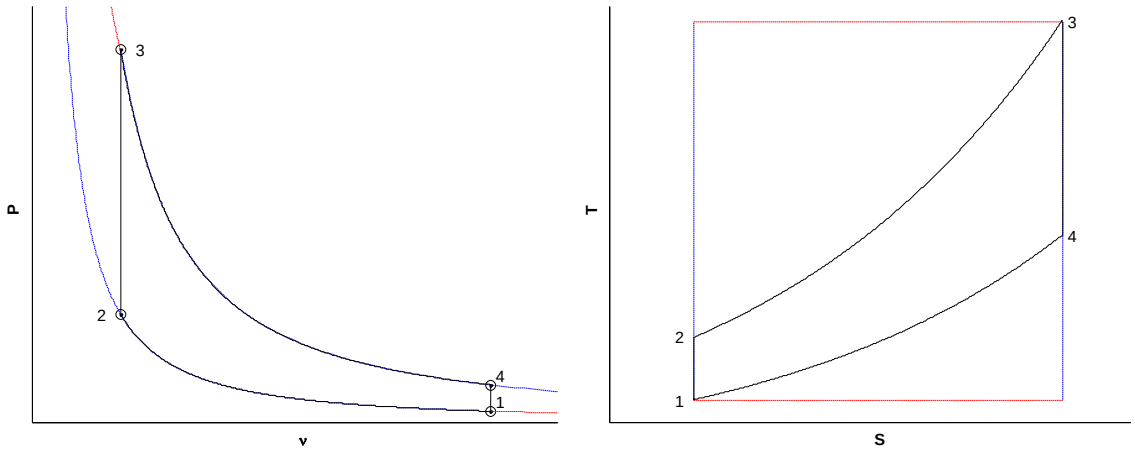

(a) *p–v* diagram. **(b) *T–s* diagram.**

Figure 2.8 Otto cycle.

Since air flows through the heat exchangers at constant volume, it follows that $v_2/v_1 = v_3/v_4$. Therefore, the Otto thermal cycle efficiency, following the derivation for the Brayton cycle, can be simplified as

$$\eta_{I-\text{Otto}} = \frac{(e_3 - e_2) - (e_4 - e_1)}{e_3 - e_2} = \frac{c_v(T_3 - T_2) - c_v(T_4 - T_1)}{c_v(T_3 - T_2)}$$

$$= 1 - \frac{(T_4 - T_1)}{(T_3 - T_2)}$$

$$= 1 - \frac{T_1}{T_2} = 1 - \left(\frac{p_2}{p_1}\right)^{(1-\gamma)/\gamma} = 1 - r^{(1-\gamma)/\gamma} \tag{2.32}$$

Note that since $v_3 = v_2$ and $v_4 = v_1$, $r = v_1/v_2 = v_4/v_3$.

The maximum operating temperature T_3 can be over 2000 K for an Otto cycle due to the reciprocating nature of the internal combustion engine, but is also limited by material considerations. High compression ratios improve the efficiency of the Otto cycle, but in a practical engine, the compression ratio is limited by the fuel–air ignition temperature in order to prevent auto-ignition of fuel before maximum design compression is reached.

2.4.4 Ideal Diesel Cycle

The Diesel cycle is another all-gas cycle where air and combustion gases are the working fluid in a reciprocating internal combustion engine consisting of a piston that moves within a cylinder fitted with intake and exhaust valves. For simplifying the analysis, the composition changes in the combustion gases are neglected, and the air standard cycle is used for the analysis of the cyclic processes.

The Diesel air standard cycle replaces the combustion process with isobaric heating. Since the stroke length of the piston defines the maximum volumetric compression or expansion, the inlet and exhaust states are joined by a constant volume line. The details of the cycle are shown in Figure 2.9.

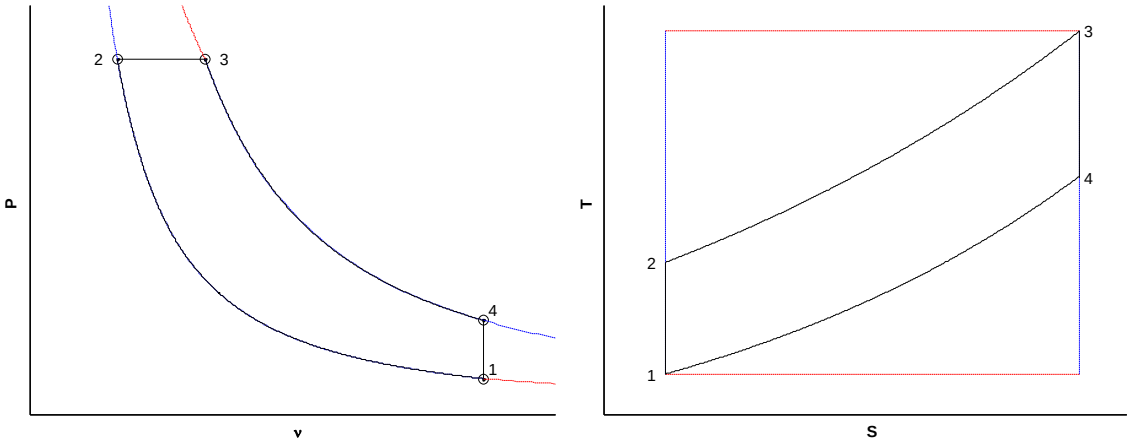

(a) *p–v* diagram. **(b) *T–s* diagram.**

Figure 2.9 Diesel cycle.

The working fluid at 1 undergoes isentropic compression 1→2, isobaric heat addition 2→3, isentropic expansion 3→4, and is returned back to ambient condition through isochoric heat rejection 4→1. For the isentropic processes 1→2 and 3→4, there is work with no heat transfer, while for the isochoric processes 4→1, there is heat transfer

with no work. For the isobaric process 2→3 there is both work and heat transfer, the end of which marks the beginning of the power stroke 3→4. Since the working gas flows through the heat exchange at constant pressure and constant volume, it follows that $p_3 = p_2$ and $v_1 = v_4$. Therefore the Diesel thermal cycle efficiency can be simplified as:

$$\eta_{I-\text{Diesel}} = \frac{(h_3 - h_2) - (e_4 - e_1)}{h_3 - h_2} = \frac{c_p(T_3 - T_2) - c_v(T_4 - T_1)}{p(T_3 - T_2)}$$

$$= 1 - \frac{c_v(T_4 - T_1)}{c_p(T_3 - T_2)} \tag{2.33}$$

(2.34)

$$= 1 - \frac{T_1}{T_2}\left[\frac{r_c^{\gamma} - 1}{\gamma(r_c - 1)}\right] \tag{2.35}$$

$$= 1 - r^{(1-\gamma)}\left[\frac{r_c^{\gamma} - 1}{\gamma(r_c - 1)}\right]$$

where $r = v_1/v_2 = p_2/p_1$ is the compression ratio and $r_c = v_3/v_2$ is the cutoff ratio.

The Diesel cycle reduces to the Otto cycle when $r_c = 1$. Although, the Diesel cycle is a reciprocating flow system similar to the Otto cycle, its maximum operating cycle temperature T_3 is lower because heat is added more gradually over the constant pressure process. High compression ratios improve the efficiency of the Diesel cycle. This can achieved in practice because only air is compressed therefore there is no auto-ignition before maximum design compression is reached.

2.4.5 Ideal ZND Cycle

The ZND cycle is an all-gas cycle where air and combustion gases are the working fluid in a steady flow engine consisting of an axial compressor, detonation combustor, and turbine. For simplifying the analysis, air is assumed to be the working fluid. The air standard ZND cycle *p–v* and *T–s* processes are shown in Figure 2.10. The working fluid

at 1 undergoes isentropic compression 1→2, shock compression 2→2h, Rayleigh heat addition 2h→3, isentropic expansion 3→4, and is returned back to ambient condition through isobaric heat rejection 4→1. It can be noted that the initial isentropic compression is typically not included in previous analysis of the ZND cycle. However, a practical engine will likely include an initial compression stage to draw in air and also to raise efficiency. For the present analysis, a CPR of 10 is included.

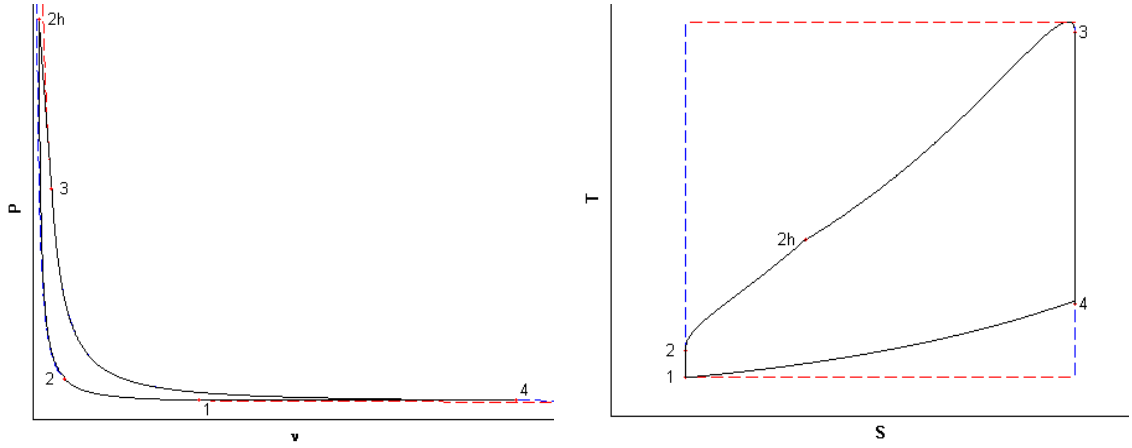

(a) *p–v* diagram. **(b) *T–s* diagram.**

Figure 2.10 ZND cycle

For the ZND cycle, after the conventional isentropic compression 1→2, the working fluid passes through a shockwave which compress it up to ZND point on the Hugoniot curve 2→2h. Shockwave compression generates the maximum amount of entropy associated with a compression process in contrast to an isentropic compression which generates no entropy. The ZND cycle heat addition is through the Rayleigh flow process 2h→3 that considers heat addition through a constant area duct for adiabatic flow. This heat addition process causes the flow Mach number to approach unity, eventually thermally choking the flow. Unlike the other classical thermodynamic cycles, the

maximum temperature in the cycle T_{Hot} does not correspond with the temperature $T_{s,max}$ of maximum entropy. The algebraic solution for the Mach number and entropy rise for a CJ detonation wave, has been derived by [46, 47] and is given by

$$M_{CJ}^2 = a + \sqrt{a^2 - 1} \tag{2.36}$$

where $a = (\gamma + 1)(\tilde{q}/\psi) + 1$, $\tilde{q} \equiv Q_{\mathrm{added}(2\to3)}/c_pT_0 = fh_{PR}/c_pT_0$ and

$$\frac{s_3 - s_2}{c_p} = -\ln\left[M_{CJ}^2\left(\frac{\gamma+1}{1+\gamma M_{CJ}^2}\right)^{(\gamma+1)/\gamma}\right] \tag{2.37}$$

The constant pressure heat rejection becomes

$$Q_{\mathrm{rejected}(4\to1)} = h_4 - h_1 = c_p(T_4 - T_1) = c_pT_0\left[\exp\left(\frac{s_4 - s_1}{c_p}\right) - 1\right] \tag{2.38}$$

$$= c_pT_0\left[\exp\left(\frac{s_3 - s_2}{c_p}\right) - 1\right]$$

$$= c_pT_0\left[\frac{1}{M_{CJ}^2}\left(\frac{1+\gamma M_{CJ}^2}{\gamma+1}\right)^{(\gamma+1)/\gamma} - 1\right] \tag{2.39}$$

Hence, the ZND thermal cycle efficiency is

$$\eta_{I-ZND} = 1 - \frac{Q_{\mathrm{rejected}(4\to1)}}{Q_{\mathrm{added}(2\to3)}} = 1 - \left[\frac{1}{M_{CJ}^2}\left(\frac{1+\gamma M_{CJ}^2}{\gamma+1}\right)^{(\gamma+1)/\gamma} - 1\right]\Big/\tilde{q} \tag{2.40}$$

The ZND cycle heat rejection 4→1 is through an isobaric process similar to the Brayton cycle. Moreover, it is possible to conceive a new cycle that employs the same shock compression and Rayleigh heat addition process of the ZND cycle, but where heat is rejected through an isochoric process ($v_4 = v_1$) similar to the Otto and Diesel cycles. This new cycle is proposed as the proper description of the operation of the PDE-LPG

because of the finite volumes created by the piston configuration and is presented in section 2.4.6 below.

2.4.6 Ideal PDE-LPG Cycle

The proposed PDE-LPG cycle is an all gas cycle where air and combustion gases are the working fluid in a pulsed flow, reciprocating internal combustion engine consisting of a piston that moves within a fitted cylinder, and with intake and exhaust valves on a detonation tube. For simplifying the analysis, the composition changes in the combustion gases are neglected, and the air standard cycle is used for the analysis of the cyclic processes. The air standard PDE-LPG cycle *p*–*v* and *T*–*s* processes are shown in Figure 2.11. Similar to the ZND cycle, the working fluid at 1 undergoes isentropic compression 1→2, shock compression 2→2h, Rayleigh heat addition 2h→3, isentropic expansion 3→4, but is returned back to ambient condition through isochoric heat rejection 4→1. This detonation engine reciprocating piston configuration is more practical for a high initial compression which is desirable to draw in air and also to raise efficiency. For the present analysis, a CPR of 10 is included.

The proposed PDE-LPG cycle goes through similar processes of compression, heat addition, and expansion as the ZND cycle. However, since its heat rejection process is isochoric in contrast to the ZND cycle's isobaric heat rejection, the PDE-LPG yields a slightly lower cycle efficiency for equivalent pressure ratio. The derivation presented earlier in section 2.4.5 for the thermal efficiency of the ZND cycle is also valid for the proposed PDE-LPG cycle with a slight modification of the value the non-dimensional heat addition $\widetilde{q}$. The value of c_p is replaced with c_v, as isobaric heat rejection is replaced with

isochoric heat rejection, enthalpy is replaced with internal energy, and the non-dimensional heat addition becomes $\tilde{q} = f h_{PR}/c_v T_0$. The constant volume heat rejection becomes

$$Q_{\text{rejected}(4\to1)} = e_4 - e_1 = c_v(T_4 - T_1) = c_v T_0 \left[\exp\left(\frac{s_4 - s_1}{c_p}\right) - 1\right] \tag{2.41}$$

$$= c_v T_0 \left[\exp\left(\frac{s_3 - s_2}{c_p}\right) - 1\right]$$

$$= c_v T_0 \left[\frac{1}{M_{CJ}^2}\left(\frac{1+\gamma M_{CJ}^2}{\gamma+1}\right)^{(\gamma+1)/\gamma} - 1\right] \tag{2.42}$$

Hence, the PDE-LPG thermal cycle efficiency is

$$\eta_{I-PDE-LPG} = 1 - \frac{Q_{\text{rejected}(4\to1)}}{Q_{\text{added}(2\to3)}} = 1 - \left[\frac{1}{M_{CJ}^2}\left(\frac{1+\gamma M_{CJ}^2}{\gamma+1}\right)^{(\gamma+1)/\gamma} - 1\right] \Big/ \tilde{q} \tag{2.43}$$

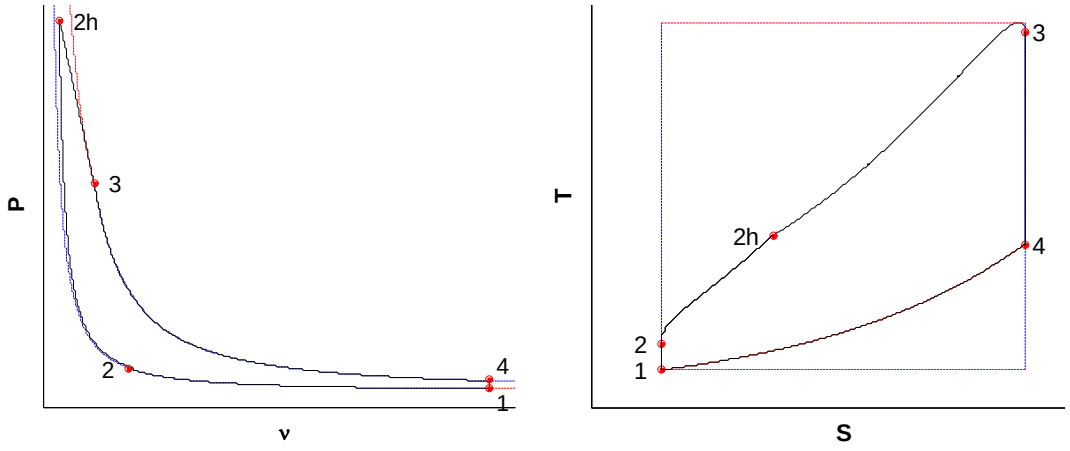

(a) *p–v* diagram. **(b) *T–s* diagram.**

Figure 2.11 PDE-LPG cycle

This proposed new cycle is similar to the Otto and diesel cycles which are also reciprocating piston engines and all rejected heat isochorically. The *p–v* diagrams in figure 2.10 and 2.11 clearly show the missing area or work missing from the PDE-LPG cycle

compared to the ZND cycle. Practical operation of a PDE at a high compression ratio with the ZND cycle is difficult to achieve because it requires a high back pressure. However, operation of a high compression ratio can easily be achieved for the PDE-LPG with confinement of the reciprocating piston.

2.4.7 Comparisons of Heat Engine Thermodynamic Cycles

All heat engines cycles are based on performing compression, heat addition, expansion, and heat rejection, but these tasks may be achieved through different thermodynamic processes such as isobaric and isochoric. It is generally assumed that the working fluid for ideal cycles of all heat engines undergoes isentropic compression 1→2 and isentropic expansion 3→4. Therefore, the primary differences between classical thermodynamic heat engine cycles are the processes by which heat is added 2→3 and rejected 4→1.

For the Carnot cycle, heat is added 2→3 and rejected 4→1 through a pair of isothermal processes. But they are a pair of isobaric processes for the Brayton cycle and a pair of isochoric processes for the Otto cycle. The Diesel cycle operates as a hybrid of the Brayton and Otto cycles because it employs an isobaric process for heat addition 2→3 similar to the Brayton cycle, and an isochoric process for heat rejection 4→1 similar to the Otto cycle. For these ideal thermodynamic cycles, it is important to note that heat is simply added to the working fluid, and combustion processes where fluid composition is changed are not considered.

For the ZND cycle, the working fluid passes through a shockwave which compresses it up to ZND point on the Hugoniot curve 2→2h. The ZND cycle heat addition is through the Rayleigh flow process 2h→3 that considers heat addition through a constant

area duct for adiabatic flow. Heat is rejected 4→1 through an isobaric process similar to the Brayton cycle. The proposed PDE-LPG cycle operates as a hybrid of the ZND and Otto cycles because it employs shockwave compression 2→2h and Rayleigh flow process for heat addition similar to the ZND cycle, and an isochoric process for heat rejection 4→1 similar to the Otto cycle.

The thermodynamic states of the working fluid changes during a cycle, but not its composition. Internal combustion engines do not perform a thermodynamic cycle because matter is introduced as reactant composition and discharged at a different product composition after combustion.

The thermal efficiency of a heat engine is the ratio of the net work of a cycle to the added heat

$$\eta_I = \frac{\Delta W}{Q_{\text{added}}} \tag{2.44}$$

The subscript *I* indicates that this is the "first-law efficiency" to distinguish it against the "second-law efficiency" which will be discussed later. It may be more intuitive to restate this as the difference between unity and the ratio of the rejected heat to the added heat

$$\eta_I = 1 - \frac{Q_{\text{rejected}(4\to1)}}{Q_{\text{added}(2\to3)}} \tag{2.45}$$

The net work can be evaluated by examining the enclosed area of the *p*–*v* cycle, but it is obviously not possible to graphically present the heat added in the *p*–*v* plots because the values of internal energy are not represented.

However using the T-s plots, the added heat is the area below the top lines adjoining the vertical isentropic lines (2→3) to the entropy axis, while the rejected heat is the area

below the bottom line adjoining the vertical isentropic lines (4→1) to the entropy axis. The area encompassed by a cycle in the T-S plot is the portion of added heat converted to work.

Applying these principles to heat engine cycles, the thermal efficiencies can be easily derived based on the processes for added and rejected heat. These thermal efficiency equations are listed in Table 2.2. The variation of η_I with CPR is plotted in Figure 2.12. This plot shows that the first-law efficiency of the ZND cycle is generally higher than those of the other cycles for the same CPR. The proposed PDE-LPG cycle follows the same efficiency trend as the ZND cycle, but has thermal efficiencies that are at maximum 3.4% lower than the ZND cycle for equivalent CPR. The Otto and Brayton cycles result in the same thermal efficiency while the Diesel cycle results in lower thermal efficiency than the other cycles for equivalent CPR.

Table 2.2 Heat processes and first-law thermal efficiency equations.

Cycle	***Heat addition Process***	***Heat rejection Process***	***Thermal Efficiency*** $\boldsymbol{\eta_I = 1 - Q_{4\to1}/Q_{2\to3}}$
Carnot	Isothermal	Isothermal	$\eta_I = 1 - \frac{T_1(S_3 - S_1)}{T_3(S_3 - S_1)}$
Brayton	Isobaric	Isobaric	$\eta_I = 1 - \frac{h_4 - h_1}{h_3 - h_2}$
Otto	Isochoric	Isochoric	$\eta_I = 1 - \frac{e_4 - e_1}{e_3 - e_2}$
Diesel	Isobaric	Isochoric	$\eta_I = 1 - \frac{e_4 - e_1}{h_3 - h_2}$
ZND	Shock Hugoniot; Rayleigh Flow	Isobaric	$\eta_I = 1 - \frac{h_4 - h_1}{Q_{shock} + Q_{Rayleigh}}$
PDE-LPG	Shock Hugoniot; Rayleigh Flow	Isochoric	$\eta_I = 1 - \frac{e_4 - e_1}{Q_{shock} + Q_{Rayleigh}}$

The general second-law efficiency or "effectiveness" η_{II} of the engines considered here (Brayton, Otto, Diesel, ZND, and PDE-LPG) is

$$\eta_{II-\text{real}} = \frac{\eta_{I-\text{real}}}{\eta_{I-\text{Carnot}}} = \frac{1 - T_1/T_2}{1 - T_1/T_3} \tag{2.46}$$

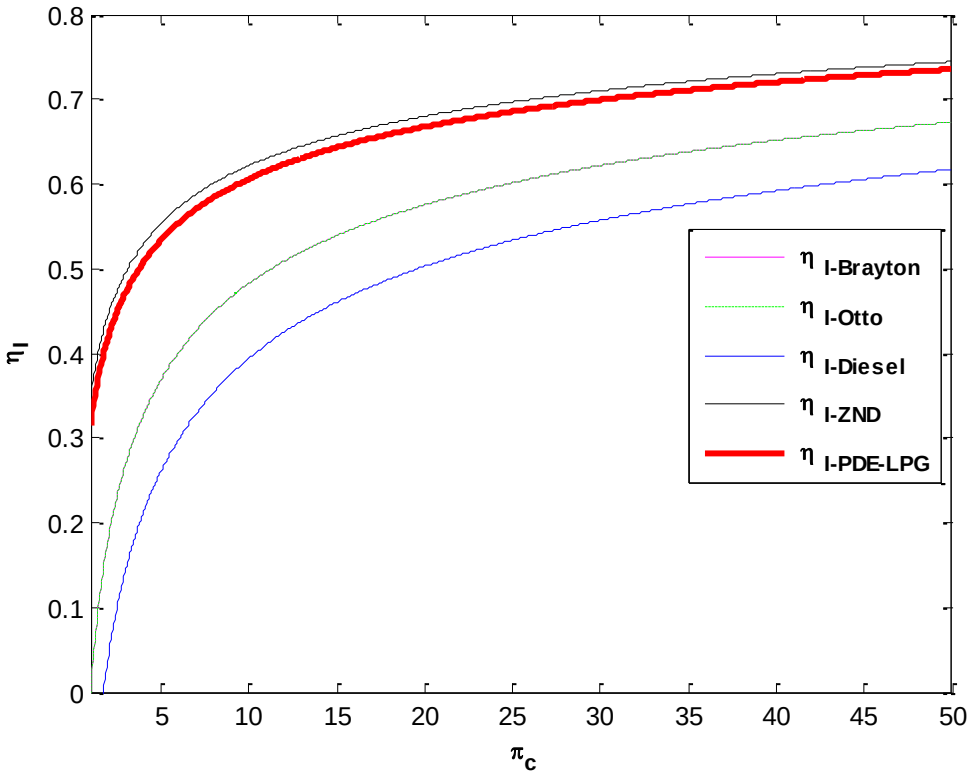

Figure 2.12 First-law efficiency for ideal Brayton, Otto, Diesel, ZND, and PDE-LPG cycles.

In other words, it is the ratio of the first-law efficiency of the cycle to that of the Carnot cycle. In the limit that $T_2 \to T_3$, $\eta_{II} \to 1$. Therefore higher compressor pressure ratios result in higher effectiveness. Using the equations listed in Table 1, the second-law efficiency for the real engines considered are plotted as a function of CPR in Figure 2.13. This plot reveals that the effectiveness of the ZND cycle is generally higher than other real engine cycles for equivalent CPR up to 30. The proposed PDE-LPG cycle also follows the

same effectiveness trend as the ZND cycle, but has second law efficiencies that are at maximum 3.6% lower than the ZND cycle for equivalent CPR. The Brayton and Diesel cycle effectiveness rise much faster at higher compression ratio due to their low turbine inlet temperature ratios. Therefore there exists a balance between increasing turbine inlet temperature T_3 to increase first-law efficiency, which therefore decreases the rate of increase of the second-law efficiency at higher CPR.

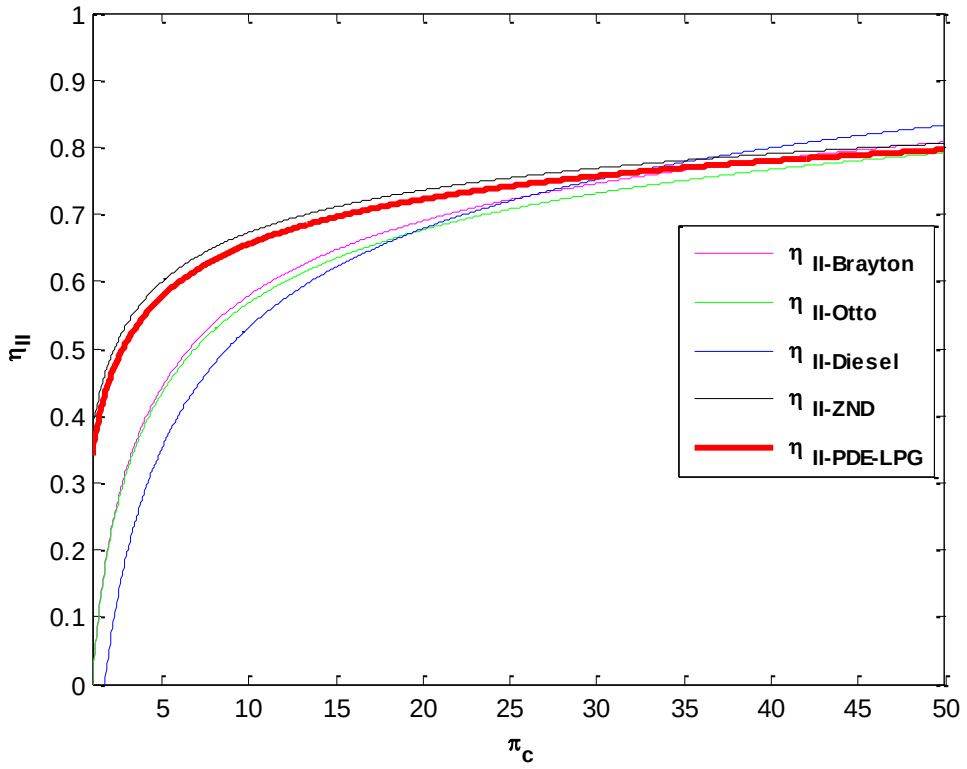

Figure 2.13 Second-law efficiency for ideal Brayton, Otto, Diesel, ZND, and PDE-LPG cycles.

For a given turbine inlet temperature T_3, the optimal compressor pressure ratio for maximum work from the Brayton cycle is derived by differentiating the energy equation with respect to CPR. It is important to note that the second-law efficiency aims at optimizing a system by minimizing entropy generation which can be derived from solving

for the minima of the exergy balance equation. It can be further noted that the minimal entropy condition is not necessarily coincidental with the optimal condition for maximum work or maximum first law efficiency.

It is important to determine which optimal condition is desirable for a given operation. For example in aircraft design where engine power-to-weight ratio is primal, it is preferable to design for maximum work output, but for power generation where the levelized cost of electricity (LCOE) is of primary concern, design for minimization of lost work (entropy generation) is desirable.

CHAPTER 3

Experimental Setup

3.1 Description of Experimental Setup

3.1.1 Detailed Description of Experimental Setup

A mobile pulse detonation engine linear power generator (PDE-LPG) facility was developed. The major components of this facility include a PDE tube, a gas cart, a diverging nozzle, a piston, and a linear power generator. The full facility was built in four incremental phases shown in Figure 3.1. The PDE tube was previously used for the study of unsteady thrust measurements, but has been heavily modified for this present research [48]. Various parts of the facility are labeled in the figure for easy reference. This incremental development scheme of the facility was essential in order to perform experiments to independently measure the performance of the various subsystems before they are fully integrated.

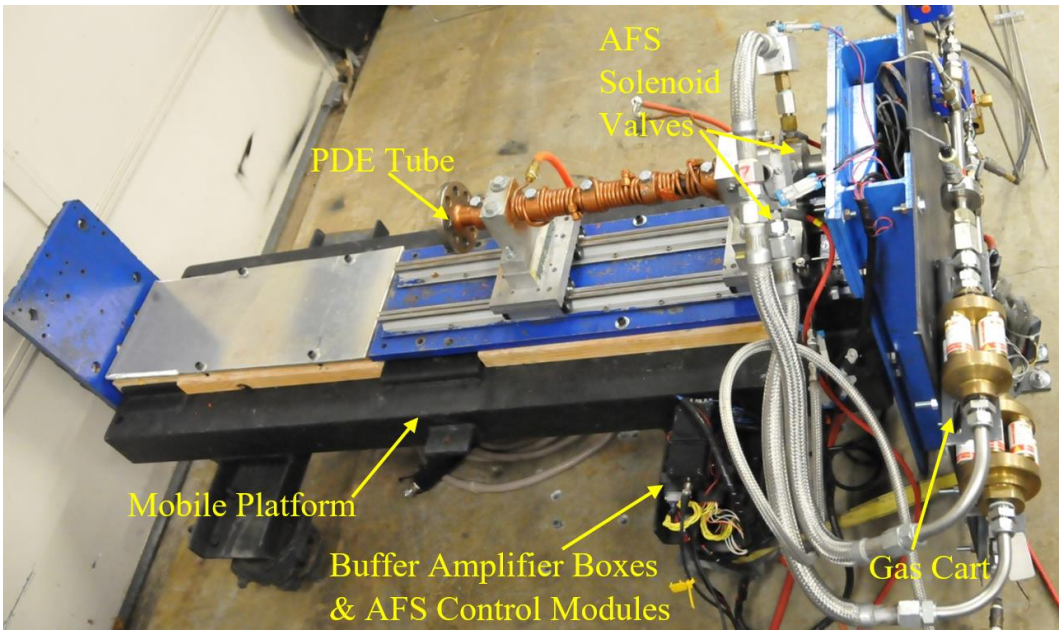

(a) Mobile PDE system – first phase

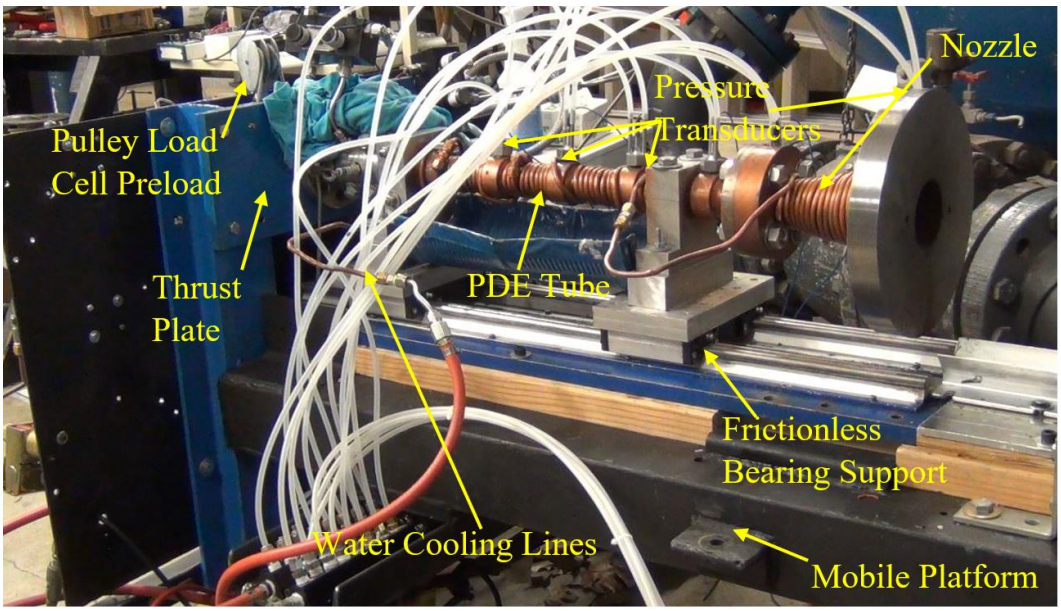

(b) Mobile PDE with nozzle – second phase

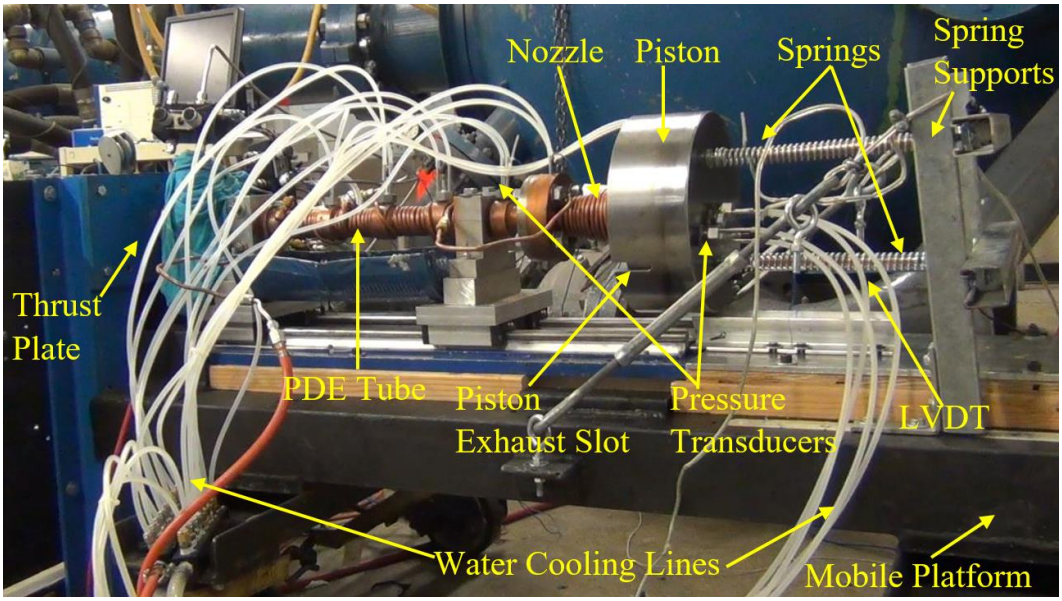

(c) Mobile PDE with nozzle and piston – third phase

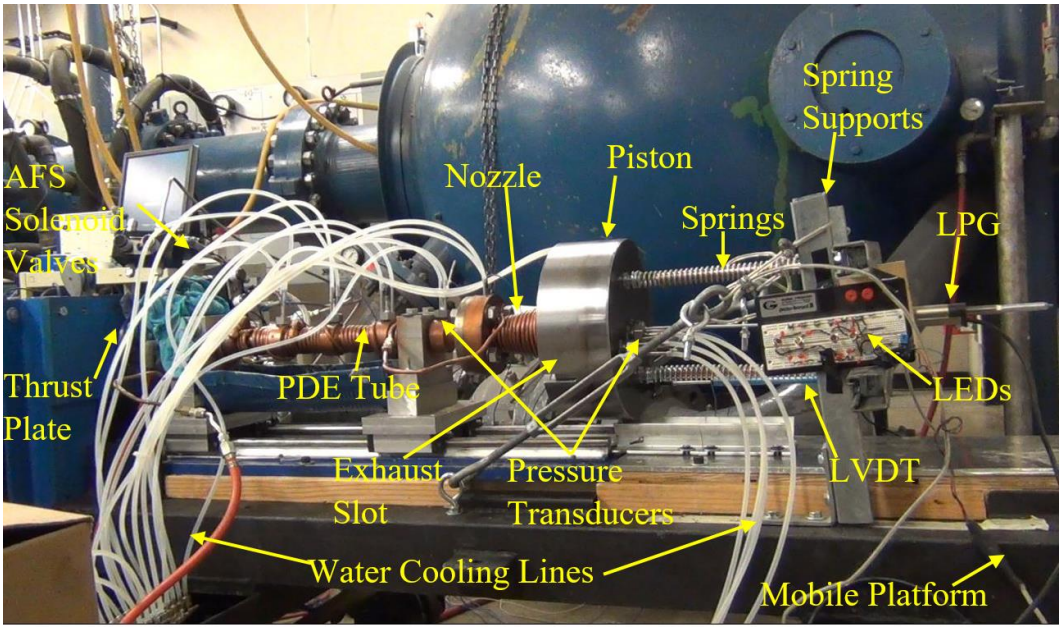

(d) Complete PDE-LPG facility– fourth phase

Figure 3.1 Incremental development of mobile PDE-LPG facility.

The first configuration, a mobile PDE system shown in Figure 3.1a is at the heart of the PDE-LPG facility. This configuration consists of a PDE, a gas cart, and a pair of buffer amplifier boxes all mounted to a mobile platform. The gas cart allows for the measurement of the gas pressure and temperature injected into the PDE. The buffer amplifier boxes are required to generate high peak currents required for the fast opening of solenoid valves attached to the PDE. The PDE itself consists of a 1 in. ID stainless steel tube that is 26 in. long. The tube is open at one end and closed at the other. The closed end serves as the thrust wall. Gaseous fuel and oxidizer are injected into the PDE tube from the closed end and are ignited creating a strong deflagration wave. A deflagration-to-detonation transition (DDT) device is placed within the detonation tube in order to achieve reliable detonations. The detonation wave and the combustion products travel toward the PDE exit providing thrust.

A load-cell (PCB Model 201B02) is mounted between the PDE thrust wall and the mobile platform's thrust plate (Figure 3.1b). A preload of 200 lbs. is applied to the PDE against the thrust wall with a mechanism consisting of a pulley and 0.25 in. thick steel tension cables. The PDE is supported by four 5 in. long frictionless linear roller bearings which allow it to slide back and forth on two 35.5 in. long guide rails manufactured by Techno-Isle Inc.

This first configuration allows for performance measurements of the PDE's thrust, specific impulse, and static pressure of the detonation wave along the detonation tube. Similar measurements were performed in the second configuration shown in Figure 3.1b, which adds a nozzle to the mobile PDE system. In addition, static pressure measurements were performed at the nozzle throat and nozzle exit, which allow for the performance of the nozzle on the PDE to be calculated. Comparisons between the specific impulse performance of the PDE and the PDE with nozzle systems are presented in Chapter 4.

The third configuration shown in Figure 3.1c shows the attachment of a piston-spring system axially aligned through the center of the combined PDE-nozzle system. In this configuration, the pulse firing of the engine displaces the piston away from the thrust wall and the piston is returned back to its nominal position by springs. The combustion products are exhausted from the PDE-piston confinement through exhaust slots on the cylindrical edge of the piston. The piston is simply supported by three sets of screw ball bearings in the piston, that roll on groves etched 120^{o} apart on the large exit nozzle flange visible in the second configuration. The piston is attached to two piano wire springs by 3/8 in. diameter bolts. The springs are bolted to a set of C-channels which are in turn bolted and tensioned with struts to the mobile platform.

Pressure is measured on the piston face at the center and 3 in. away, in order to obtain the PDE pressure work on the piston. The displacement of the piston is measured with a Penny+Giles (SLS130/125/5K/C/50/1) linear variable displacement transducer (LVDT), in order to obtain the thermomechanical performance of this SDOF system described in Chapter 2. This configuration does not allow for meaningful force measurements at the thrust wall due to the presence of the piston at the exit. In this configuration, the pressure measurements along the PDE and nozzle are included with pressure measurements on the piston face. The configuration allows for the independent measurement of the piston-spring system displacement response in order to determine thermomechanical performance without a load.

The fourth configuration in Figure 3.1d shows the attachment of a linear power generator (LPG) system axially aligned through the PDE-nozzle-piston system. In this configuration, the piston and the LPG magnetic slider are displaced axially away from the thrust wall due to the pulse firing of the PDE and returned by springs. The motion of the LPG slider through the LPG stator generates an emf or voltage in the stator coils. The terminal leads of the LPG are connected to an electrical load and shunt resistor circuit, in order to measure electrical current. The electrical power output of the PDE-LPG system is calculated from simultaneous measurement of voltage and current. For qualitative demonstration of continuous electric power generation by the PDE, the LPG was connected to a circuit of diode bridges and capacitors in order to provide the DC voltage for LEDs which light up during the PDE operation. This fourth configuration does not allow for force measurement at the thrust wall or pressure measurement at the piston center. All other previous pressure and displacement measurements are performed. The overall PDE-LPG

system performance which relates the fuel energy input to the electrical energy output is measured in this configuration.

The pressure along the detonation tube, nozzle, and on the piston face are measured using piezoelectric pressure transducers (PCB Model 111A24) placed in flush-mounted water-cooled jackets (PCB Model 064B02) on the PDE and piston, and recessed water-cooled jackets (PCB Model 064B01) in the nozzle throat and exit flange. Cool tap water flows in and out to each of the pressure transducer jackets through ¼ in. plastic tube fittings. A heat exchanger made of copper tubes wound around the PDE tube and nozzle through which water flows removes the heat transferred to the wall by the combustion. The piston face is not cooled because the burned gases are considerable cooled by the expansion through the nozzle, and the total residence time of the hot gases on the piston face as it moves away from the thrust wall during operation is very short.

On the PDE tube, the ignition source, the fuel, oxidizer, purge air gas injection section are located by the thrust wall. The igniter is an automotive Champion Copper Plus® sparks plug that can only initiate a deflagration wave. The in-house igniter consists of a capacitor bank that is charged by an ordinary 120 V, 60 Hz outlet. It can deliver over 25 kV. The deflagration wave is accelerated to a detonation wave by a Shchelkin spiral, shown in Figure 3.2. This deflagration-to-detonation (DDT) device is secured in the tube injection section by the thrust wall. The spiral used is 6.075 in. long, with an outer diameter of 0.961 in., an inner diameter of 0.530 in., and a pitch of 0.239 in. A long spiral and small pitch ensure that the deflagration flame is accelerated to over the critical, half of the CJ velocity required for DDT. A key parameter in choosing an effective spiral is the blockage ratio, which is defined as the ratio of the area obstructed by the DDT device to the area of the

detonation tube. The blockage ratio of the spiral used is 36%, and previous studies have indicated that a blockage ratios in the range of 40% is desired for enabling DDT [3].

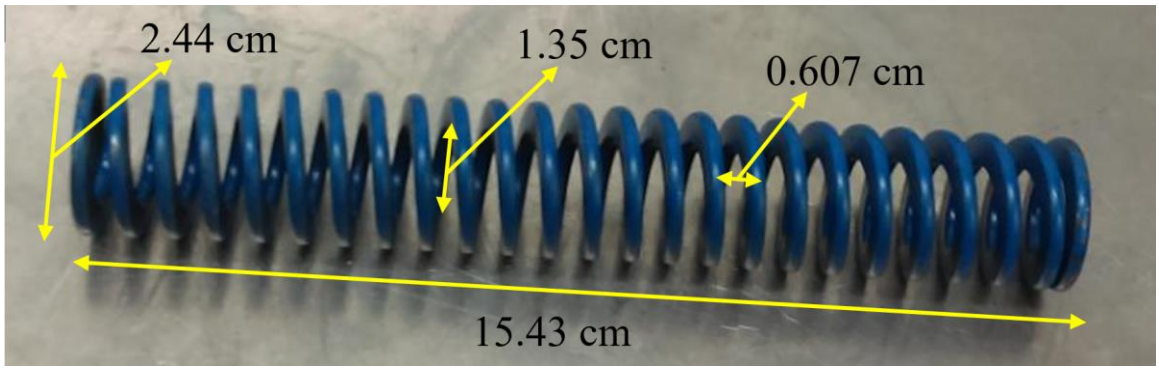

Figure 3.2 Shchelkin spiral used in PDE tube for promoting DDT.

A gas cart for injecting fuel, oxidizer, and purge air was assembled for the PDE. Figure 3.3a shows a schematic of the gas cart items assembly that is triplicated for hydrogen, oxygen, and air, while Figure 3.3b shows the final assembled gas cart attached to the mobile PDE-LPG system. Hydrogen and oxygen are supplied to the gas cart from regulated cylindrical tanks, while purge air is supplied from an air compressor. The gas cart incorporates several components including Hoke pneumatic valves (0722A4), SuperFlash flashback arrestors (ISO 5175 EN730), Flow-Dyne critical flow nozzles (N120076-SA), Omega pressure transducers (PX302-1kGV), and temperature thermocouple sensors (P09C410J4HA) to ensure safe operation of the PDE and for the measurement of gas flow rates into the engine. The pneumatic valves are controlled by high-pressure air supplied through a Dayton solenoid valve (6X542). The flashback arrestors are a safety feature of the facility to prevent any potential combustion wave from travelling back through the lines to the fuel and oxidizer gas supply tanks. The critical flow

nozzles in conjunction with the gas pressure and temperature measurements are used to determine the mass flow rates into the PDE tube.

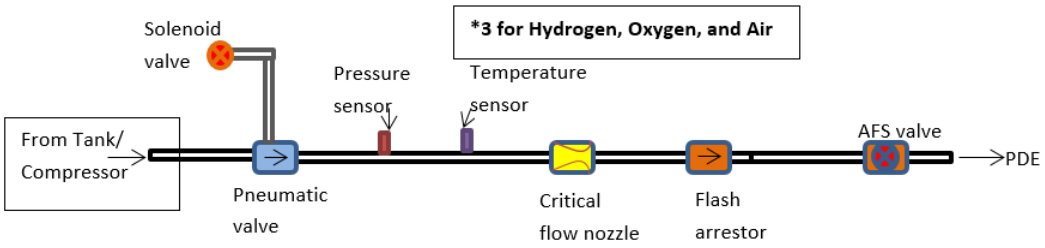

(a) Schematic.

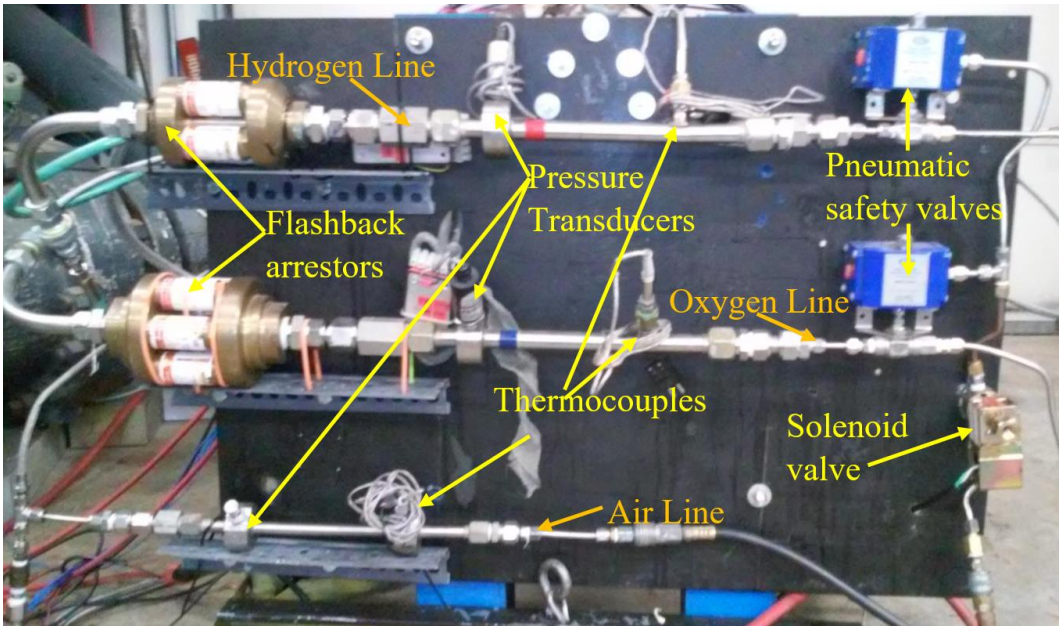

(b) Photograph.

Figure 3.3 PDE gas cart assembly.

A diverging nozzle is placed at the end of the PDE to expand the exhaust to atmospheric pressure. The conversion of the enthalpy to kinetic energy allows for a greater transfer of momentum to the piston. The total pressure of the gas is the constraining property needed for proper nozzle design. The total temperature of the PDE exhaust flow

is a high constant value and decrease of the static temperature occurs at a much slower rate due to expansion relative to the static pressure. The total pressure can be computed from the static pressure and the wave velocity using

$$p_0 = p_s + \frac{1}{2}\rho u^2 \tag{3.1}$$

A theoretical approach based on CEA calculations and an experimental approach based on a fully-filled PDE operation were considered for the determination of the total pressure to be expanded by the nozzle.

From a 1 Hz run of a 1 in. diameter PDE, the static pressure and wave velocity were measured to be $p_{det} = 250$ psia and $u_{det} = 2{,}260$ m/s, while from CEA calculations these values are $p_{det} = 274$ psia and $u_{det} = 2{,}835$ m/s [49]. The area ratio of the nozzle was calculated from isentropic relations, using the specific heat ratio of the exhaust gases $\gamma_{exh.} = 1.13$, the static to total pressure ratio of the detonation exhaust, and the total pressure to the ambient pressure ratio p_{0det}/p_{amb}. The area ratio for the nozzle using the experimental data is A/A^*=8.43, while for the theoretical case the area ratio is A/A^*=8.62. Proceeding with the experimental result, and with a nozzle that slightly underexpands the gas, the diameter ratio of D_2/D^*=2.85 was chosen, yielding an area ratio A/A^*=8.12. A 10° semi-angle for the diverging section is proposed which results in a nozzle length of 5.25 in. as shown in preliminary design in Figure 3.4.

Based on this preliminary design, a technical drawing of the diverging nozzle is made, as shown in Figure 3.5. This design includes two 1.25 in. thick flanges at the throat and exit of the nozzle. These flanges are made sufficiently thick to allow for mounting ports of water cooled pressure transducers.

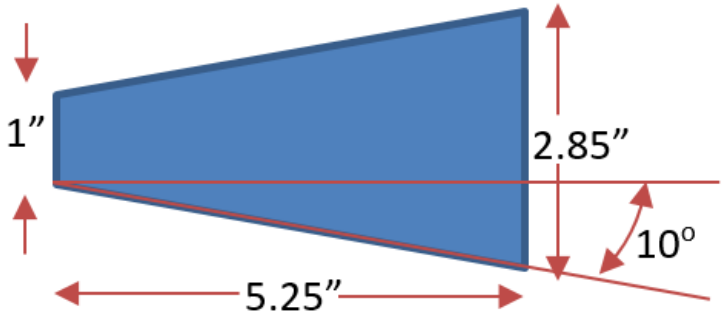

Figure 3.4 Preliminary design of diverging nozzle.

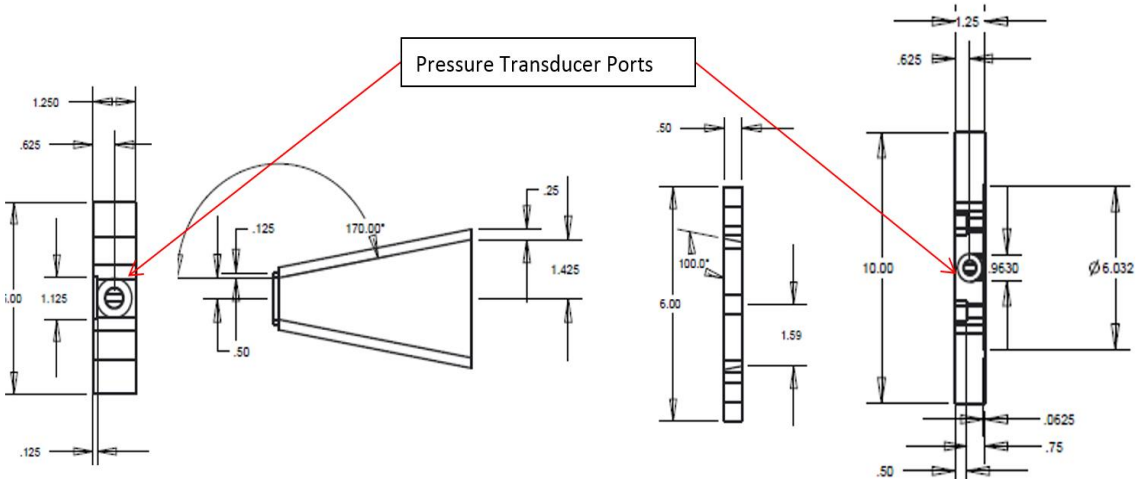

Figure 3.5 Technical drawing of diverging nozzle.

The nozzle throat, nozzle diverging section and exit plate are all welded together as shown in Figure 3.5, while the 10 in. diameter exit nozzle flange is machined separately in order to reduce cost. The 10 in. diameter exit nozzle flange is attached to the welded nozzle section with alignment pins on the nozzle exit plate. The nozzle pressure ports allows for the determination of the performance of the nozzle by taking the pressure ratio between these locations. A picture of the machined nozzle is shown in Figure 3.6.

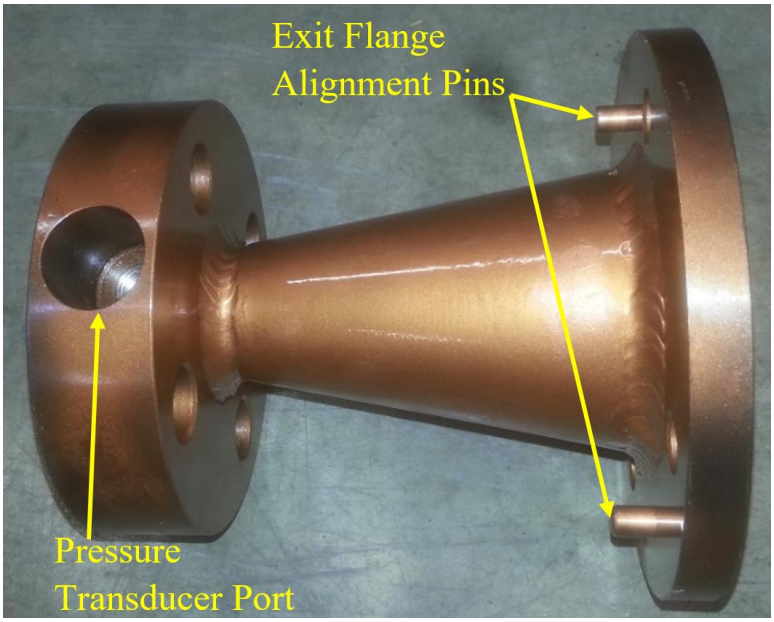

Figure 3.6 Picture of diverging nozzle.

The proposed piston design is an open, cylindrically U-shaped piston that allows the flow to stagnate, prevents cross flow upon impact, and also acts as an exhaust valve for the entire system. This proposed design allows the LPG structural dynamics to be considered independently from the PDE system. The piston is designed to support three pressure measuring ports. The center port is also adapated to rigidly connect the LPG slider for the power generation configuration.

The piston design process incorporated the air gap between the 10 in. nozzle exit flange and the piston cylindrical section. Therefore, a nominal 10 in. SCH 40 pipe, 10.02 in. ID and 10.75 in. OD is chosen for the tubular section of the cylinder. This resulted in an air gap between the nozzle flange and piston of only 0.01 in. in the radial direction, and an area gap of only 0.3145in.^{2}, which is about half the 1 in.-ID PDE exit area of 0.785in^2.

Also considered in the piston design is the expansion of the gas because the motion of the piston away from the PDE will create a vacuum. From cycle analysis discussed in

Chapter 2, a volume expansion factor of 8 is typically required to return the gas to ambient pressure. Previous efforts to develop a PDE-LPG system by Braun et al. did not attempt to expand the gas to atmospheric, but focused on only utilizing the blast wave momentum [11]. The total expansion ratio is 9 with the inclusion of the PDE volume. From the above consideration, only a 2 in. long tube is thus needed for the piston

$$L_{Piston} = 8L_{PDE}\left(\frac{D_{PDE}}{D_{Piston}}\right)^2 = 8 \times 26 \times \left(\frac{1}{10.02}\right)^2 = 2.07 \text{ in.} \tag{3.2}$$

The piston length was doubled to 4 in. for safe measure. The technical drawing and picture of the piston are shown in Figure 3.7 and 3.8.

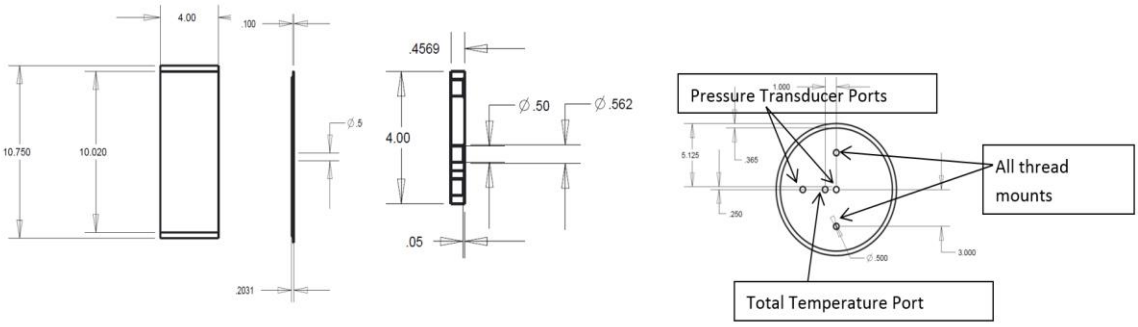

Figure 3.7 Technical drawing of piston.

Other system components include the solenoid valves, piston springs, and linear power generator. The solenoid valves are AFS gaseous fuel injectors with high mass flow rate discussed in section 3.1.2. The piston springs are made of piano wire, 11.25 in. long and discussed later in section 3.2.1. The linear power generator is adapted from a linear motor from LinMot Inc, and consists of magnetic slider and stator. The detailed properties of this unit are discussed later in section 3.2.2.

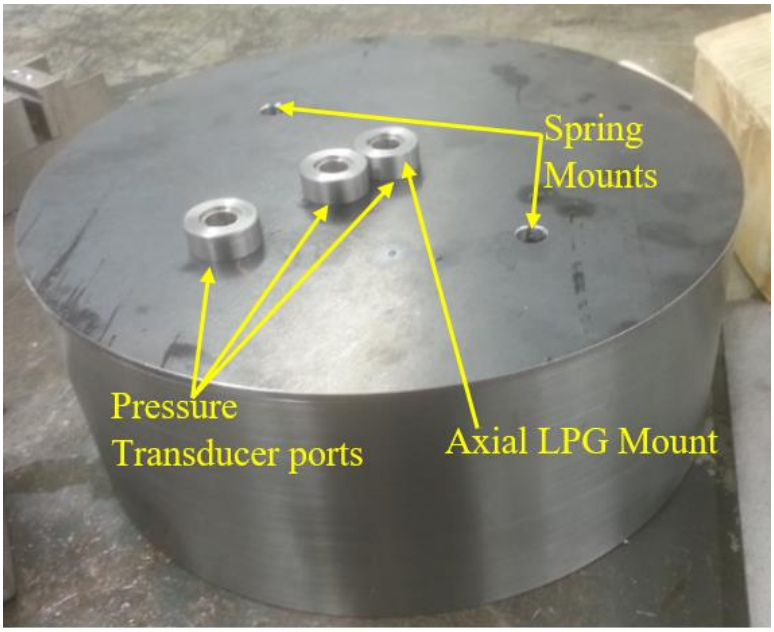

Figure 3.8 Picture of piston.

3.1.2 Operation and Data Acquisition

The PDE is operated with stoichiometric oxyhydrogen mixture for all tests. The fill-fraction is the primary parameter varied between operations in order to study the effect of using less fuel to improve the overall system efficiency. The pulsed nature of the engine is created by intermittently injecting fuel and oxidizer through valves and igniting the mixture in a detonation tube. Therefore, the precise sequential timing of these devices is critical for reliable operation. The PDE has five major phases in a cycle of operation as shown in Figure 3.9.

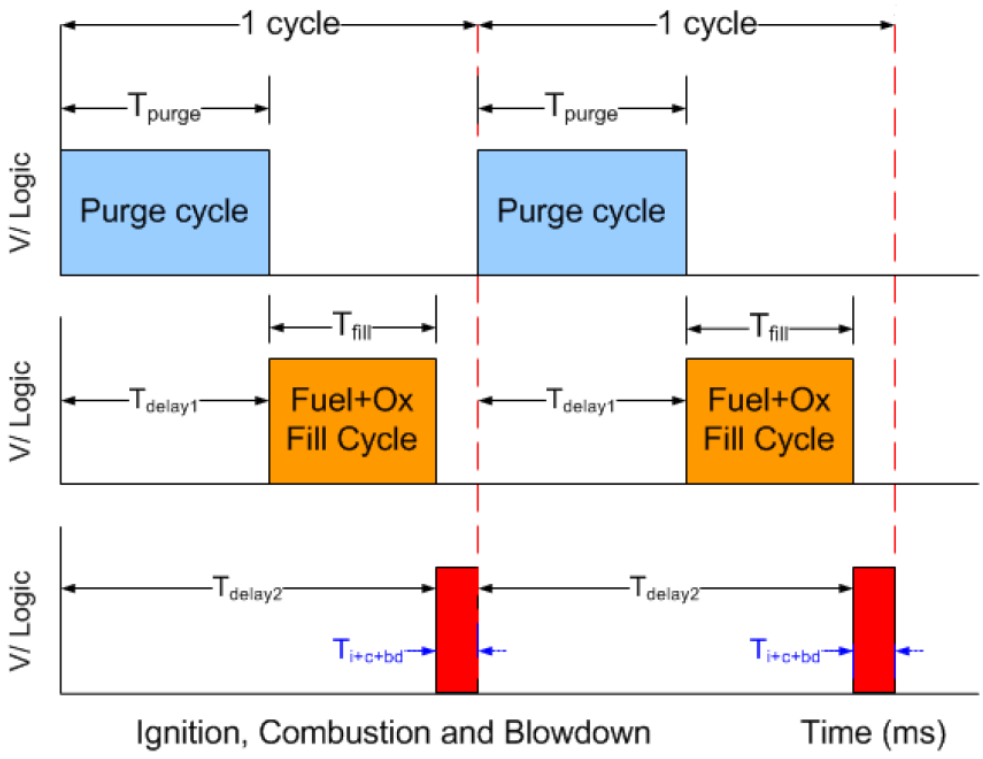

Figure 3.9 Phases of PDE operation [30].

These include the purge phase, followed by the fuel-oxidizer injection phase, ignition phase, combustion phase, and blowdown phase. The purge phase is then repeated marking the beginning of a new cycle. During the purge phase, a cool gas such as air is injected into the detonation tube in order to act as a buffer between the hot burned gas from the blowdown phase and the fresh detonable mixture from the next fuel injection phase. A major effect of the purge gas is cooling the internal walls of the detonation tube. The cooling prevents the detonable mixture from auto-ignition.

The start and duration of the purge, fuel injection, and ignition phases are directly controlled by precise timings of valve openings and ignition firing, while the combustion and blowdown phase are subject to the fuel and oxidizer mixture and the pressure boundary conditions at the tube exit. The timing of the phases is achieved by sending TTL signals

from NI's LabView® program. All of the phases are run on the same time base from a master signal in order to assure synchronicity. The TTL signal for the purge phase is the master signal with no time delay, while the fuel injection and ignition signals are triggered by the purge signal and are delayed. This allows for the purge to be run independently of the other phases in order to cool down the tube, and also to ensure safety since no firing will occur without being preceded by a purge phase. The front panels of the LabView® virtual instrument shown in Figure 3.10 is used to input the physical channels of the signals, the PDE frequency of operation, duty cycle, initial time delays, and trigger source from the master signal. This program also allows for the conditions of operation to be changed from one state to another in the same operation. For example, the first 5 detonation pulses could be operated with one set of delays and duty cycle while the next 10 detonation pulses can be operated with a different set. This jump in operating conditions can be used for driving the piston displacement response to operate at resonance.

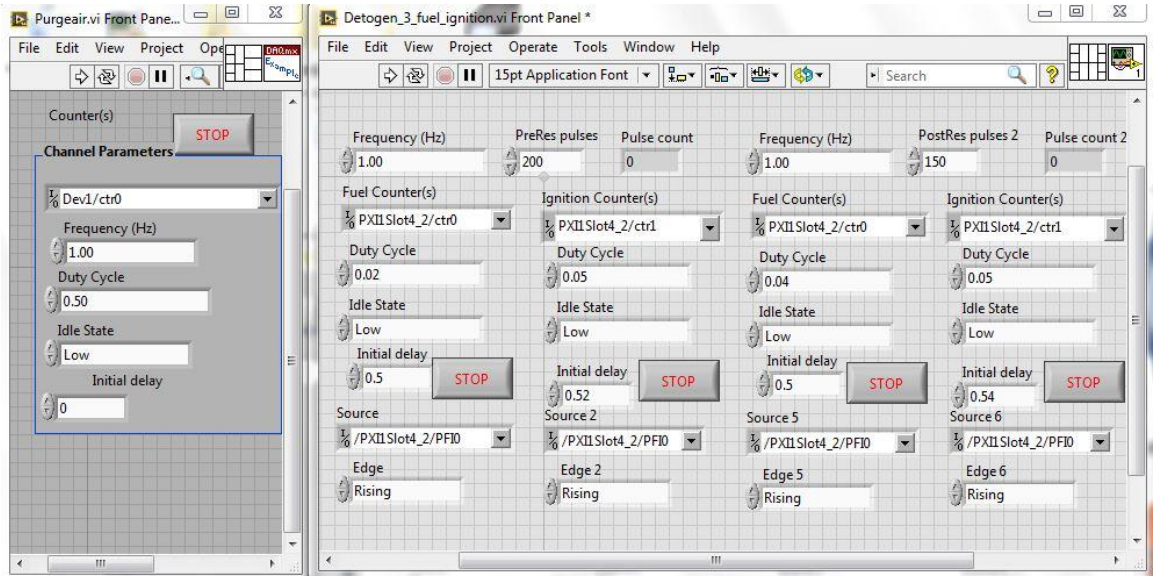

Figure 3.10 Front panel of LabView® VIs used to control PDE operation.

The TTL signals required for the pulsed operation of the PDE are generated by a control system shown in Figure 3.11 that includes a computer loaded with NI's LabView® program and a fiber optic output card (NI PCI 6221), an NI power supply box (NI PXI 1042Q) that holds fiber optic input card (NI PXI-8336), and two analog outputs cards (NI PXI-6722 8 ch AO), and a BNC-2110 and a BNC 2120 module.

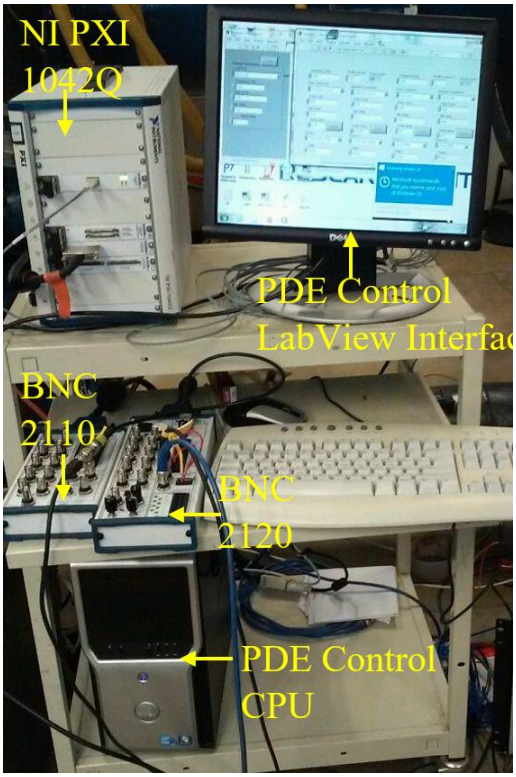

Figure 3.11 Control system for PDE operation.

The LabView® program is able to recognize the physical channels on the BNC modules through cable connections with the analog output cards, and the fiber optic connection with the computer. The counter output analog channels on the BNC modules are required for the transmission of a pulsed TTL signal. Each BNC module has only two counter output channels; therefore, at least two BNC modules are required to transmit the TTL signals required for the purge valves, fuel valves, and igniter. A 5 VDC TTL digital

signal is generated by the LabView® program and transmitted to the analog output cards which convert the digital signal to an analog signal. This analog signal is transmitted to the BNC modules. The analog output for the purge valves is split on the BNC module, in order to serve as a trigger source for the fuel-oxidizer injection and ignition phases. The use of the purge valve signal as the trigger source, ensures that all the TTL control signals share the same time base.

The combustion phase is initiated by the ignition phase; however, the duration of the combustion is dependent on the fraction of the detonation tube filled with a combustible mixture. This fraction is referred to as the fill fraction, and is dependent on the regulated back pressure of the fuel and oxidizer, and the duty cycle of the TTL signal for the fill phase. The duty cycle of a TTL signal is the percentage of time within a cycle that the 5VDC TTL signal is on. This percentage represents the amount of time that the purge valves and fuel-oxidizer valves are open. It also marks the incident of the ignition spark. Table 3.1 shows the resultant engine fill fraction for stoichiometric operation of the PDE at various frequencies, fuel and oxidizer back pressures, and corresponding delays and duty cycles for purge, fuel-oxidizer, and ignition phases.

Table 3.1: Sample timing selections for PDE operation

Frequency [Hz]	H_2 [Psig]	O_2 [Psig]	Fill-Fraction	Purge		Fuel-Oxidizer		Ignition	
				Delay [s]	Duty Cycle	Delay [s]	Duty Cycle	Delay [s]	Duty Cycle
1	15	59	53%	0	75%	0.75	2%	0.77	5%
1	15	59	80%	0	75%	0.75	3%	0.73	5%
1	15	59	133%	0	75%	0.75	5%	0.8	5%

10	25	84	14%	0	75%	0.075	4%	0.081	8%
10	25	84	28.8%	0	75%	0.075	8%	0.083	8%

The solenoid valves used for the purge air injection and fuel-oxidizer injection are gaseous fuel injectors manufactured by AFS Global (Gs60-05-5-C). These valves have 2-3 times higher mass flow rate compared to other automotive gas injectors, and are compatible with various gaseous hydrocarbons and hydrogen [50]. The corresponding discharge coefficients for air, hydrogen, and oxygen for AFS valves have been previously experimentally determined [51]. The dimensions and a photograph of the AFS valves are shown in Figure 3.12.

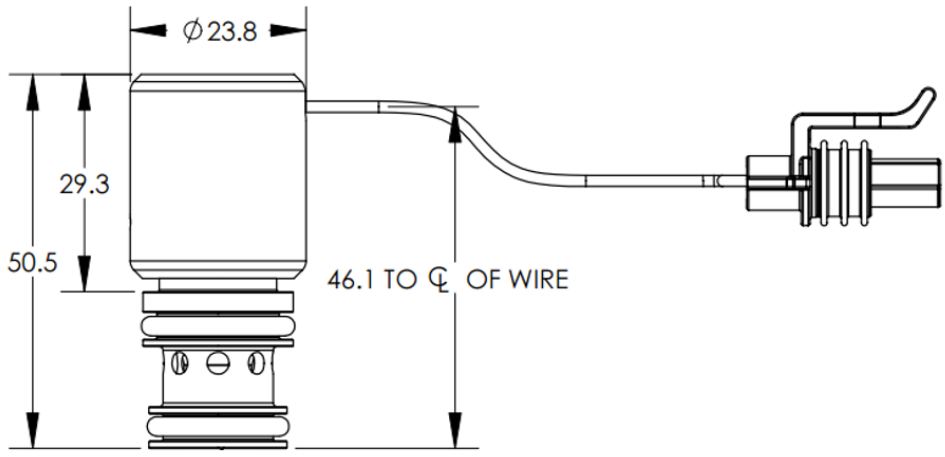

(a) Drawing [50]

(b) Photograph

Figure 3.12 AFS Gs series gaseous fuel injector.

The AFS injectors are operated with control modules that require 12 VDC at an 8 A peak current for opening and a 2 A hold current. In order to provide the power requirements of the injectors, a pair of current buffer amplifiers were built to interface the 5 VDC TTL control signal from the LabView® program with the AFS control modules, and an external power source capable of supplying 12 VDC. A schematic and a photograph of the interfacing circuit for the current buffer amplifiers are shown in Figure 3.13. The current from the external power source is amplified by a current power buffer (LT®1010) manufactured by Linear Technology. The LT®1010 current buffer amplifier is a fast, unit gain buffer that can increase output capacity by more than an order of magnitude while reducing sensitivity to capacitive loading and thermal feedback [52]. The speed of the current buffer is improved in the circuit with a single 5 kΩ external resistor connected to the input signal.

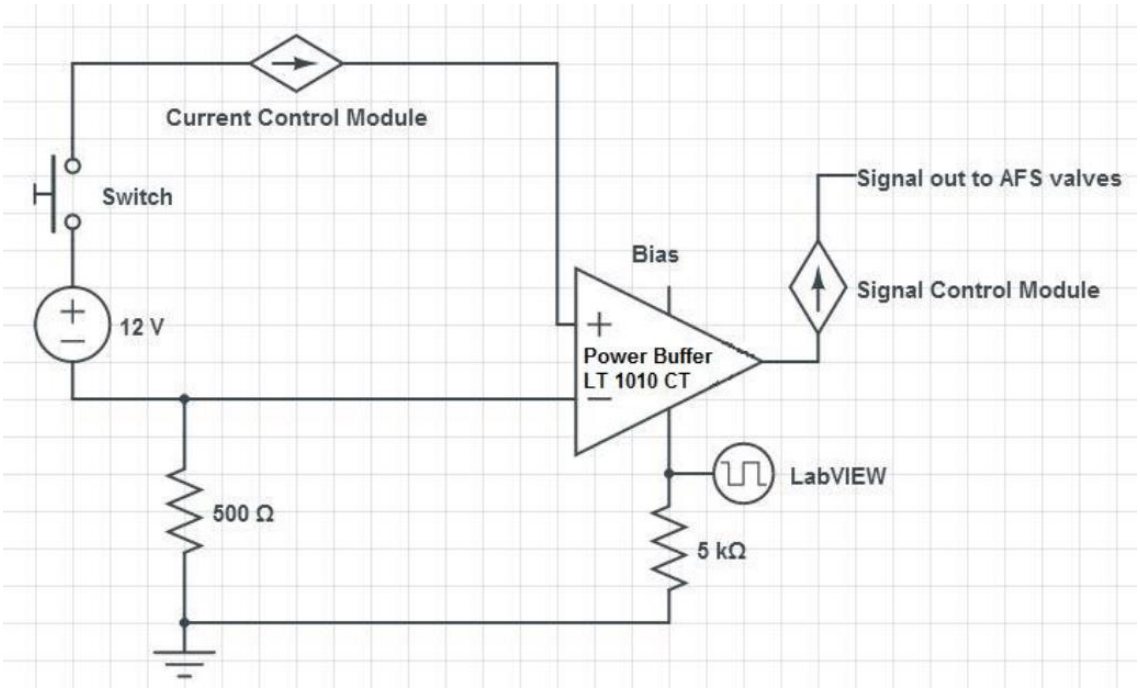

(a) Schematic [51]

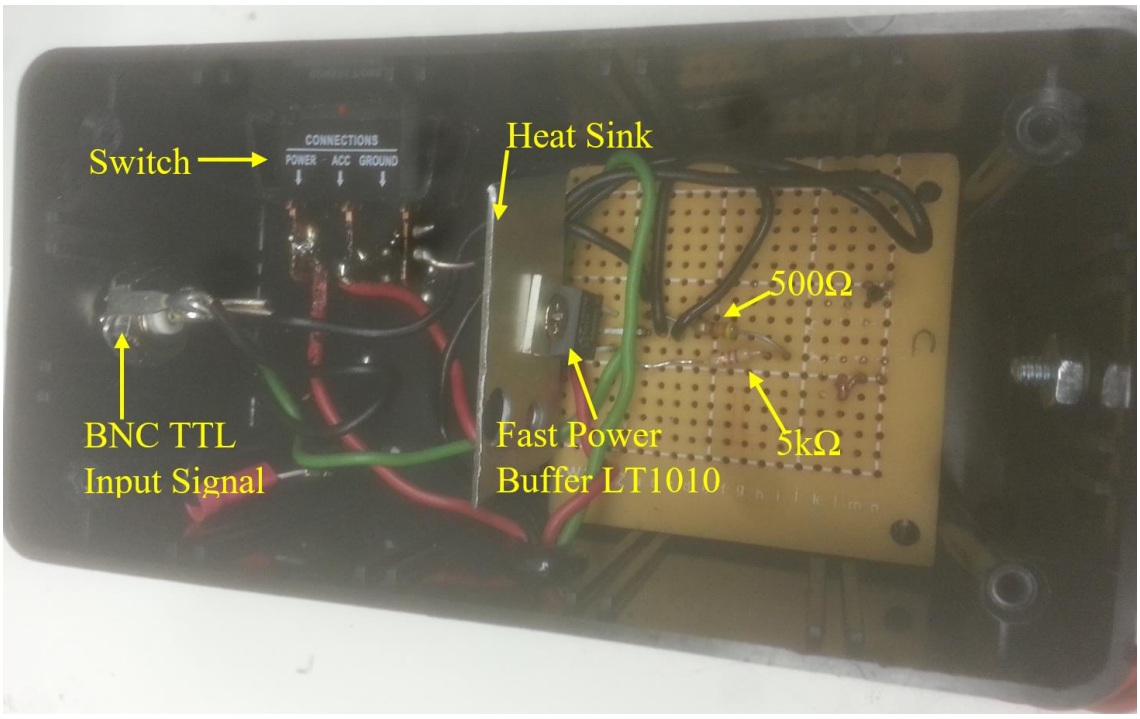

(b) Photograph

Figure 3.13 Buffer current amplifier circuit.

The switch in the circuit is used to turn on the external 12 VDC power to be amplified for the AFS injector operation. A heat sink is attached to the current buffer amplifier in order to help reduce the heat loads during high-frequency operation where the cumulative duration at peak current is significantly increased. In Figure 3.13b, the green wires are used for the TTL signal, the red wires are for power, and the black wires are for ground. The amplified current from the current buffer is connected to the AFS control modules. The pair of buffer amplifier boxes and AFS control modules used to control the AFS injectors for the purge air valves, and fuel-oxidizer valves are shown in Figure 3.14.

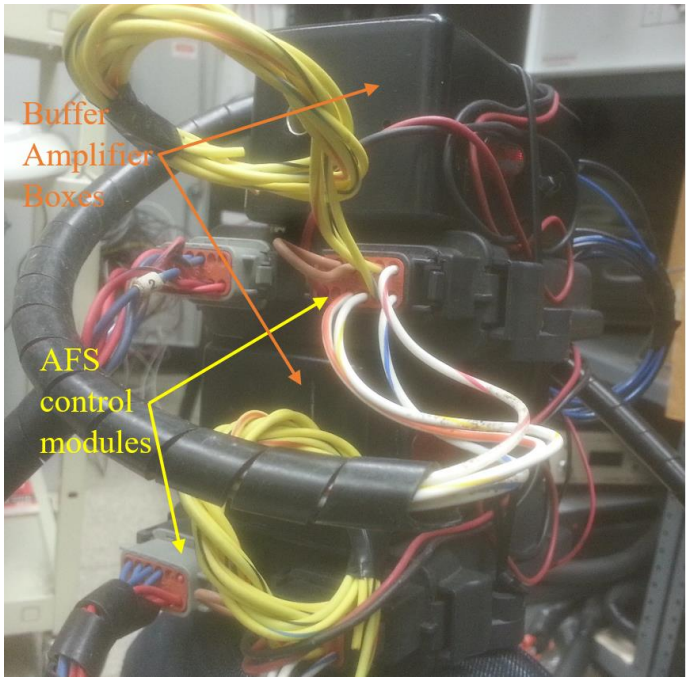

Figure 3.14 Pair of current buffer amplifier boxes and AFS injector control modules.

A total of 8 PCB 111A24 piezoelectric pressure transducers are used in this study, four are mounted on the PDE, a pair are mounted on the nozzle throat and exit, and another pair are mounted on the piston face. These pressure transducers measure the conditions in

the PDE-LPG system during operation. The position of the mounted PCB transducers away from the PDE thrust wall is listed in Table 3.2. Using the time-of-flight method, wave propagation speeds can be deduced from the pressure outputs, and the distances between pressure transducers. These pressure profiles can also verify the presence of detonation combustion within the PDE.

Table 3.2: Position of PCB transducer relative to distance from the PDE thrust wall.

PCB Transducer	**PCB2**	**PCB3**	**PCB4**	**PCB5**	**Noz-T**	**Noz-E**	**Pis-1**	**Pis-2**
Position (in)	11.5	15.5	19.5	23.5	26.75	33.00	36	36

The output from the pressure transducers on the PDE and piston are sent to a PCB model 483A signal conditioner. The output voltages of the PCB pressure transducers, Penny+Giles LVDT, LinMot® LPG-voltage, and LPG-current are read by National Instruments TB-2709 data acquisition cards (NI-DAQs), and stored by a National Instruments PXIe-8130 embedded controller. The storage of all the data from the various components in the same file is critical for proper quantitative analysis, due to the transient nature of the PDE-LPG system. Each DAQ card has 8 input channels, and by using 2 NI-DAQ cards, a maximum of 15 channels were available in this study. The DAQ is triggered manually during PDE operation. The DAQ is programmed via National Instruments LabVIEW software, to record data for 3 seconds, and at a simultaneous sampling rate of 250 kHz/channel, for all channels.

3.2 Determination of Essential Parameters

3.2.1 Spring Constant Test

A pair of 11.25 in. piano compression springs shown in Figure 3.15 is used to simply support the piston of the PDE-LPG system. A testing rig shown in Figure 3.16 was assembled to determine the spring constant of these springs. This system operated by applying tension to the compression spring by separating two wooden plates.

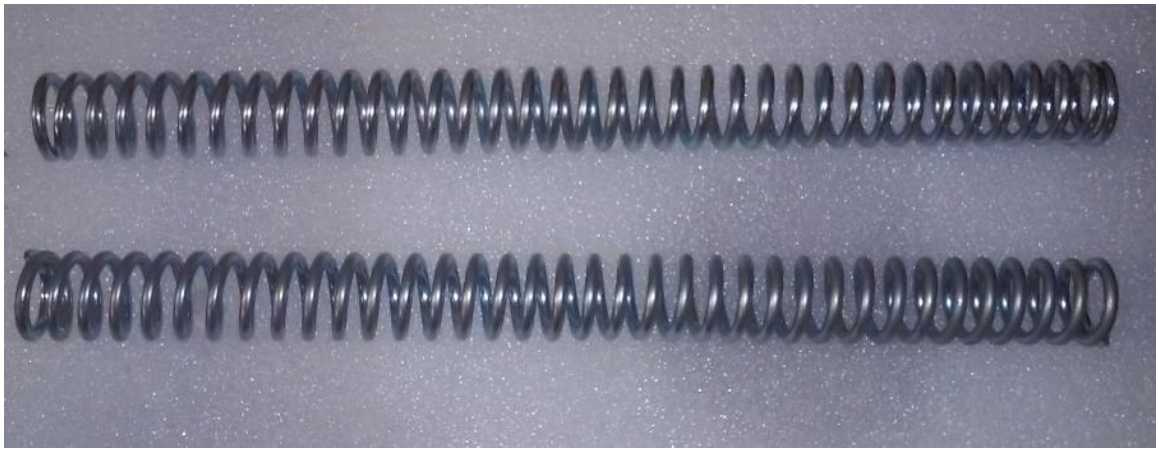

Figure 3.15 Pair of 11. 25 inch springs used for PDE-LPG system

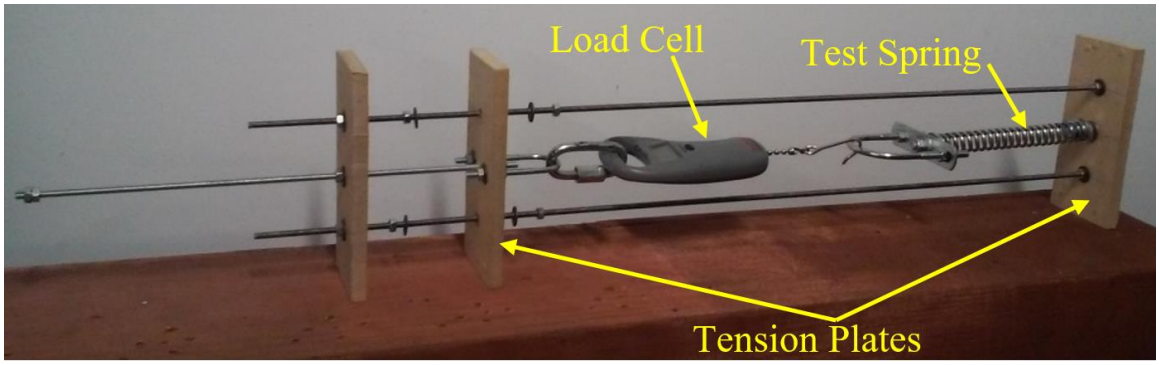

Figure 3.16 Spring constant measurement rig.

A load cell is placed between the wooden tensioned plates in order to measure the tension. As the tensioned plates are separated, both the distance between the plates and the force displayed by the gauge are recorded. The results of this test are shown in Figure 3.17.

The fitted trend-line equation is $\vec{F} = 1.1845\Delta x$ with $R^2 = 1$, and the slope of this linear fit is the spring constant.

The spring constant value is 1.1845 lbf/mm or 30.09 lbf/in. Since the pair of springs have similar spring constants and are attached in parallel to the piston back, the effective spring constant of the PDE-LPG SDOF system is 60.18 lbf/in. The spring constant value serves a baseline and was chosen to maximize the velocity of the slider, so the system oscillations are dampened by the energy transfer to the LPG stator.

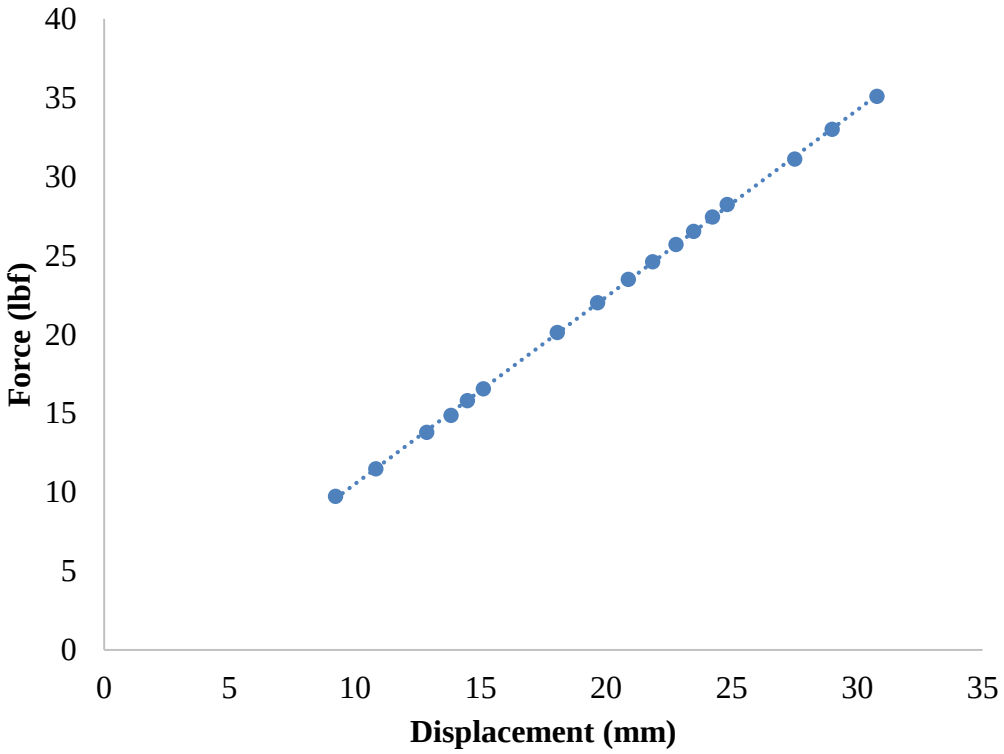

Figure 3.17: Spring constant measurement for 11.25 inch spring.

3.2.2 Linear Power Generator Calibration

The linear power generator (LPG) used in the PDE-LPG system is adapted from a linear motor comprised of a slider and stator (P01-23x160/70x210) manufactured by

LinMot®. This assembly is shown in Figure 3.18. The LPG magnetic slider has fine thread tapped mounts on each end for driving by a motor during calibration, and the prime mover piston in the PDE-LPG operation. The stator is filled with wound solenoid wire in a two-phase configuration. The induced voltage can be measured from the stator power cable. It is critical that the LPG slider be properly aligned axially with the center of the driving mechanism in order to prevent warpage of the slider from the resultant jerk loads due to misalignment.

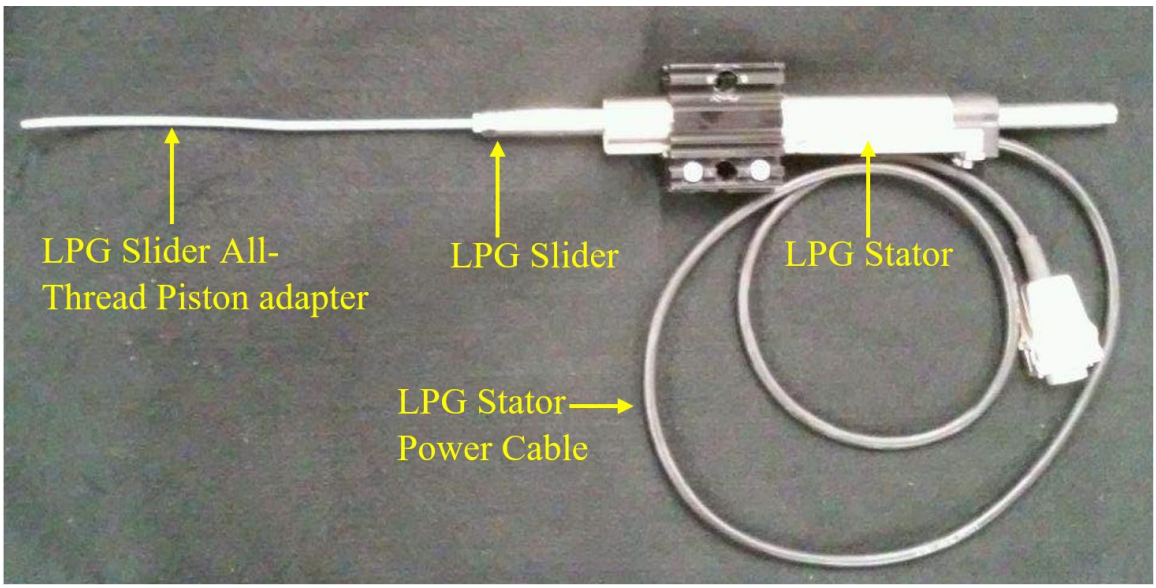

Figure 3.18 LinMot® linear motor and slider.

The apparent power range of the LinMot® 2-Phase LPG is initially determined by measuring the maximum current and maximum voltage through manually oscillating the slider. The maximum apparent power from each phase was approximately 4 W, and 5.1 W after changing the configuration from a unipolar generator to bipolar generator. The PDE-LPG is designed for a maximum stroke of 4 in. The induced voltage is also linearly dependent on the velocity and the magnetic field strength.

An estimate of the maximum theoretical power from detonating an oxy-hydrogen mixture in the fully-filled PDE at 5 Hz is 5.8 kW. Hence the LPG extracts power at three orders of magnitude less than what the PDE can generate! Detonating H_2-air reduces this *theoretical* maximum power by half.

As shown in Figure 3.19, in the Standard Stroke (SS) range, the LPG has a constant maximum force, since the drive magnets of the slider are in the active range of the stator. This results in optimal power generation over the entire SS stroke range. The further the slider moves out of the SS stroke range, the fewer the number of magnets that are within the active part of the stator, thereby generating less power.

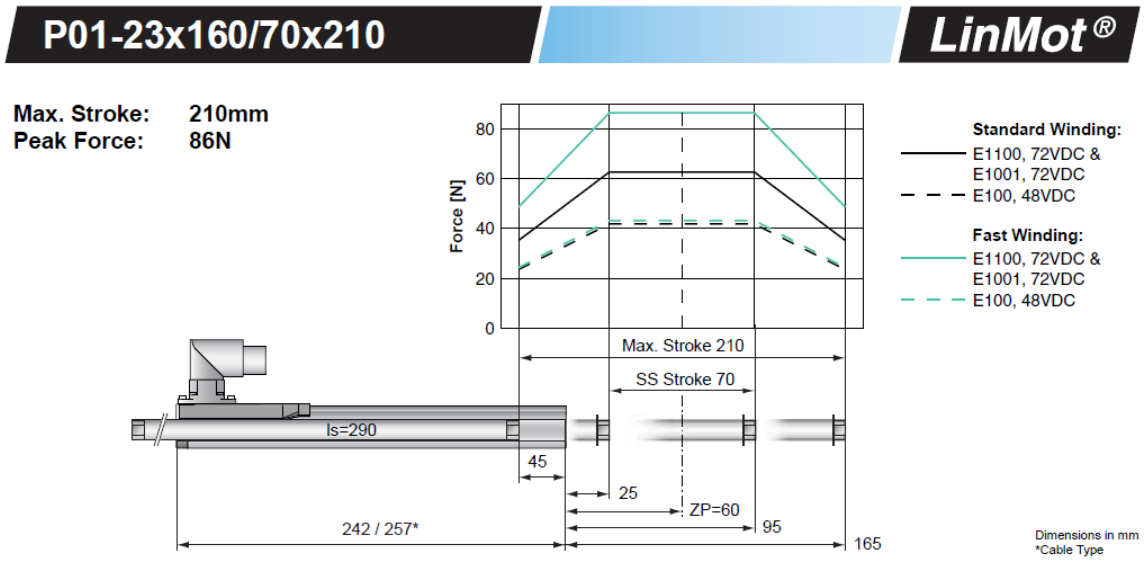

Figure 3.19 LinMot® linear motor stroke force diagram [53].

A calibration rig consisting of an NI motion controller (NI PXI-7340), a 60 VDC stepper motor, and a crankshaft mechanism, is built to independently examine the performance of the LPG. Using the stepper motor to drive the LPG as shown in Figure 3.20, and based on a design stroke of 4 in., the aforementioned mismatch of PDE power

output and LPG electrical power output, the LPG is calibrated for a maximum rated velocity of 10 Hz or 600 RPM. Hence the LPG is calibrated from 1–6 W of electrical power without regard to the losses due to thermal stress and magnetic reluctance. Performance plots of the LPG based on the current, voltage and power at constant motor speeds are shown in Figures 3.21–3.23.

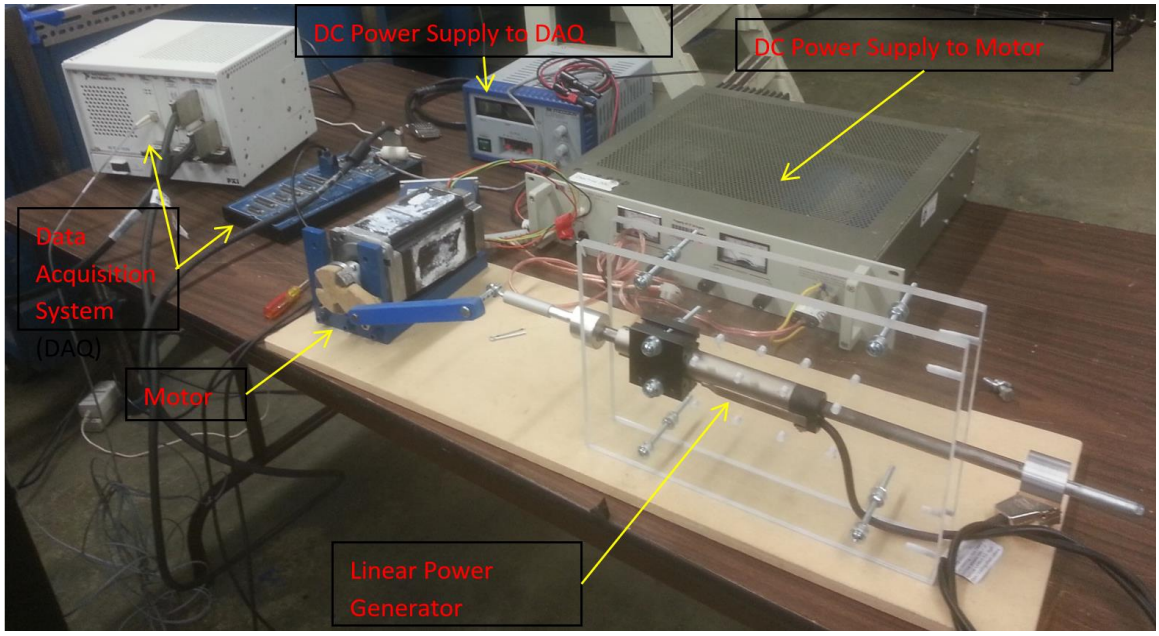

Figure 3.20 Linear motor calibration rig.

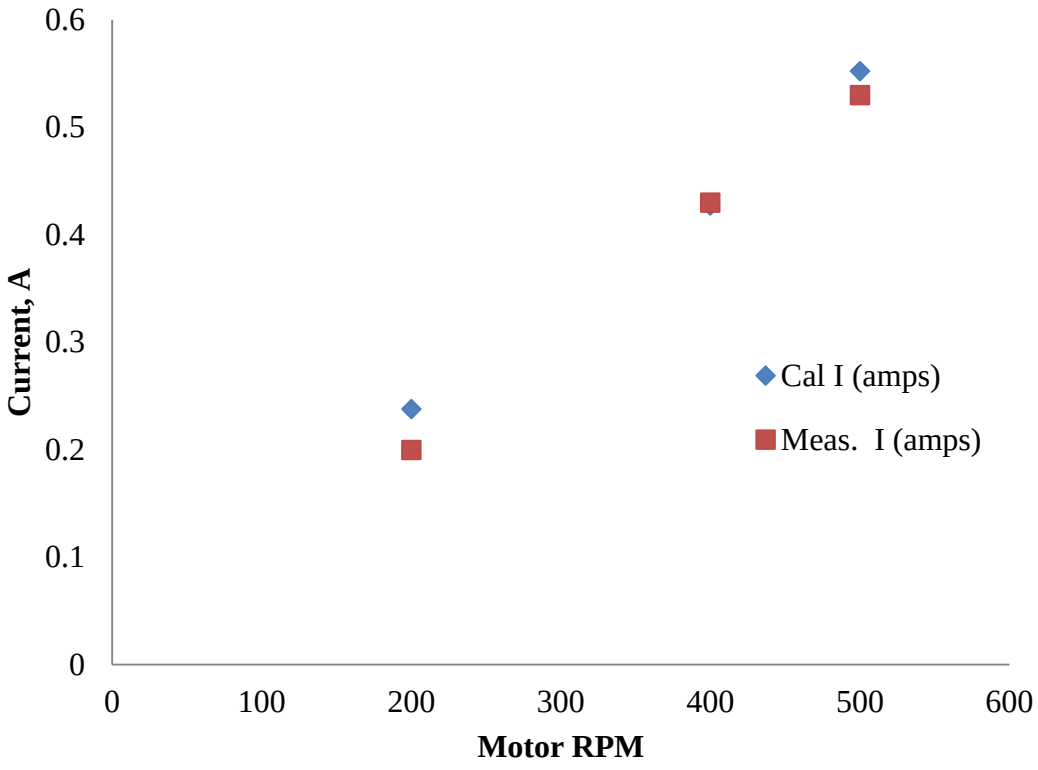

Figure 3.21 Peak current measurement for LPG.

The results shown confirm the linear power generation circuit. Ohm's law is used to compute the expected current based on the previously measured voltage. This corresponded to directly measured values of current. Detailed LPG calibration is completed with a maximum motor speed of 700 RPM. The PDE-LPG piston resonator system is designed to operate in this frequency range. The gross mismatch of PDE and LPG power will be unforgiving for efficiency calculations. However, the efficiency of this component in the overall system is evaluated relative to this calibration in Chapter 4.

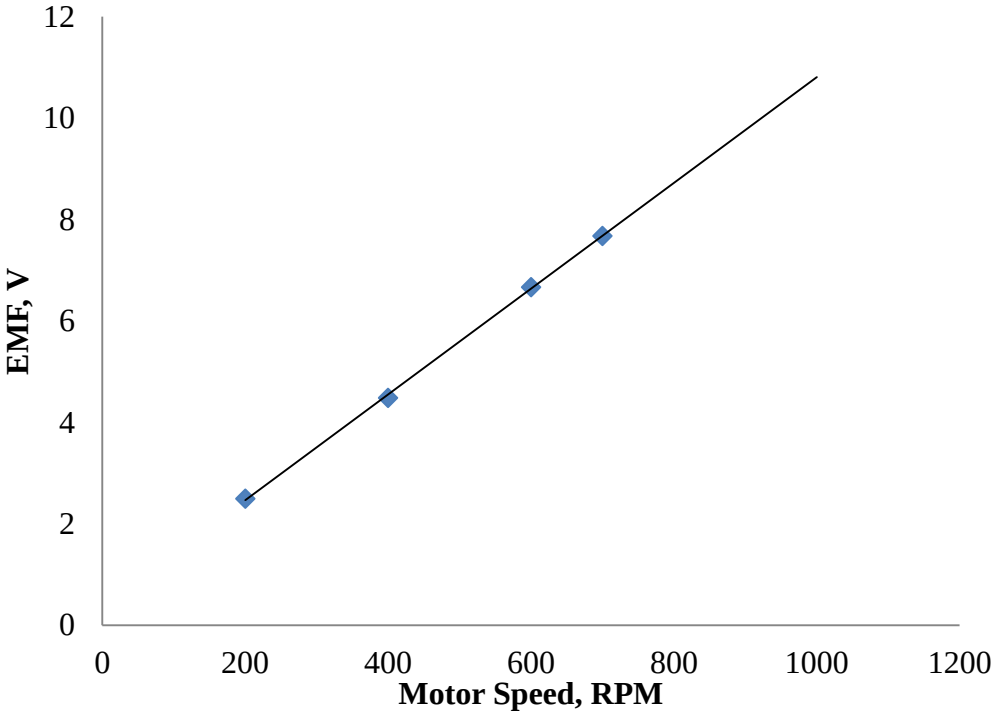

Figure 3.22 Peak voltage measurements for LPG.

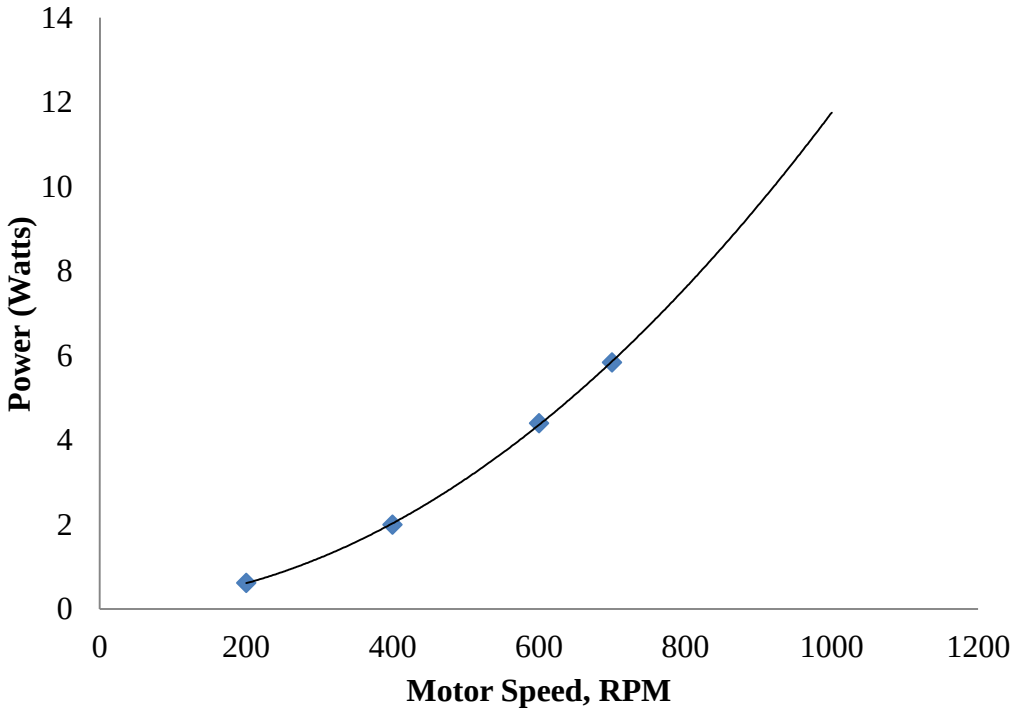

Figure 3.23 Peak power measurements for LPG.

CHAPTER 4

Results and Discussion

The energy and exergy efficiencies of the PDE-LPG subsystems and overall system are analyzed using the general approach discussed in Chapter 2. This chapter presents the experimental results of each subsystem followed by the derived performance of the PDE-LPG facility. The static pressure profiles along the PDE and nozzle are presented. The specific impulse and the sound levels are used to compare the results of the facility operation in configurations 1 and 2 described in Chapter 3.

The energy and exergy of the fuel are calculated from the LHV and the chemical exergy quality factor. The stagnation pressure profiles on the piston face are measured and are used to derive the PDE pressure work on the piston. The spring work is calculated from the displacement of the piston. The current and the voltage are simultaneously measured, and the average power per pulse is calculated based on the duration of the piston motion. The average electrical power is used to calculate the electrical energy output per pulse of the system. These energy and exergy values of the various systems are then used to compute the sub-component efficiencies. The experimental results are presented for varying tube fill-fraction ranging from 10.7 to 240%, and electrical loads ranging from 46.7 to 505 Ω.

4.1 Experimental Results

4.1.1 PDE Pressure Profiles

This section details the static pressure profiles along the detonation tube. Pressure measurements using piezoelectric transducers along the detonation tube are used to determine the onset of detonation, and also to calculate the detonation wave velocity within

the tube. The piezoelectric pressure transducers record zero voltage under exposure to long steady pressures such as the ambient atmospheric pressure initially within the tube. All the pressure profiles presented in this section are corrected to reflect the absolute pressure by accounting for the ambient pressure present within the tube. In configuration 1 shown in the experimental setup of Chapter 3, only the PDE is setup on the mobile stand. In this configuration, only the pressure profiles along the PDE and the force at the thrust wall are measured.

The pressure profile of a single detonation wave for a flush-mounted pressure transducer at 11.5 in. from the thrust wall for a fully-filled operation is shown in Figure 4.1. This pressure profile is similar to the theoretical pressure profile predicted for the thrust wall of a fully-filled PDE shown in Chapter 2, although the pressure sensor is at a location equivalent to 44% tube fill-fraction away from the thrust wall.

The tube is initially filled with a detonable mixture at 0.101 MPa (or 1 atm). The incidence of the detonation wave is recorded at 0.59775 s, with a peak pressure of 2.266 MPa. This peak pressure is higher than the pressure of 1.8 MPa predicted by CJ theory for stoichiometric oxyhydrogen mixture, but lower than the 4.0 MPa predicted for the ZND point of a detonation wave. The ZND pressure is not resolved due to the low sampling rate of the data relative to the velocity and thickness of the shockwave, and the inadequate spatial resolution of the pressure sensor. The pressure spike due to the detonation wave is then followed by a plateau of relatively steady pressure at 0.6 MPa. This pressure plateau is due to the expansion of the burned gases matching the boundary condition at the thrust wall of zero flow velocity. The pressure plateau at this tube location on the tube lasts for 0.4 ms.

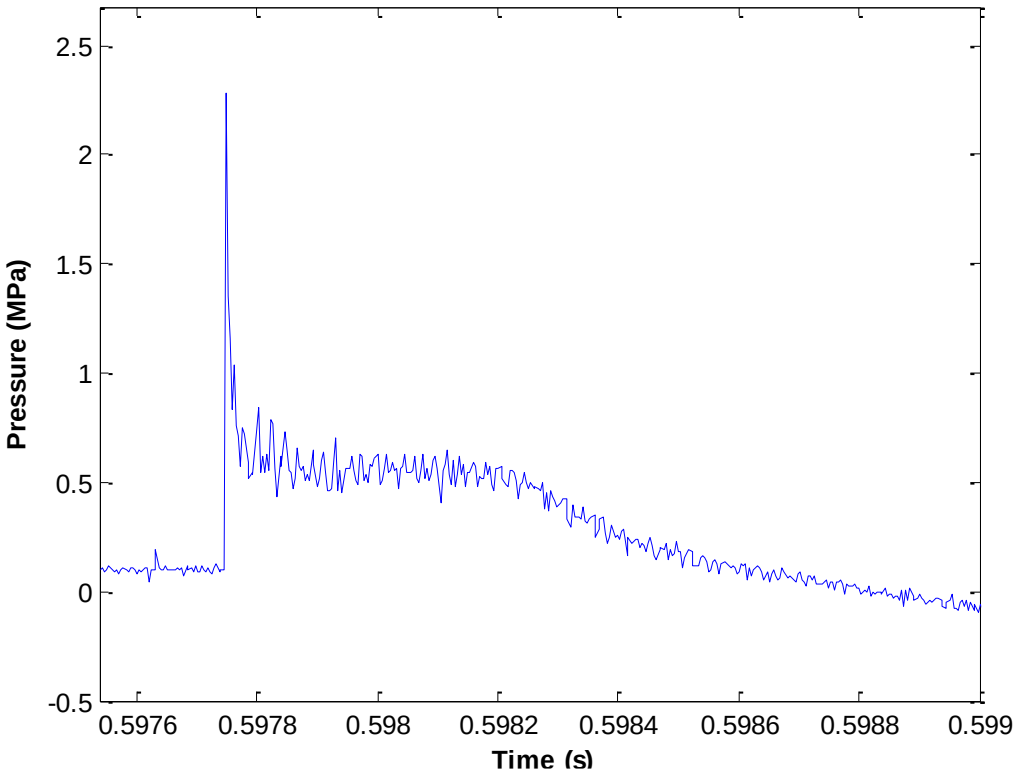

Figure 4.1 PDE pressure profile of a single detonation.

The plateau pressure then begins to decrease once expansion waves travelling from the exit plane of the detonation tube reaches this transducer location, reducing the pressure in the detonation tube to below ambient pressure due to the gas momentum of the exhaust gases and the boundary condition at the thrust wall. The pressure continues to decrease and becomes negative which is an unphysical measurement of pressure. This artefact is due to the characteristics of the piezoelectric sensor under rapid expansion and high thermal loads.

The range of the pressure measurements used for further analysis is the overpressure duration, which corresponded to the time range when the pressure measurements are above the atmospheric ambient pressure. Air rushes back into the tube after the pressure dips below atmospheric, and the pressure in the tube returns back to

ambient pressure. The tube is then filled with a detonatable mixture at 0.101 MPa and pressure profile of the cycle is repeated.

Figure 4.2 shows the static pressure profiles of four pressure transducers along the detonation tube for a fully-filled PDE at locations specified in Chapter 3. These pressure transducers are evenly spaced, and the equal separation of the incidence of the pressure spikes due to the detonation wave indicates that the wave is traveling at a relatively constant velocity along the tube.

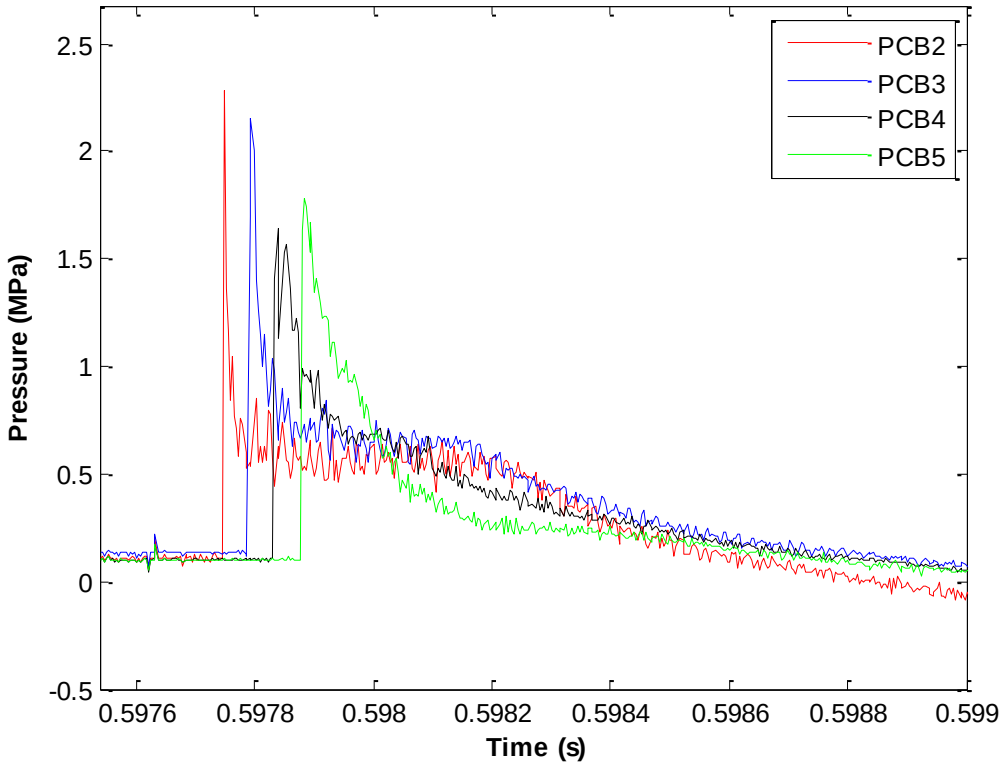

Figure 4.2 Pressure profiles along detonation tube.

The pressure profiles of PCB2 and PCB3 show a pressure plateau after the incident shock and before an exhaust expansion. The pressure profile of PCB4 shows a lower peak pressure value than PCB5 which is further downstream. This erratic detection of the peak is attributed primarily to the low sampling frequency of the DAQ system which can

sometimes miss the peak pressure of the traveling wave. PCB5 is mounted close to the exit of the detonation tube and the data show a strong expansion wave following the incident of the detonation wave. The detonation wave exits the detonation tube, transmitting a blast wave into the air and reflecting a strong expansion wave back into the detonation tube. The presence of this strong expansion wave can be seen by examining the decay profiles of the pressures within the tube at the various locations.

These pressure profiles are used to calculate the wave velocity by using the time-of-flight (TOF) method. Three wave velocities are calculated from the four pressure profiles and the corresponding values are presented in Figure 4.3.

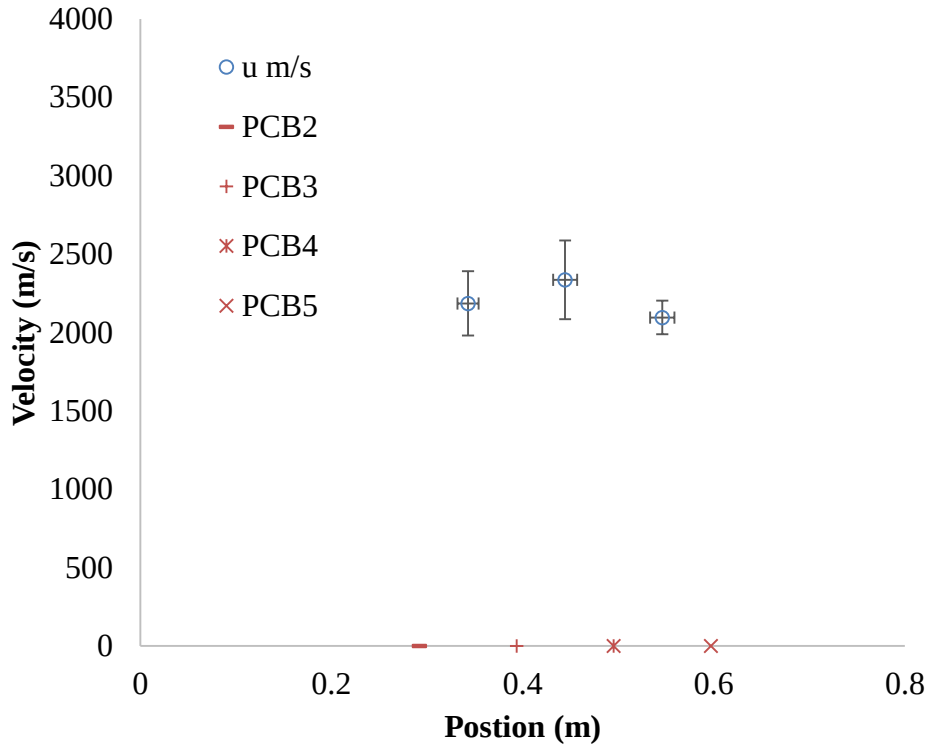

Figure 4.3 Detonation wave velocities in detonation tube.

The positions of each pressure transducer pressure PCB2-PCB5 along the detonation tube are represented in Figure 4.3 by symbols on the x-axis and corresponding

symbols in the legend, and the measured velocity between the pressure transducers is located halfway between them. For example, the positions of PCB2 and PCB 3 transducers on the detonation tube are highlighted by – and + symbols. The average detonation wave velocity along the tube is 2205 ± 199 m/s. This average wave velocity is 21% lower than the expected CJ velocity value for stoichiometric oxyhydrogen of 2800 m/s.

The uncertainty of the wave velocity is calculated by error propagation of the position error of the PCB transducers and the standard deviation of multiple time difference measurements. The position error for each velocity measurement is the sum of the 5.54 mm sensing diameter for each pressure transducer. As the sensing diameter of the transducer is the error of the location of the transducer itself.

The pressure profiles of PCB2 for multiple engines cycles are shown for 1 and 10 Hz in Figure 4.4. The detonation tube fill-fraction at both frequencies is 36%. These pressure profiles show that the peak pressures of the PDE at the same fill-fraction is invariant of the operational frequency.

The performance analysis of a PDE can be computed per pulse and without regard to the operational frequency since there are no pulse-to-pulse wave interactions. It is currently impractical to operate a PDE at frequencies where these wave interactions are possible. Therefore the experimental investigations in this work focused primarily on the system performance at 1 Hz, and can be generalized to higher frequency operation.

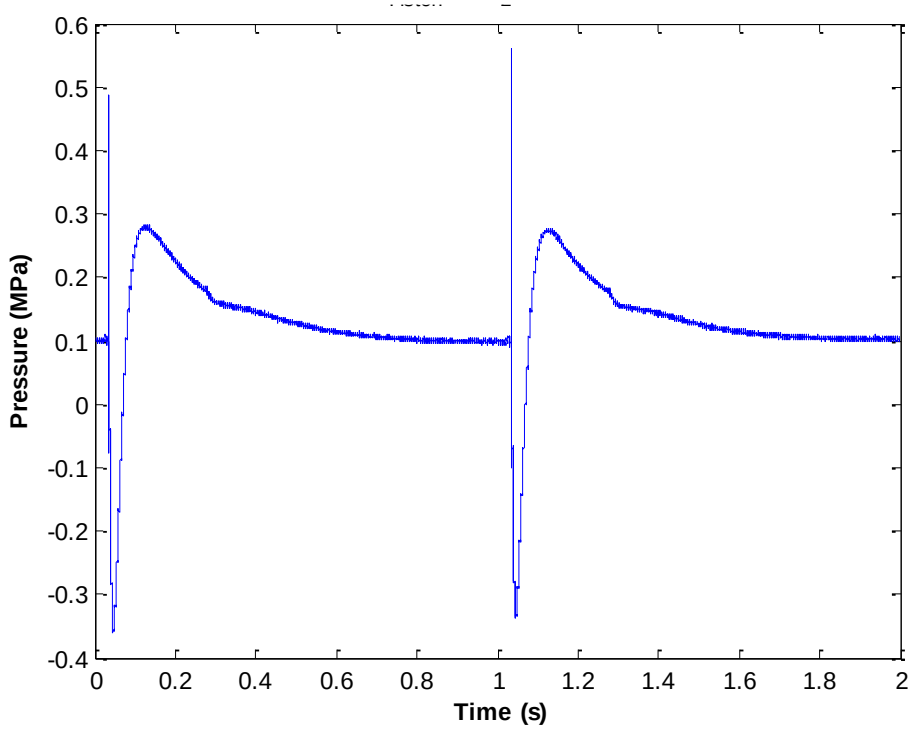

(a) 1 Hz.

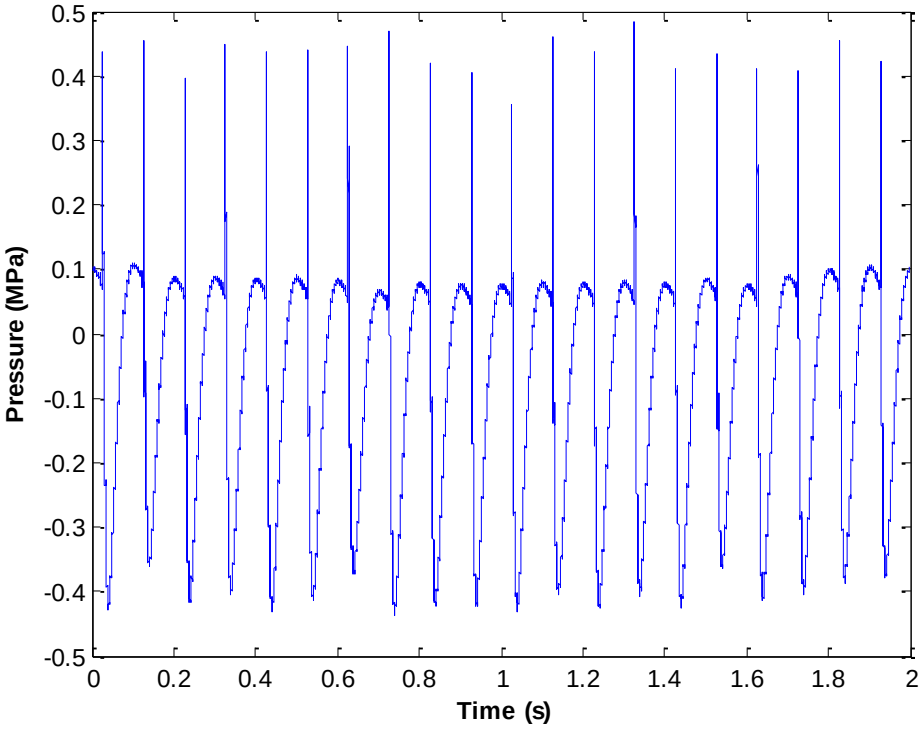

(b) 10 Hz

Figure 4.4 PCB2 pressure profile with 36% fill-fraction.

4.1.2 PDE Nozzle Performance

In addition to pressure measurements within the PDE, pressure profiles are measured within the nozzle at the nozzle-throat and nozzle-exit planes for different detonation tube fill-fractions. These measurements are performed in the facility configuration 2 described in Chapter 3. Figures 4.5(a) and (b) show the pressure profiles along the nozzle for a fill-fraction of 124% at the nozzle throat and nozzle exit planes.

The pressure transducers placed along the nozzle are recess mounted in water-cooled jackets. This type of mount reduces the response time of the pressure transducer to high-speed flows. The pressure spike of 0.9 MPa in the nozzle throat is below the predicted CJ pressure value of 1.8 MPa, which shows that the detonation wave degenerated to a blast wave due to the changing geometry even though the detonation tube is overfilled into the nozzle throat.

The burned gases at the nozzle throat expanded into the large area increase in the nozzle. The detonation wave breaks down into a blast wave as it travels though the nozzle. This blast wave is then accelerated toward the exit plane by the expansion in the nozzle.

The pressure of the gases at the exit plane increases over ambient pressure due to the transmitted shock from the detonation wave, and is diffused back to ambient pressure very rapidly as shown in the Figure 4.5(b). The pressure at the nozzle exit plane fluctuates around the ambient value as various wave processes occurs to equilibrate the entire tube volume back to ambient pressure.

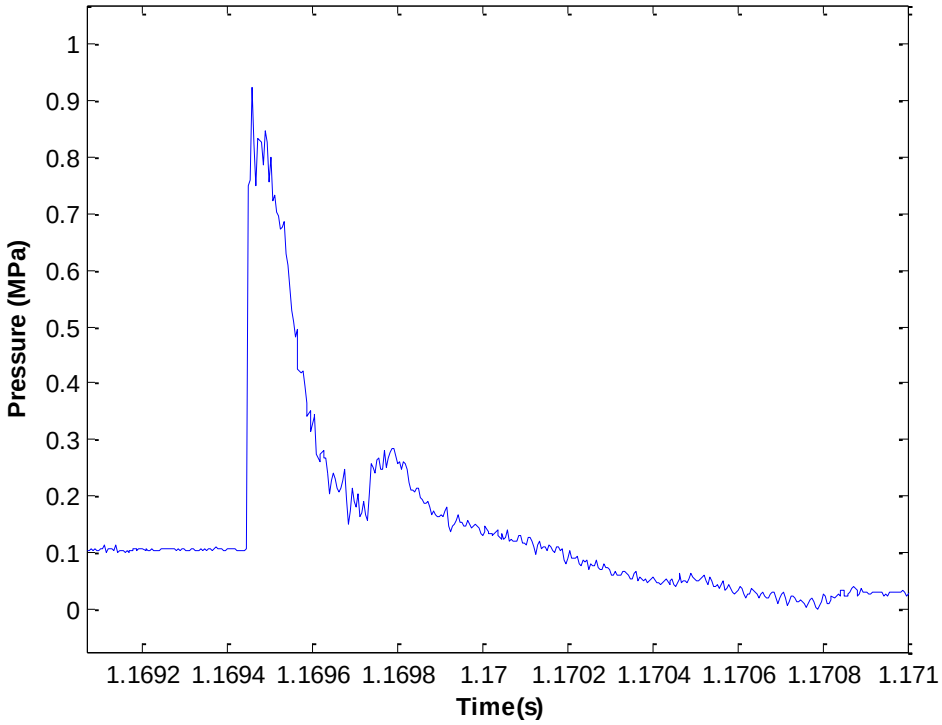

(a) Nozzle throat.

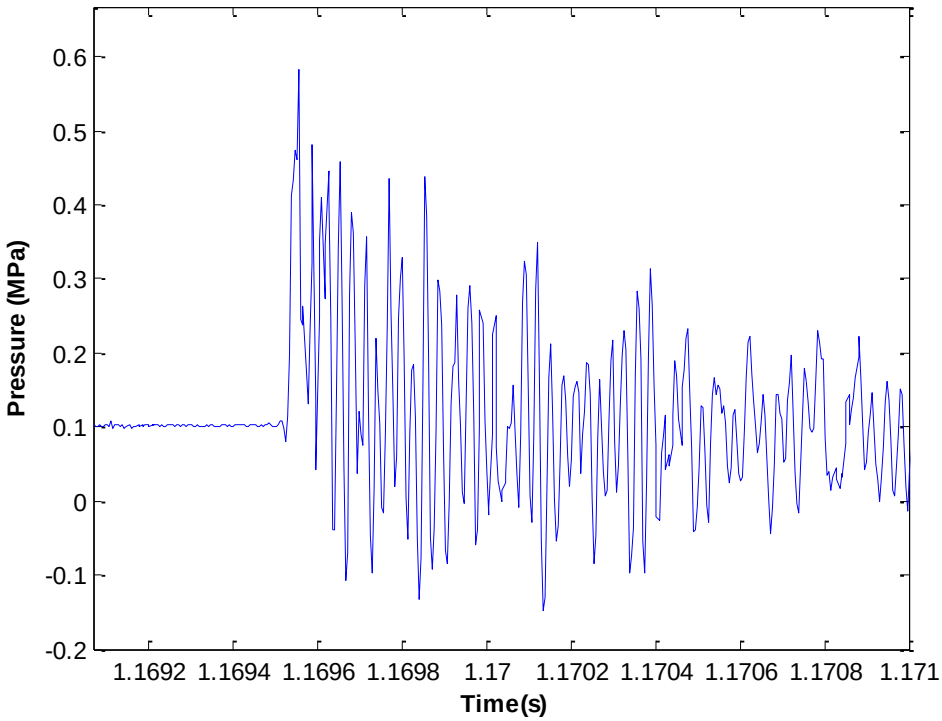

(b) Nozzle exit.

Figure 4.5 Pressure profiles on PDE nozzle with 124% fill-fraction.

The nozzle overexpands the exhaust gases causing a retonation wave to form in the nozzle and travel upstream toward the nozzle throat. The incidence of this retonation wave is present in the pressure profile of the nozzle throat shown in Figure 4.5(a), and causes the pressure to rise and briefly plateau at a constant pressure, at t = 1.1698 s. Exhaust rarefaction wave travels from the exit nozzle plane toward the nozzle throat and reduces the pressure within the tube to sub-atmospheric values. Ambient air rushes in through the nozzle to increase the pressure in the nozzle and tube back to atmospheric values.

Similar to pressure profile results of configuration 1 presented in section 4.1.1, the pressure profiles of all the transducers along the PDE including the pair at the nozzle throat and exit planes are presented in Figure 4.6, corresponding to PCB6 and PCB7 respectively. The pressure spike of the four pressure transducers PCB2-PCB5 are consistent and matches the predicted CJ pressure of 1.8 MPa. This shows that the detonation wave maintains a relatively constant gas state as it travels down the detonation tube. In comparison, the pressure spike at the at the nozzle throat drops to 0.9 MPa, about half the value of the pressure spike within the detonation tube, while the pressure spike at the nozzle exit drops to 0.6 MPa due to the expansion of the shock wave along the nozzle. The shock wave that traveled upstream towards the nozzle throat due to over-expansion of the exhaust traveled further upstream through the entire detonation tube and can be tracked from the various pressure profiles.

The incidence of the pressure spikes at the various transducer locations is used to compute the detonation wave speed within the tube, and the shock wave velocity within the nozzle. These velocities are presented in Figure 4.7. The positions of each pressure transducer PCB2-PCB7 along the detonation tube and nozzle are represented in Figure 4.7

by symbols, and the measured velocity between the pressure transducers is located halfway between them. For example, the positions of PCB6 and PCB7 transducers at the nozzle throat and nozzle exit plane are highlighted by ◊ and ▲ symbols on the x- axis.

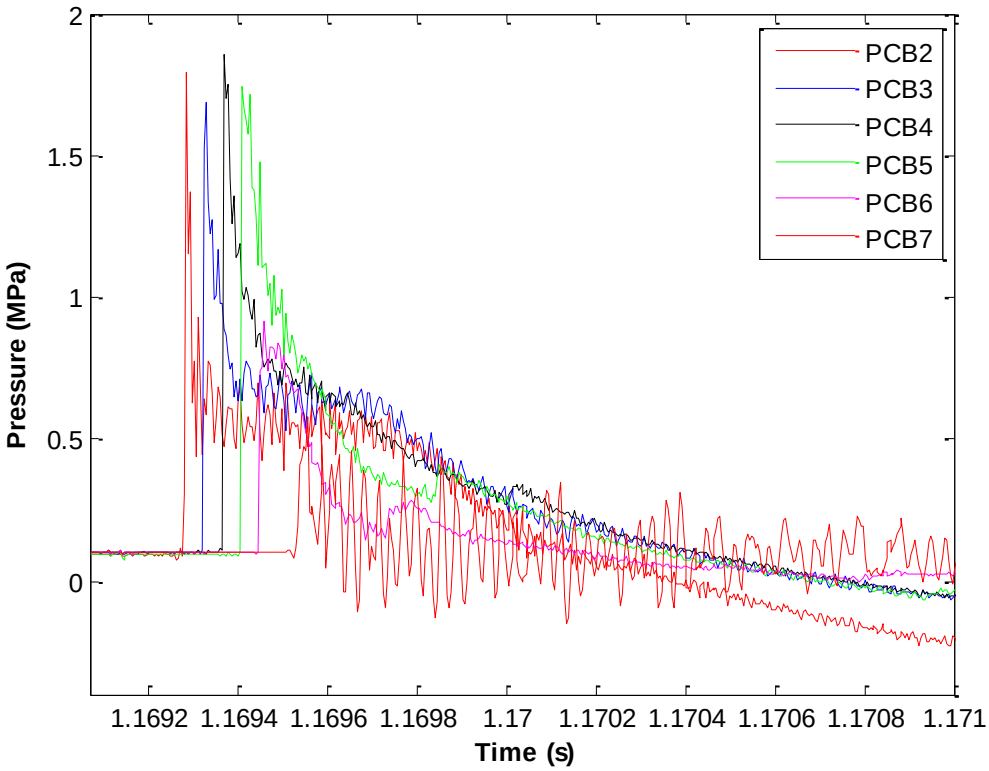

Figure 4.6 Pressure profiles along detonation tube and nozzle.

The average detonation wave velocity within the tube is 2400 ± 170 m/s, and the transmitted shock velocity in the nozzle is 1850 ± 190 m/s. These velocity measurements show that the velocity of the travelling wave drops by 500 m/s as it transitions from a detonation wave to a blast wave, and is then accelerated with an additional velocity of 227 m/s through the nozzle.

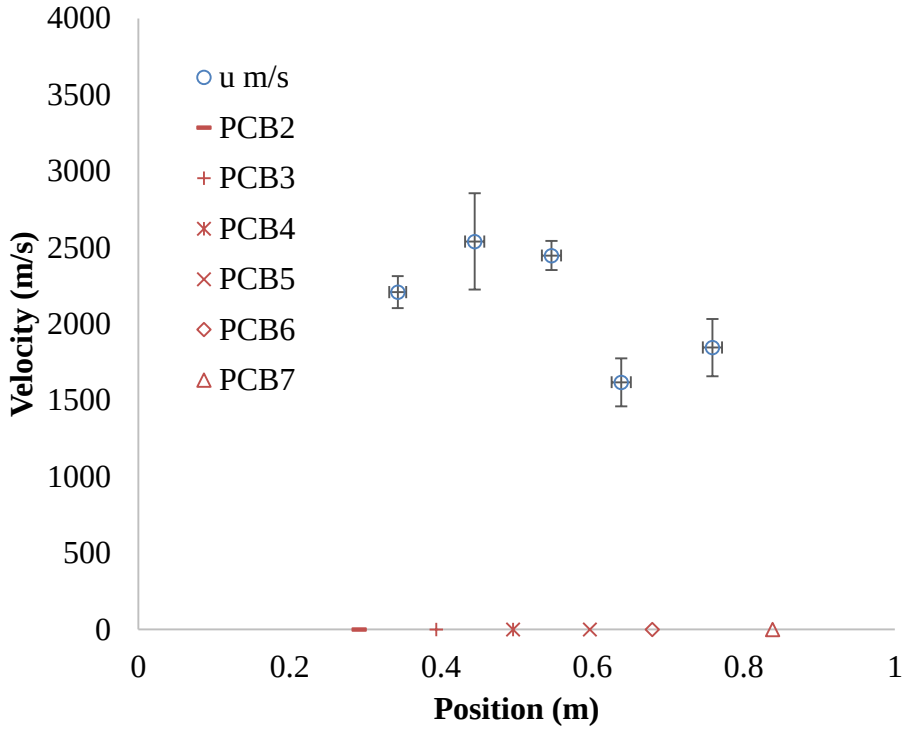

Figure 4.7 Detonation wave velocities in detonation tube and nozzle.

The static pressures at the nozzle throat and nozzle exit plane are recorded for fill-fractions ranging from 11% to 240%, and are presented in Figure 4.8. The pressure at the nozzle throat is generally higher than the pressure at the nozzle exit, and increases with fill-fraction. The stagnation-to-static exit pressure ratio across the nozzle is calculated based on the assumption that the flow is choked at the throat. Therefore, the ratio of the throat static-to-stagnation pressure is 1/0.528 for $\gamma = 1.4$ which corresponds to air, and $\gamma = 1.13$ for stoichiometric oxy-hydrogen detonation products. These pressure ratios are presented in Figure 4.9. The nozzle exit Mach number is then calculated from the pressure ratios and is presented in Figure 4.10. These results show that the exit Mach numbers of the nozzle are invariant of the fill-fraction until the entire nozzle is fully-filled with a detonable mixture. The average nozzle exit Mach number for the partially filled PDE with nozzle is 2.44 ± 0.06.

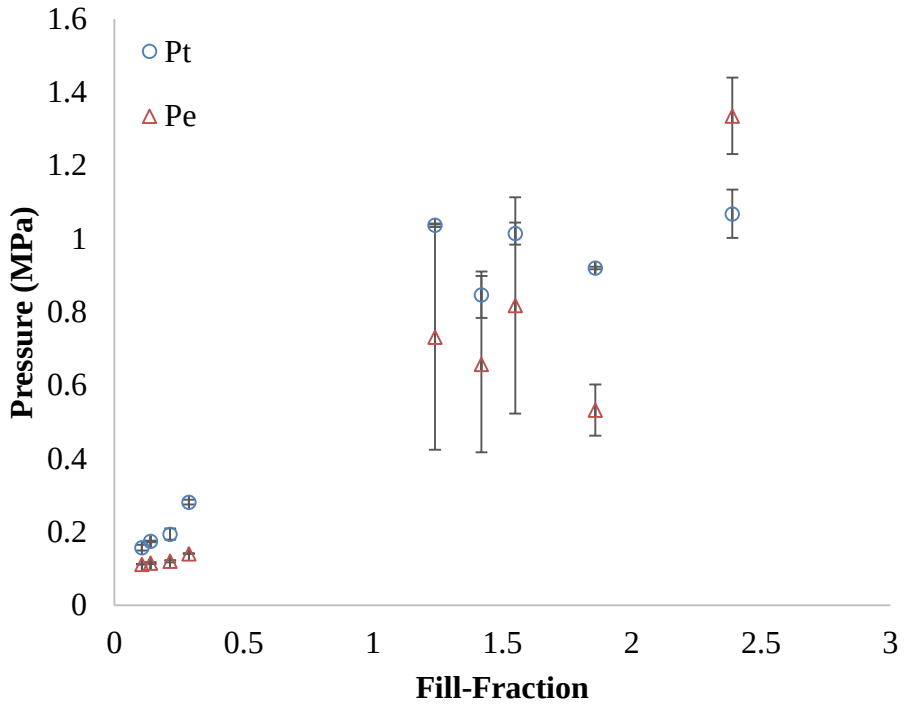

Figure 4.8 Nozzle throat and exit pressures for varying fill-fraction.

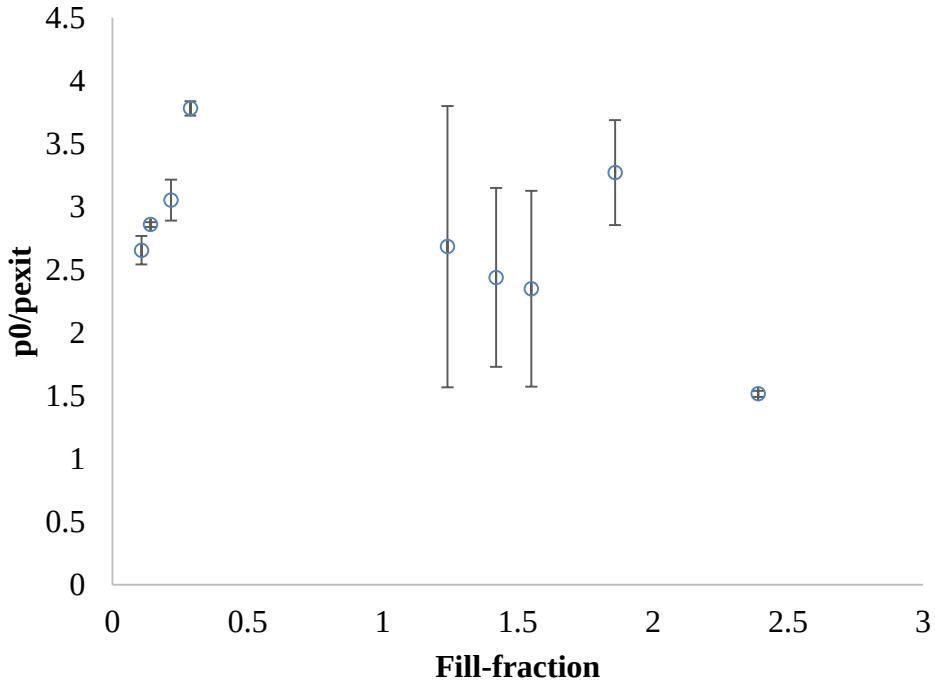

Figure 4.9 Stagnation pressure ratio across nozzle exit pressure.

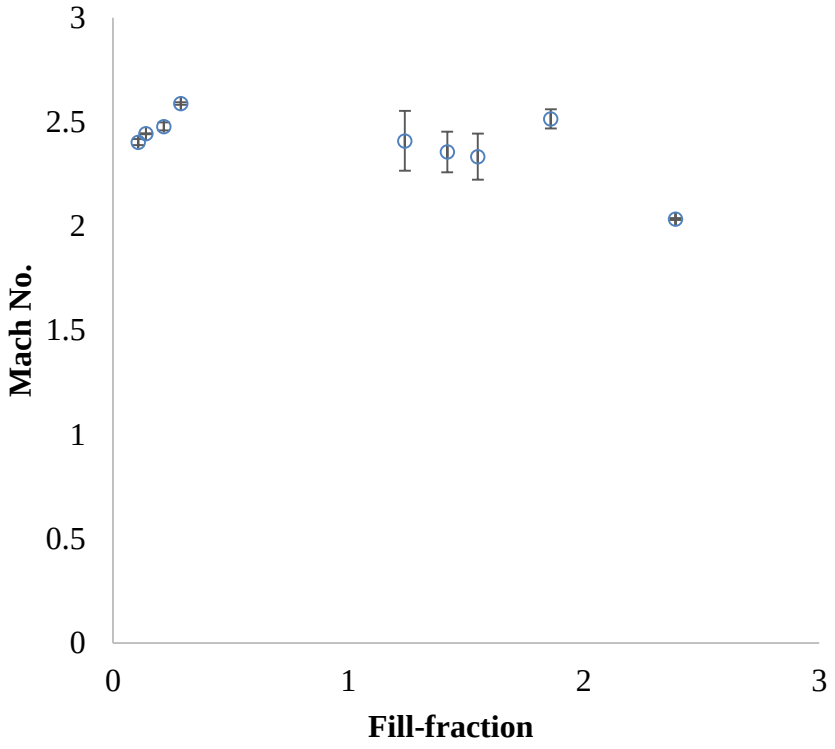

Figure 4.10 Nozzle exit Mach number for varying fill-fraction.

4.1.3 PDE and Nozzle Specific Impulse

The performance improvements of the nozzle on the PDE can be quantitatively determined by comparing the thrust output of facility configurations 1 and 2. A dynamic load cell placed between the PDE thrust wall and thrust wall plate records the force generated by the PDE. The dynamic load cell used for force measurement is preloaded to 200 lbf (900 N). This load cell only reads compressive loads. Therefore, negative force readings are disregarded. The performance of the PDE configurations is determined from the thrust measurement and integration of the thrust measurement over time to compute the impulse. The thrust data are integrated about the peak compressive load in the region where a positive force is recorded. The impulse is analogous to momentum, and is generally normalized by the area where the force is applied.

The thrust profiles at a fill-fraction of 124% for the PDE only, and PDE with nozzle configurations are presented in Figure 4.11(a) and (b). The peak force of configuration 1 with just the PDE is 250 N, while the peak force of configuration 2 of the PDE coupled the nozzle is 400 N, an increase of 60%. This shows that from a thrust production perspective, the PDE with a nozzle produces a significantly better performance than just the PDE alone.

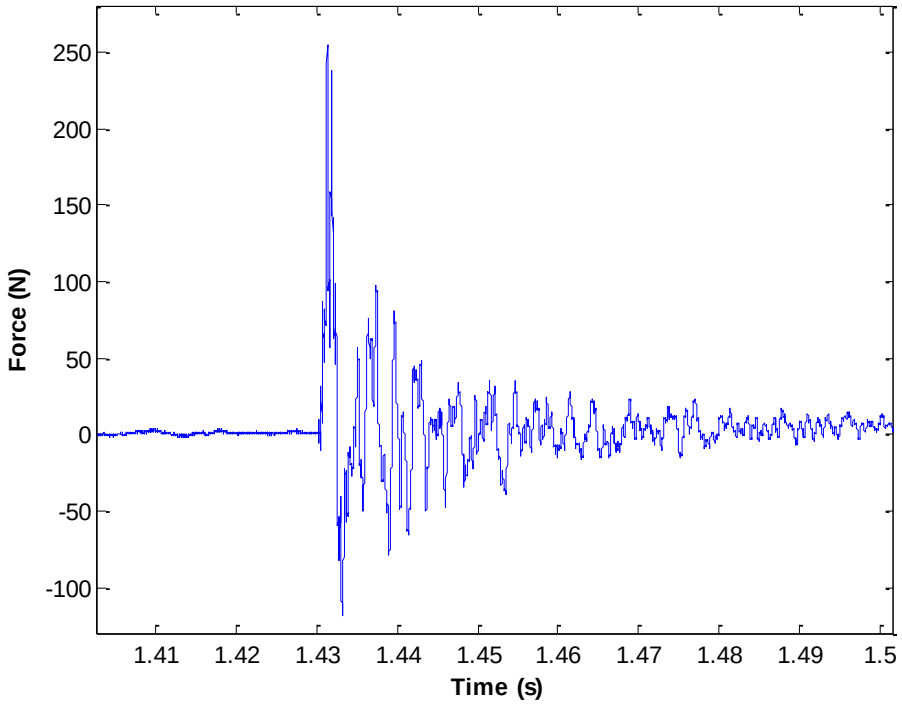

(a) PDE.

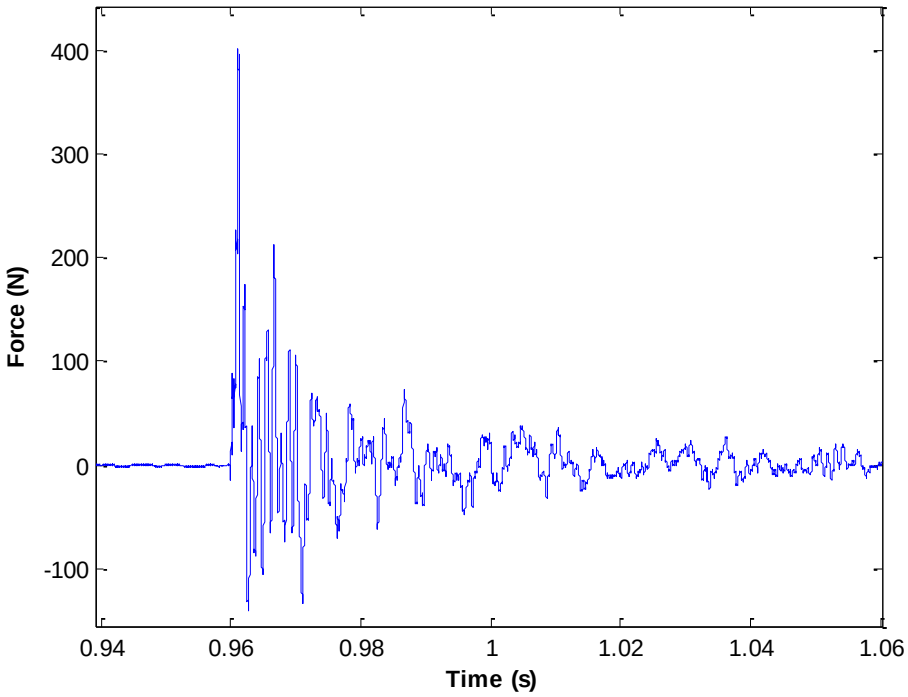

(b) PDE with nozzle.

Figure 4.11 PDE thrust measurements at 124% fill-fraction.

The average impulse measurements of the two PDE configurations for various fill-fraction operation are plotted in Figure 4.12. The standard deviation error bars of the average impulse measurements are also plotted. As can be seen, the impulse increases linearly with increasing fill-fraction. The PDE configuration with a nozzle generally produces a higher impulse than the configuration without. Attempts to operate at fill-fractions lower that 11% did not yield successful detonations. For detonation tube overfilled cased, where the fill-fraction is greater than 1, the impulse drops while with the nozzle the impulse continues to increase linearly when the PDE is overfilled. This is because the fill-fraction is defined based on the detonation tube volume, and the addition of the nozzle effectively increases the overall detonation chamber volume, while in the

PDE-only configuration the overfilled case draws the reactant out of the tube into the ambient.

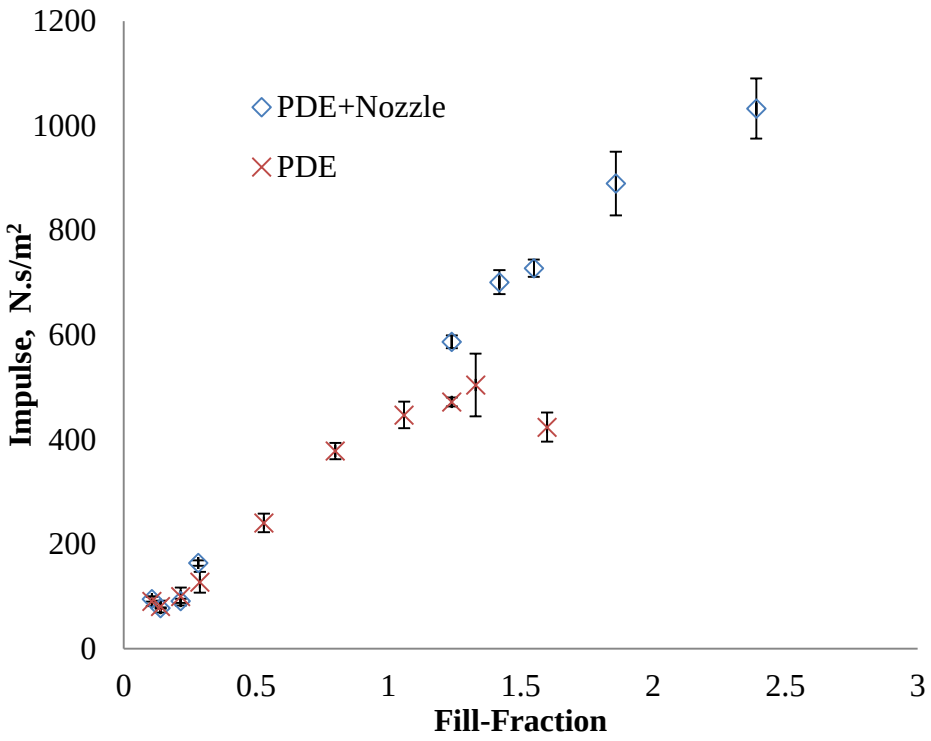

Figure 4.12 Impulse of PDE with and without a nozzle.

The specific impulse of the PDE configurations is plotted in Figure 4.13. The specific impulse normalizes the measured impulse by the corresponding fuel-oxidizer mass. Therefore, the specific impulse of the PDE at lower fill-fractions is higher due to the smaller amount of fuel used to generate the impulse. This plot clearly shows that it is more fuel efficient to operate the PDE at a lower fill-fraction, and with a nozzle.

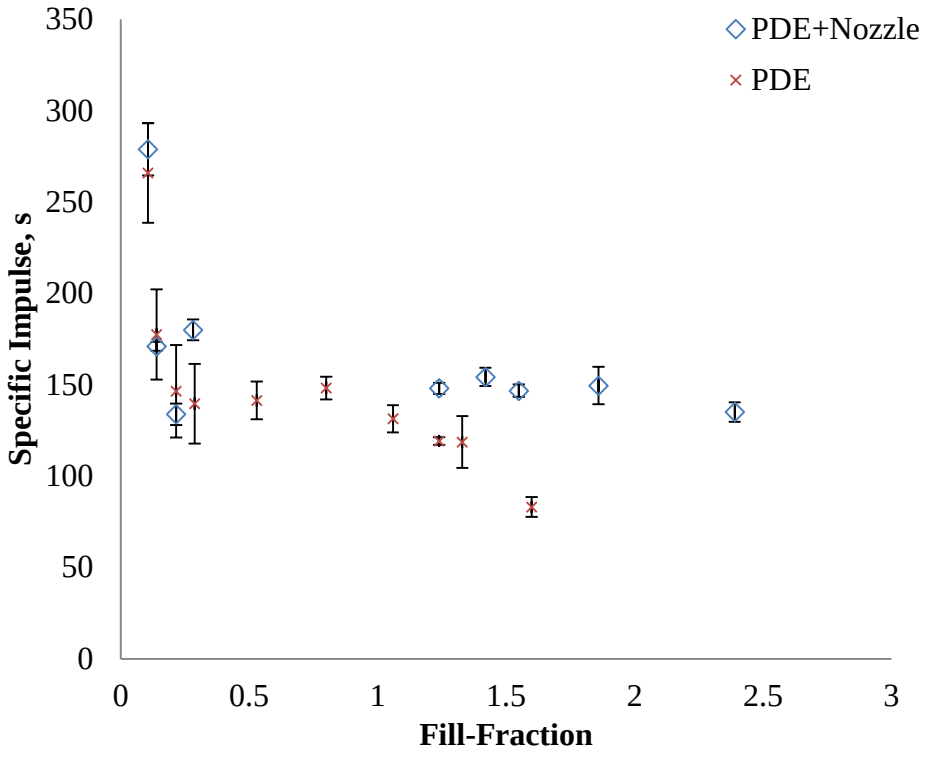

Figure 4.13 Specific impulse of PDE with and without a nozzle.

More common in the literature is the fuel-based specific impulse shown in Figure 4.14. This is calculated simply by normalizing the impulse of the engine only by the mass of the fuel and neglecting the mass of the oxidizer. The fuel-based specific impulse is the most common metric for comparing the performance of various engines. As shown by Figures 4.13 and 4.14, the trends for the general and fuel-based specific impulse are similar. Differences in the trends would be pronounced if the equivalence ratio of the fuel-oxidizer mixture is varied.

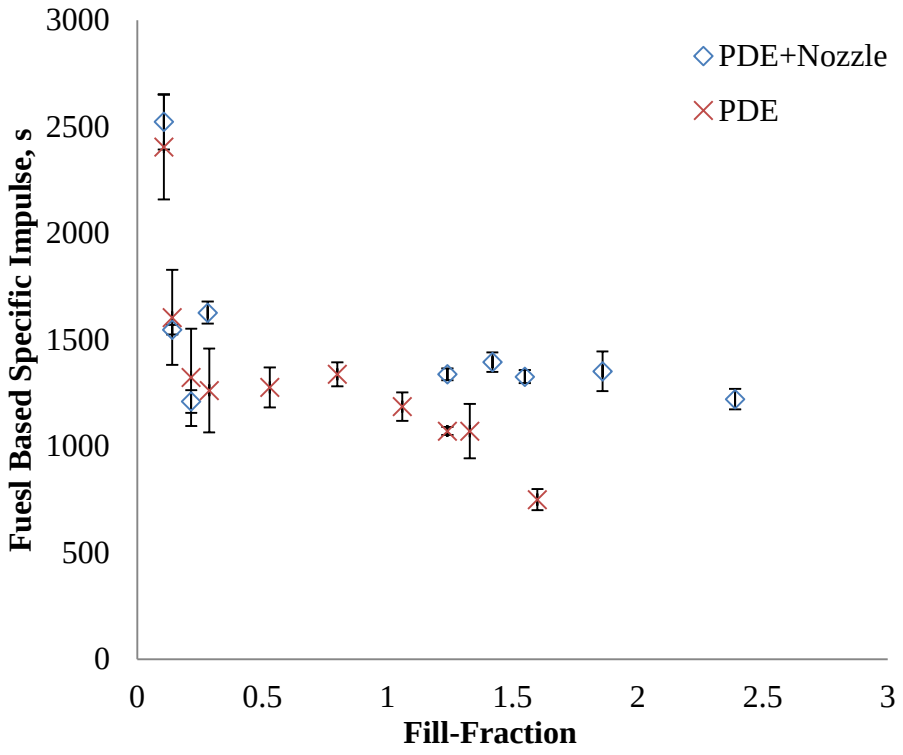

Figure 4.14 Fuel-specific impulse of PDE with and without a nozzle.

Close examination of Figures 4.12 and 4.13 for the PDE only configuration, reveals a linear relationship of PDE impulse in the partially-filled scale, and a linear relationship of PDE specific-impulse in the over-filled scale. However, for PDE configuration 2 with the nozzle, there is a linear relationship of PDE impulse for the entire fill-fraction scale examined. It is possible that the specific impulse of the PDE with nozzle begins to decrease after it is fully filled with fuel and oxidizer at fill-fractions above 240%, but experiments were not conducted at these scales due to safety considerations of the facility integrity from the high impulses produced at that scale. The specific impulse and fuel-based specific impulse data presented over both scales show that the optimally efficient operating condition for the PDE-LPG system is at low fill-fractions and with a nozzle.

4.1.4 Sound Level

The high sound levels emitted by the PDE are often cited as one of the key challenge to its practicality. Therefore, monitoring this sound level provides understanding of the noise levels produced by the proposed PDE-LPG system. The sound levels 3 ft away from the exhaust openings of only PDE and the PDE configured with the diverging nozzle are presented in Figures 4.15 and 4.16. These plots show that the sound level increases logarithmically with fill-fraction. The trend line equations and regression fit values for these plots are: $MSL = 6.58\ln(ff) + 99.55$ with $R^2 = 0.994$ for Figure 4.15 and $MSL = 4.93\ln(ff) + 107.3$ with $R^2 = 0.992$ for Figure 4.16, where MSL is the maximum sound level, and ff is the fill-fraction.

The solid lines in both of these figures are logarithmic trend line fits to the data. Higher fill-fraction experiments are not performed because the sound levels exceed the measurement range of the microphones used. The PDE-nozzle configuration produces higher sound levels than the simple PDE only configuration. The quantitative effect of the higher noise produced with the nozzle is also illustrated by the y-intercept constant of the trend line equation which is 8 dB higher. The diverging nozzle accelerates the shockwave and has a larger exit area, thereby enabling a larger pressure disturbance at the exit.

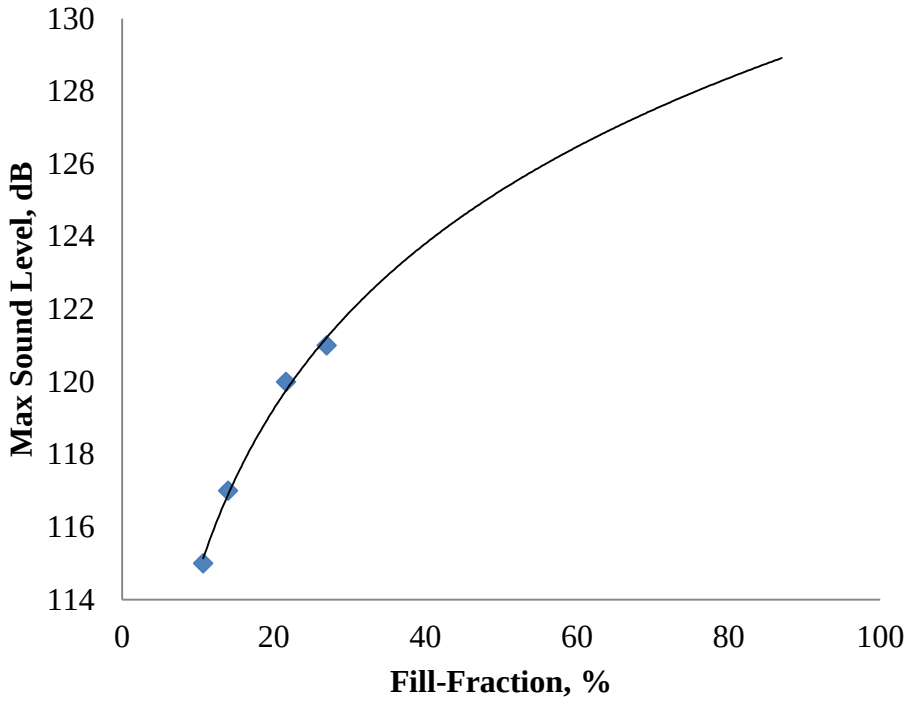

Figure 4.15 Sound level 3ft away from PDE exit.

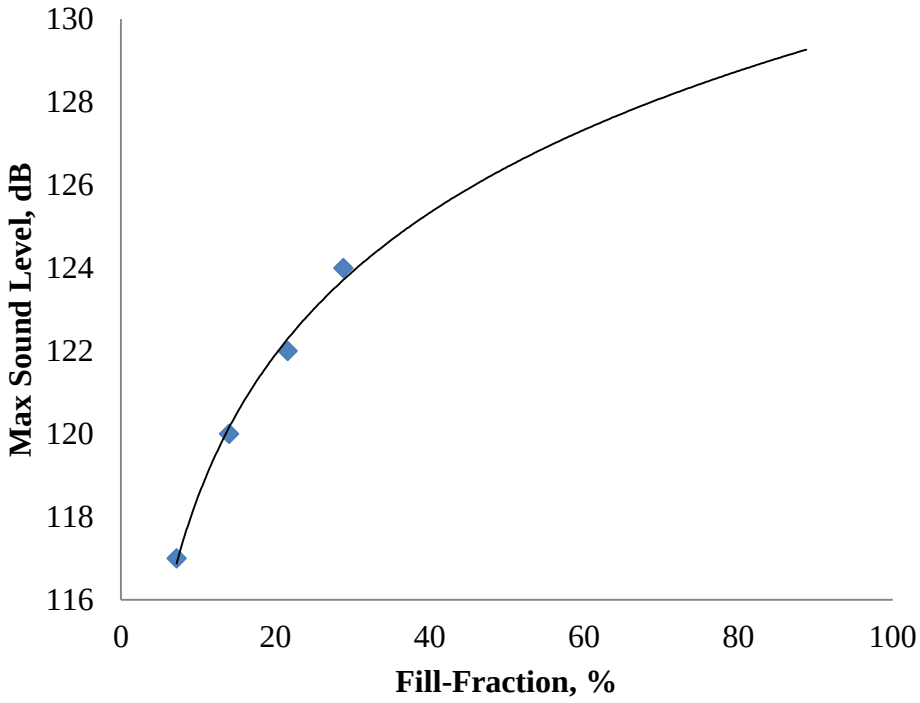

Figure 4.16 Sound level 3ft from PDE-nozzle exit

4.1.5 PDE Piston Pressure and Spring System Response

In facility configuration 3 discussed in the experimental setup, a 10 in. ID piston is added to the PDE with the nozzle from configuration 2. In this new configuration, the performance of the piston is independently examined through pressure measurements on the piston face and displacement measurements of the piston-spring system due to the PDE exhaust pressure loading. The pressure on the piston face is measured at the center of the piston, which is axially aligned with the center of the nozzle exit plane, and at 3 in. away from the center of the piston. Pressure profiles at the two piston face locations are shown in Figure 4.17.

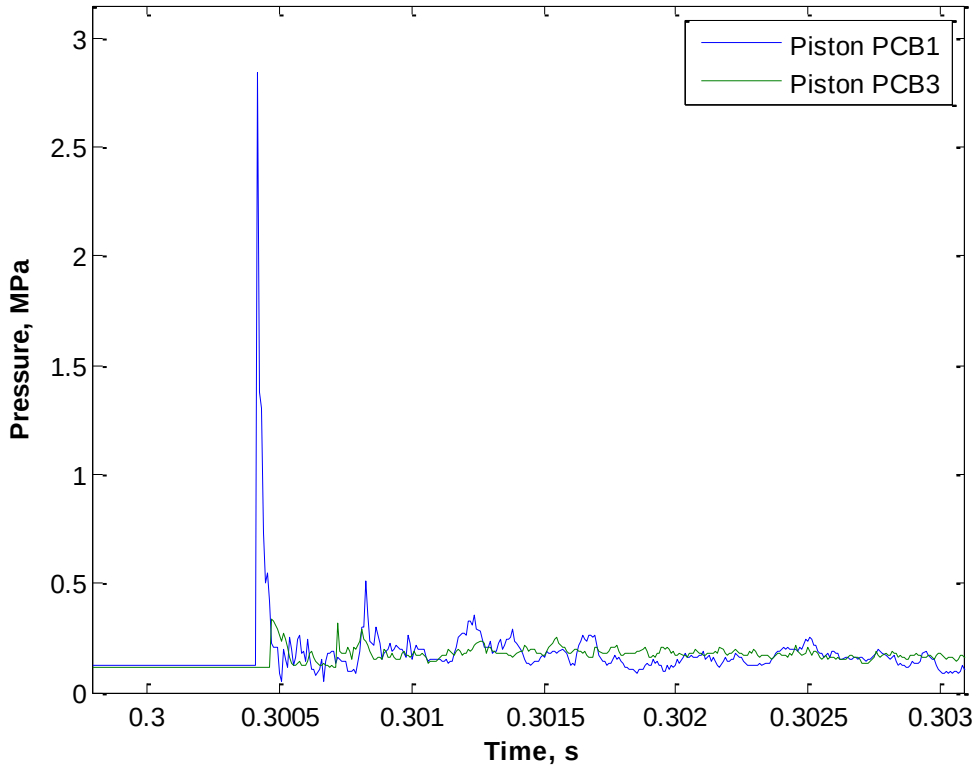

Figure 4.17 Pressure profile on piston face center and 3 in. away from the piston center for 106% fill-fraction.

These piston face pressure profiles show the stagnation pressure of the reflected shock wave, and they follow the Friedlander decay profile for a blast wave. The reflected pressures at the piston face for varying fill-fraction are presented in Figure 4.18. These pressure values are used to calculate the pressure work done by the PDE with nozzle on the piston.

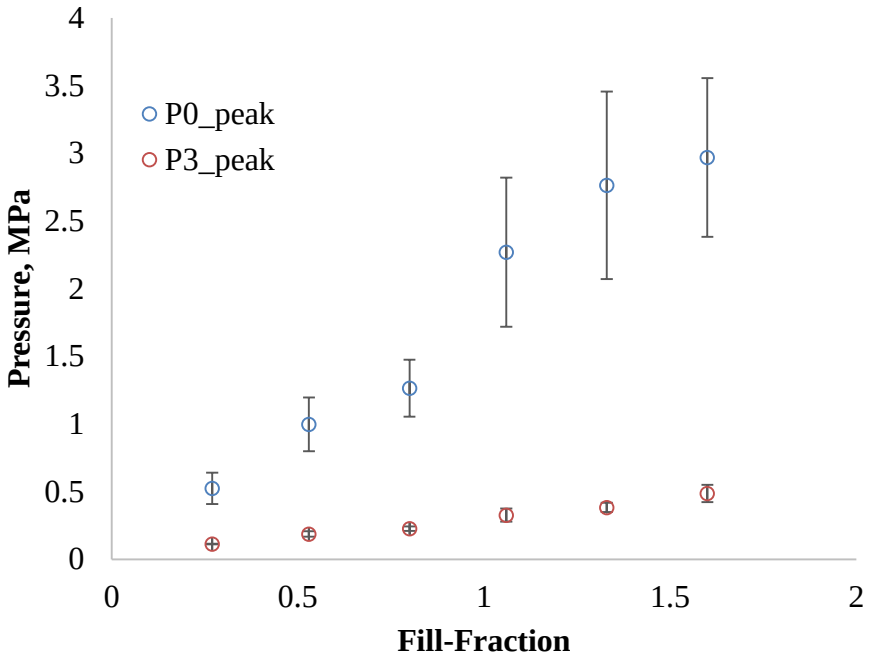

Figure 4.18 Peak pressure on piston face center and 3 in. away from the piston center for varying fill-fraction.

The PDE is operated at a frequency of 1 Hz and drives the resonator system which included the U-shaped piston coupled with compression springs. A linear variable displacement transducer (LVDT) is placed at the center of the piston to track its displacement back and forth. The resultant displacement of the resonator system for a 100% PDE fill-fraction operating at 1 Hz is shown in Figure 4.19.

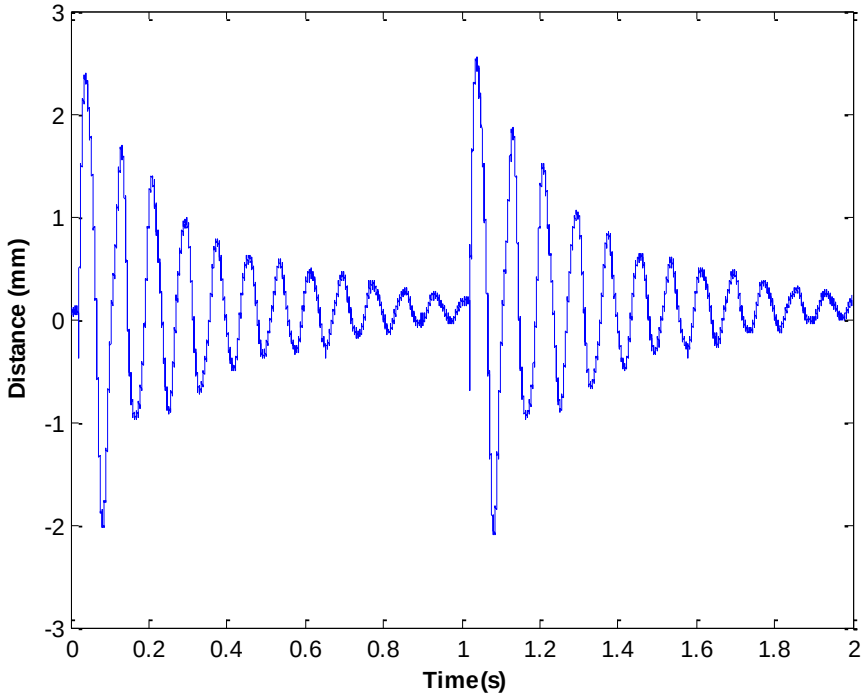

Figure 4.19 Displacement response of piston-spring system.

The displacement response shows that the system is under-damped. Using the logarithmic decrement method, the damping ratio is calculated to be $\zeta = 0.05$. The calculated damping ratio of 0.05 is relatively low as subsequent pulses are able to interact with the system before the response decayed back to its nominal position. It can also be seen that the resonator vibrates at its damped frequency. The damped natural frequency is determined by performing a fast-Fourier transform (FFT) on the displacement data as shown in Figure 4.20.

Based on the peak of the FFT plot, the displacement data shows that the system is vibrating at a damped frequency of 12 Hz. Therefore, using the damping ratio of 0.05 and the damped frequency of 12 Hz, the natural frequency of the system is calculated to be 12.02 Hz. This FFT plot of the displacement data also reveals that the system vibrates very

simply and that high-order harmonics that would otherwise be present at 24, 36 Hz, etc. have no prominence within the system.

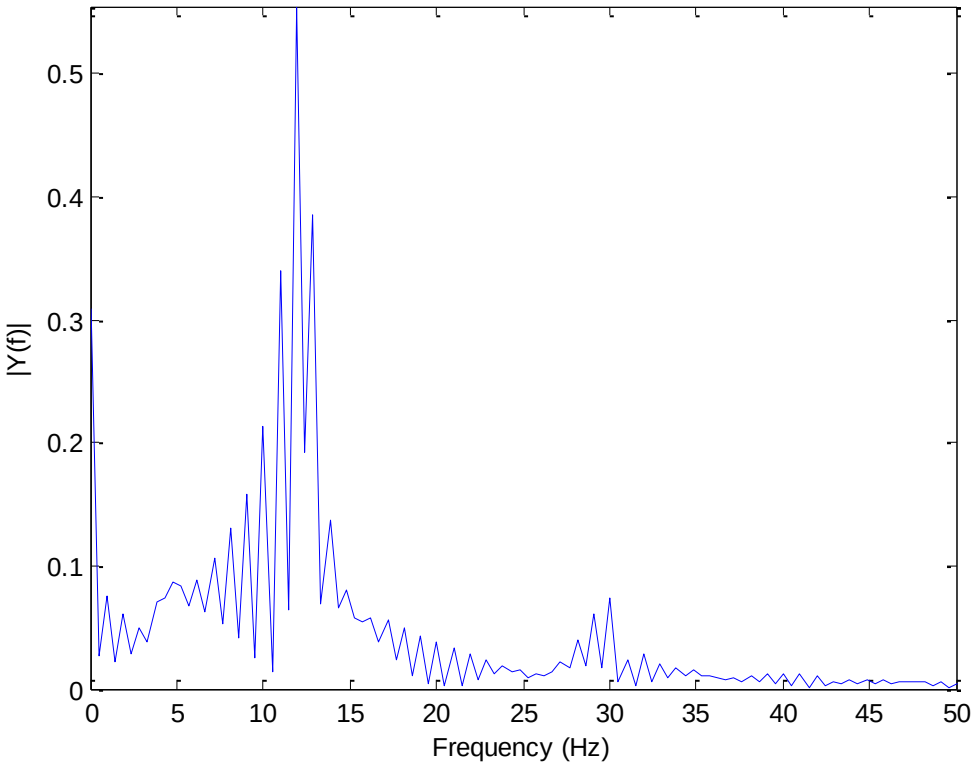

Figure 4.20 Single-sided amplitude spectrum of piston displacement.

The same experiments are repeated for various fill-fractions, and the maximum displacement amplitude of the piston is recorded in Figure 4.21. This shows that there is a linear increase in the performance of the PDE-LPG system up to the overfilled region of 130%, after which the addition of more fuel and oxidizer increased the piston displacement further, but not at a higher rate compared to the partially-filled operation. Therefore, PDE-overfilling would yield lower fuel efficiency relative to the partially filled operation. Also, the damped frequency of the piston-spring system is measured to be invariant to fill-fraction.

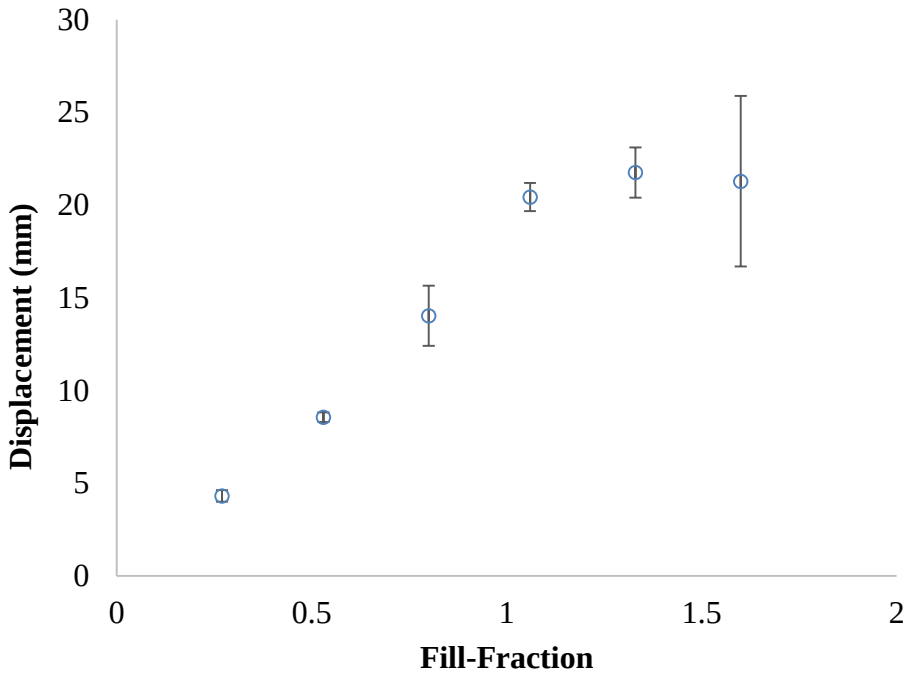

Figure 4.21 Effect of PDE partial-filling on displacement.

4.1.6 PDE – LPG Slider Displacement, Electric Voltage, Current and Power

The final configuration of the facility discussed in the experimental setup allows for measurement of the pressure profiles along the PDE and the nozzle, the linear power generator (LPG) slider displacement, and the LPG current and voltage output. This section presents the results of the LPG system for various fill-fractions and electrical loads. The piston is placed directly over the 10 in. nozzle exit flange, and directly connects to the LPG slider. Therefore, the mechanical subsystem is a SDOF system described in Chapter 2, and the motion of the LPG slider and piston are equivalent. In this configuration, the motion of the piston-slider mass is overdamped, due to the piston enclosure which forces the piston to create a vacuum or compress the gas in the PDE with nozzle under free vibration. Figures 4.22 to 4.26 present the results of the slider displacement, LPG voltage, current and power for a PDE tube fill-fraction of 106%.

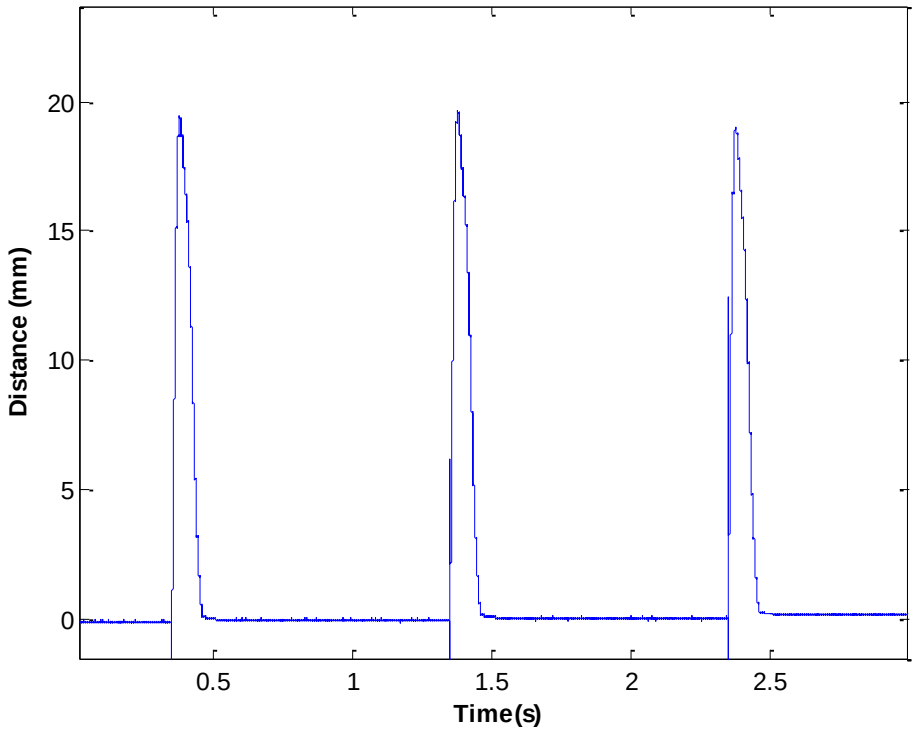

Figure 4.22 Displacement of LPG slider for 106% fill-fraction.

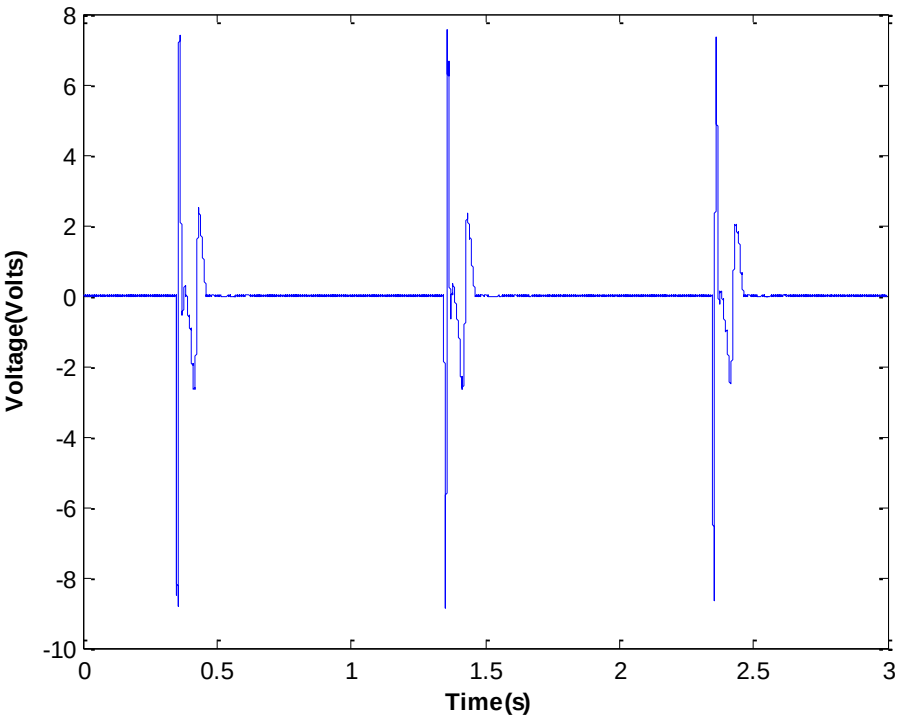

Figure 4.23 Voltage generated in LPG stator for 106% fill-fraction.

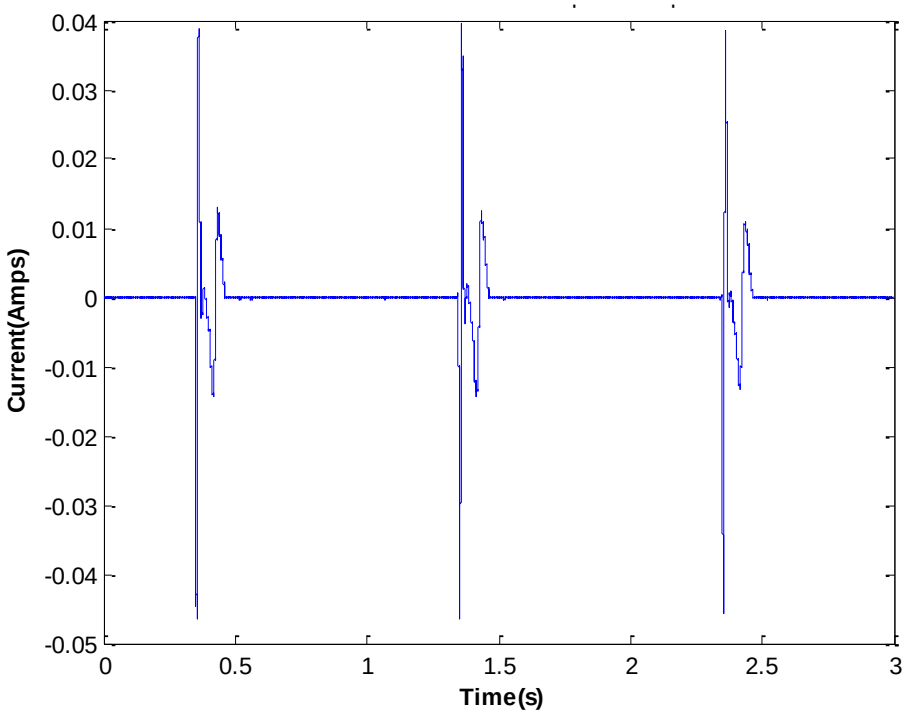

Figure 4.24 Current in LPG stator for 106% fill-fraction.

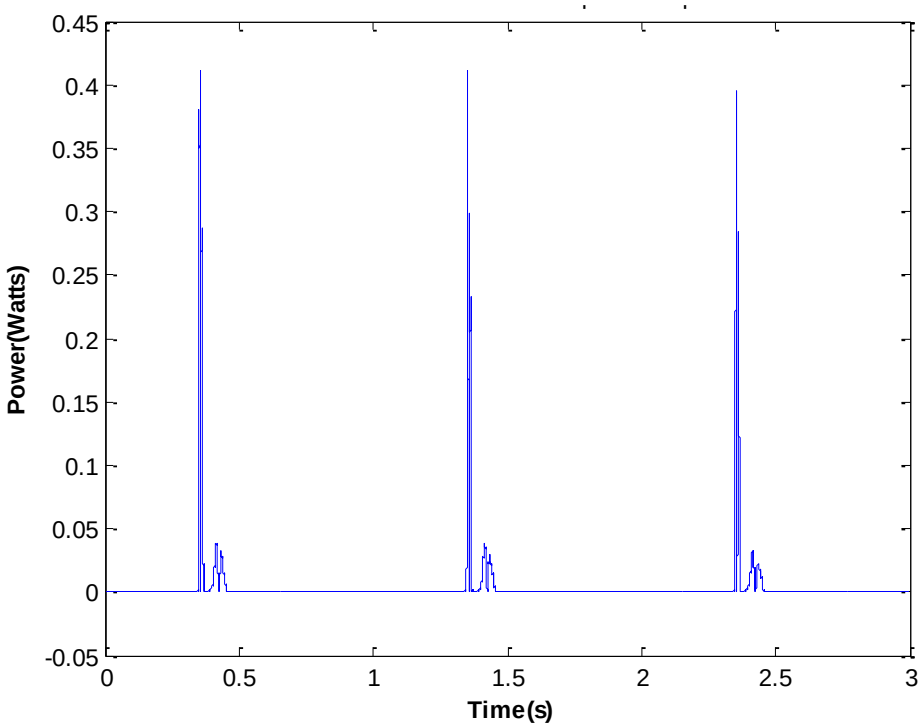

Figure 4.25 Power of LPG 106% fill-fraction.

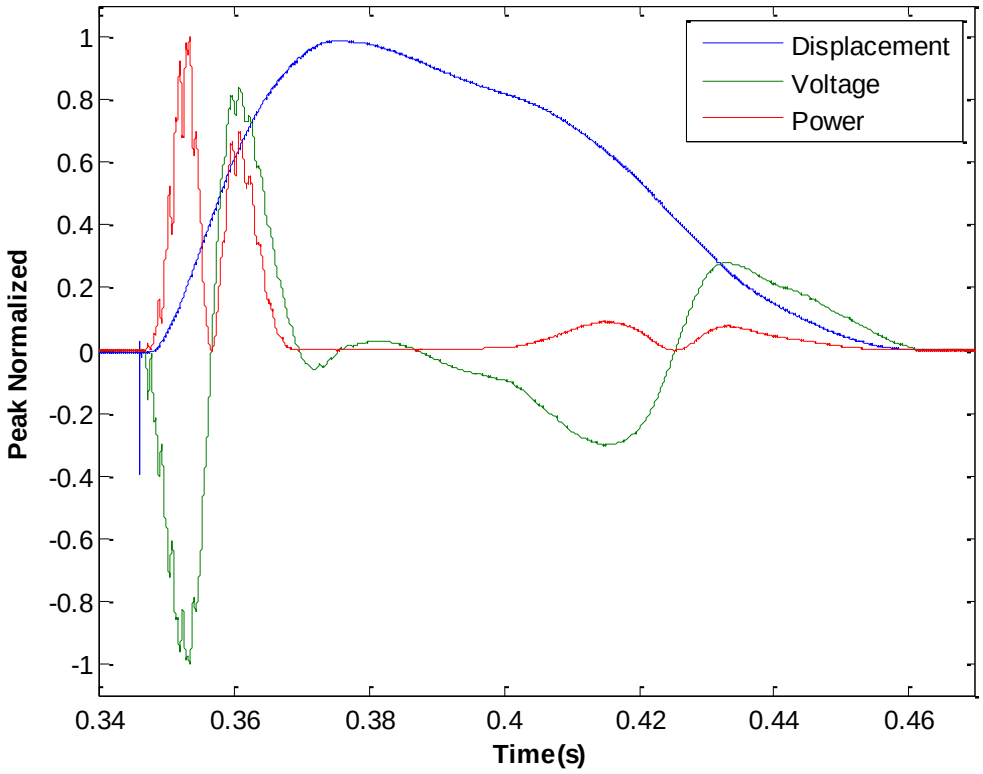

Figure 4.26 Normalized LPG slider displacement, stator voltage and power.

The piston-slider displacement displayed in Figure 4.22 shows that the mechanical subsystem of the facility is an overdamped SDOF system. This severe damping resulted in significant efficiency losses for the overall system. The high-pressure blast wave from the PDE with nozzle drove the U-shaped piston away from the nozzle exit plane, and the piston is returned back to its nominal position of 2 in. away from the nozzle exit plane by compression springs. The cycle is then repeated with successive firings of the PDE at 1 Hz. The displacement profiles of the piston-slider shown in Figure 4.22 also elucidate that the SDOF response is stable as the mass always returns back to its nominal position, and repeatable as the maximum displacement from the same fill-fraction is equivalent.

The voltage and current generated in the LPG stator by the motion of the LPG slider magnets are measured simultaneously, and are shown in Figures 4.23 and 4.24. The two

phases of the LPG are combined to provide a single pair of positive and negative electrical output terminals. The voltage across this pair of terminals is directly measured by the DAQ. For the current measurement, a simple shunt and load resistor circuit is connected to the terminals. A resistive load of 175 Ω is placed in the circuit in series with a 15 Ω shunt resistor. The current flowing through the resistive load and the shunt resistor are equivalent because they are connected in series. The voltage drop across the shunt resistor is measured, and the current is calculated using Ohm's law. Since the applied electrical load is purely resistive, there is no reactance creating a phase lag. Therefore, the current and voltage measurements in time generate the same trends.

The electrical power is calculated by multiplying the measured current and voltage and is shown in Figure 4.25. This plot shows that there are two distinct phases of power generation during the motion of the LPG slider, separated by flat line of zero power at maximum piston displacement, which occurs at t = 0.35 seconds. The first power generation phase occurs as the piston-slider was pushed back very rapidly due to blast wave pressure of the piston face, yielding a peak power of 0.4 W. The second power generation phase occurs as the piston is spring returned relatively slowly to its nominal position away from the nozzle exit, yielding a peak power of 0.04 W. In both cases regions, the LPG slider covers the same displacement, but the drastic difference in the slider velocity yields a peak power difference of an order of magnitude. Therefore, it is important to design a piston return mechanism capable of returning the piston-slider to its nominal position at a comparable speed to being driven by the blast wave. It is also possible to decouple the motion of the piston and the slider in order to have the displacement response of the slider

be maintained at a constant velocity in order to achieve uniform power dissipation by designing a MDOF system.

The effect of the slider velocity in creating these two power zones can be more clearly seen in Figure 4.26, which shows an overlay of the peak normalized displacement, voltage and power. The plot overlay indicates that peak electrical voltage and power generation occurs at peak slider velocity. An AC electrical cycle is completed in half the period of the overdamped slider displacement profile. This is because as the piston-slider moved from its nominal position to its peak displacement, the rate of change of voltage is directly related to the rate of change of the slider velocity. Therefore, the voltage is negative when the slider is accelerated to its maximum velocity, and then becomes positive as it decelerates to reach the maximum displacement. The peak voltage and peak power of each half electrical period occurs at maximum slider acceleration and deceleration. When the slider velocity is at a maximum, the slider acceleration is zero and the voltage and power generated are also zero. Figure 4.26 clearly shows that in order to optimize the power generation performance of the PDE-LPG facility, it is critical to reduce the dwell time of the piston at maximum displacement, and also reduce the response time of the spring to a compressive load.

The maximum displacement of the SDOF piston-slider spring system is recorded for varying fill-fraction in Figure 4.27. The displacement of the piston slider increases linearly with increasing fill-fraction. These displacement values are used to compute the spring work of the mechanical system. In this configuration, the measured spring work is negatively impacted by the energy transfer of the LPG slider into the stator which converted the slider motion into electromotive force generating a voltage. The peak and

RMS current and voltage generated by the LPG for varying fill-fraction are presented in Figure 4.28.

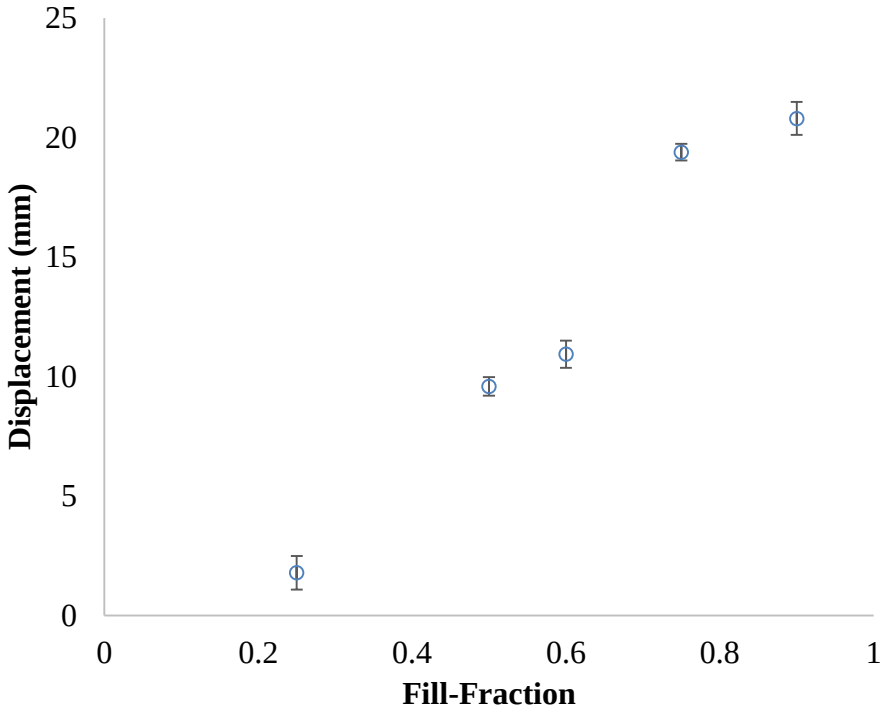

Figure 4.27 LPG slider displacement for varying fill-fraction.

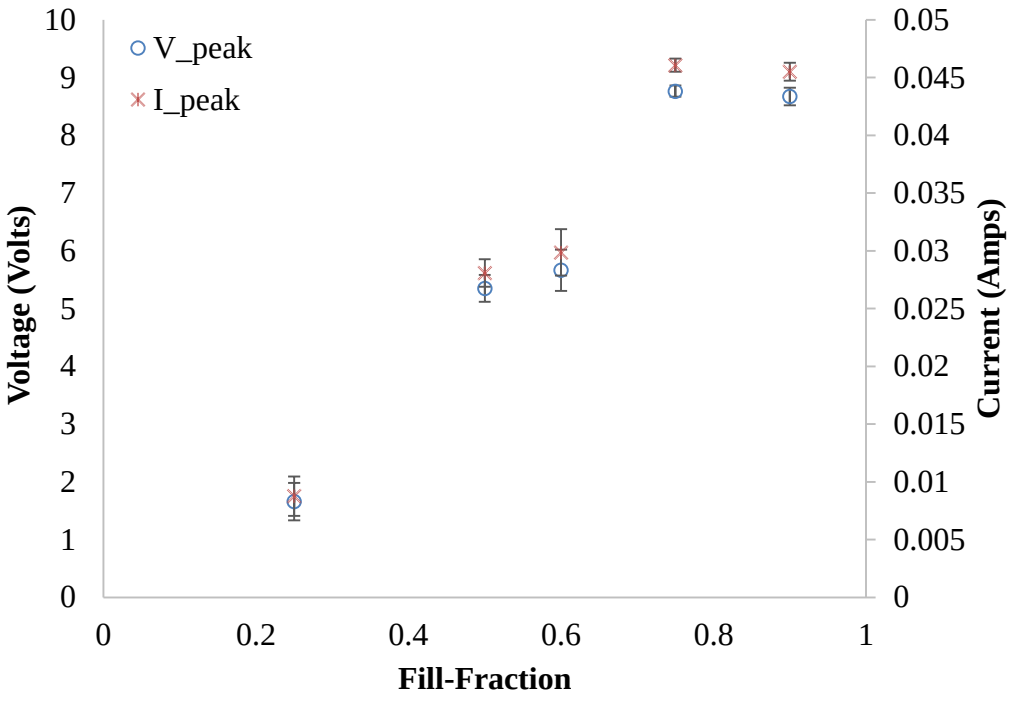

(a) Peak

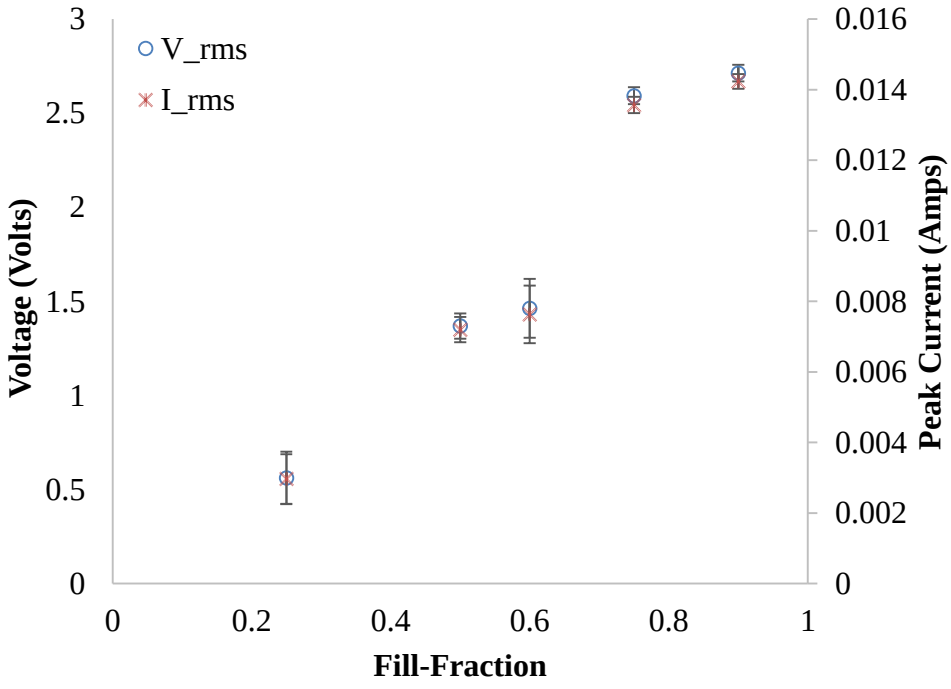

(b) RMS

Figure 4.28 LPG stator current and voltage for varying fill-fraction.

The RMS voltage and current are computed over the duration of the slider motion. For example, the RMS values for the 106% fill-fraction case shown in Figure 4.26 are computed from 0.35 to 0.46 s. The RMS voltage and current values correspond to the DC equivalent voltage and current.

The peak and RMS power generated by the LPG for varying fill-fraction are presented in Figure 4.29. Similar to the voltage and current peak and RMS values, the LPG power increased with increasing fill-fraction. Also, the RMS power is computed by averaging the power over the duration of slider motion. The RMS power corresponds to an equivalent DC circuit. The RMS power measured from the PDE-LPG facility is a few tens of mW. This equivalent DC power in this range is sufficient to power LEDs.

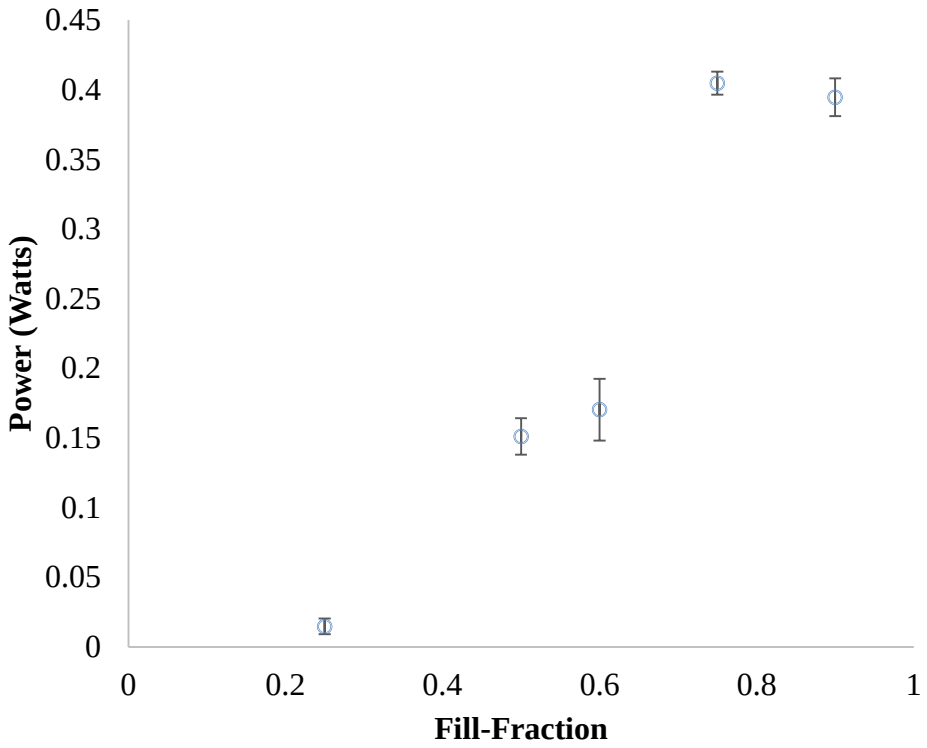

(a) Peak

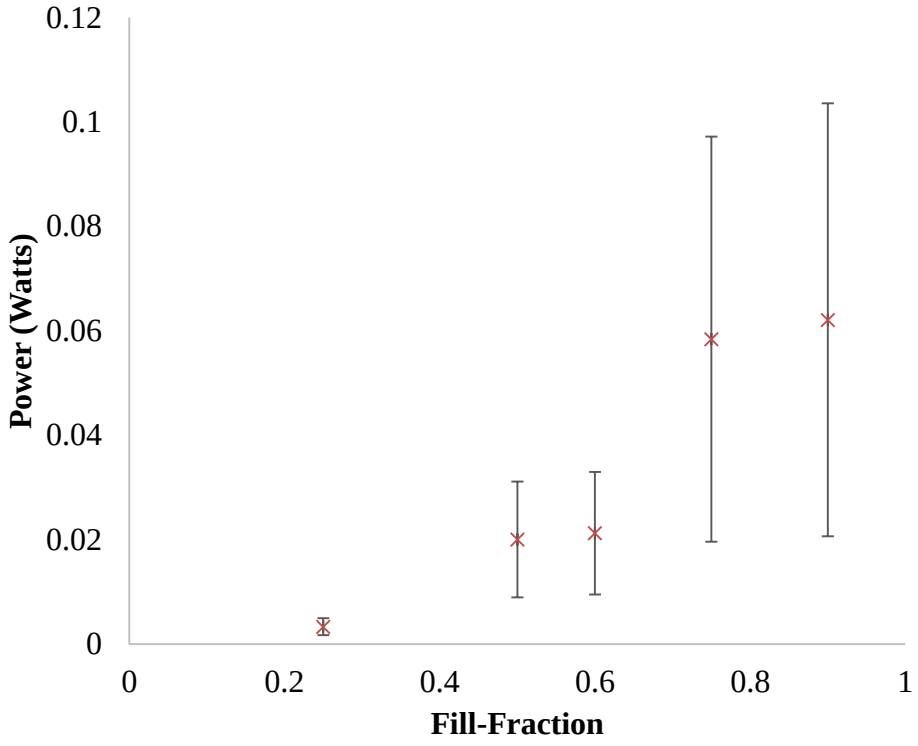

(b) RMS

Figure 4.29 LPG power for varying fill-fraction.

Qualitative power generation experiments are conducted with LEDs as the electrical load. The AC voltage generated is converted to DC voltage through a diode bridge which performed the physical equivalent of the mathematical RMS computation. All of the electrical current measurements for the PDE-LPG operation with varying fill-fraction are conducted with a constant load resistor of 175 Ω and a shunt resistor of 15 Ω.

The performance of the PDE-LPG facility is also examined for varying resistive electrical loads ranging from 47 to 505 Ω, while the PDE is operated at a constant fill-fraction of 75%. The peak displacements for the LPG slider with varying electrical loads are presented in Figure 4.30. The piston-slider displacement is relatively constant for the various electrical loads, and had an average value of 17.82 ± 0.55 mm. However, it can be

noted that the displacement of the LPG slider displacement decreased with increasing electrical load resistance. This decrease in LPG slider displacement can be attributed to the resistive load acting as a damper on the slider, through the LPG stator.

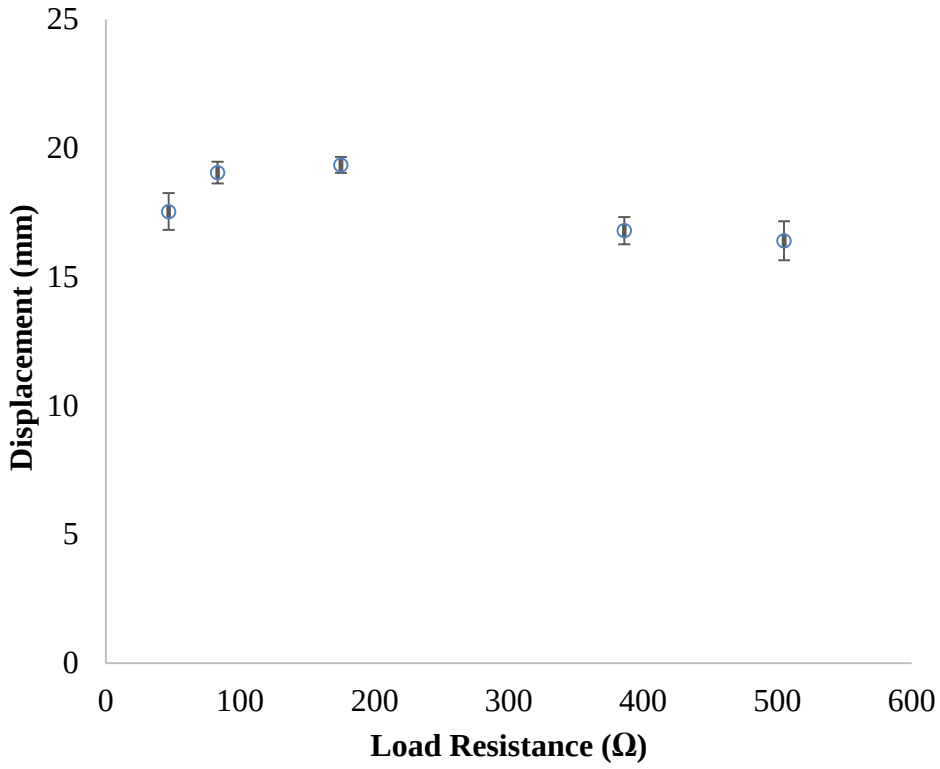

Figure 4.30 LPG slider displacement for varying electrical load.

The peak and RMS current and the voltage of LPG are measured for different resistive loads and at a constant fill-fraction of 75%, and are presented in Figure 4.31. The peak and RMS current decrease logarithmically with increasing load resistance, while the peak voltage is relatively constant over for the different electrical loads. However, the peak voltage drops significantly for the measurement at 47 Ω to an average value of 7.37 ± 0.48 V. The average voltage for the other four peak measurement for varying resistive load is 8.44 ± 0.20 V. The large error values for the voltage and current measurements at the low

load resistance value may be attributed to the decrease of the ratio of the shunt to load resistance.

The peak and RMS power are also calculated for difference load resistance at a constant fill-fraction of 75% and are shown in Figure 4.32. The peak and RMS power followed a logarithmic decreasing trend for increasing load resistance similarly to the peak and RMS current values. The maximum peak and RMS power occur at the low resistive load of 47Ω and were 0.885 ± 0.119 and 0.885 ± 0.119 W respectively.

In general, the electrical performance of the PDE-LPG can be improved by driving the slider at higher velocities, and ensuring that its oscillation to and from its nominal position is uniform. The LPG used in this work is also not powerful enough to harness the mechanical power transferred into the piston. The performance of the PDE-LPG can be further improved by matching the LPG power to the expected mechanical piston power.

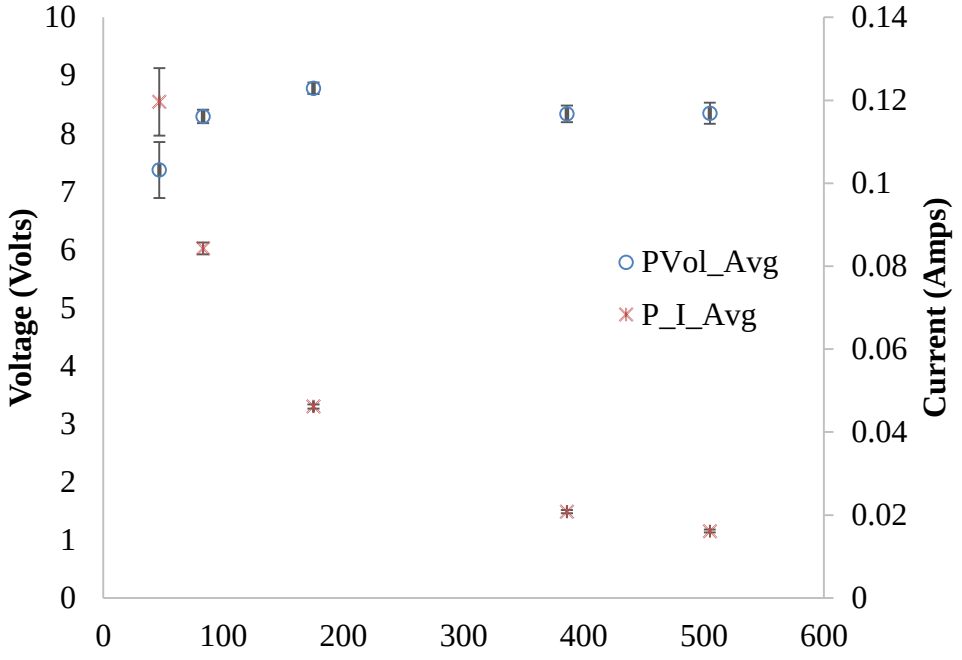

(a) Peak voltage and current

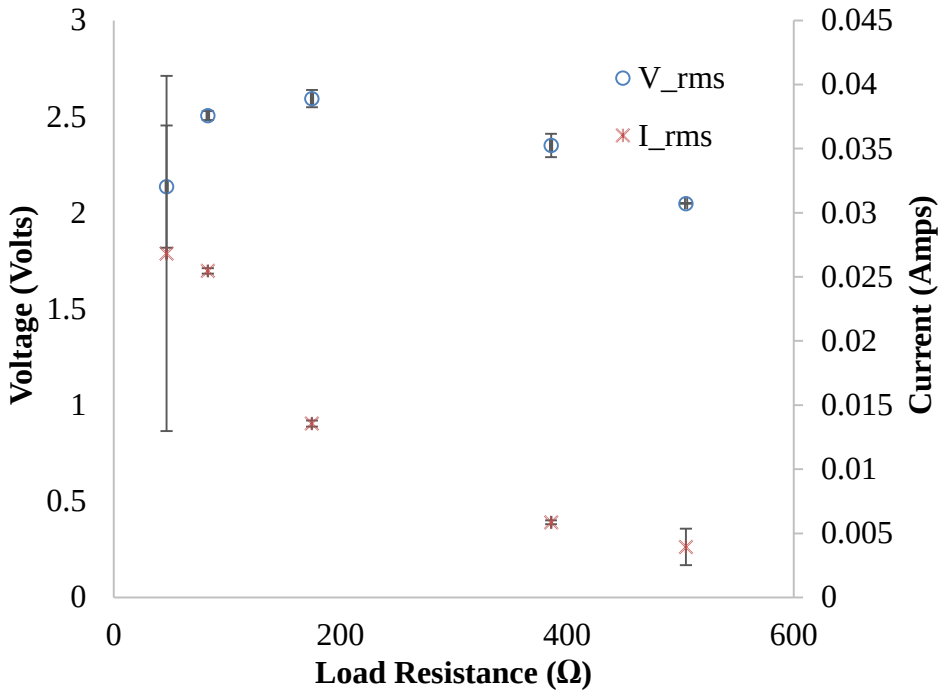

(b) RMS voltage and current

Figure 4.31 LPG stator current and voltage for varying electrical load.

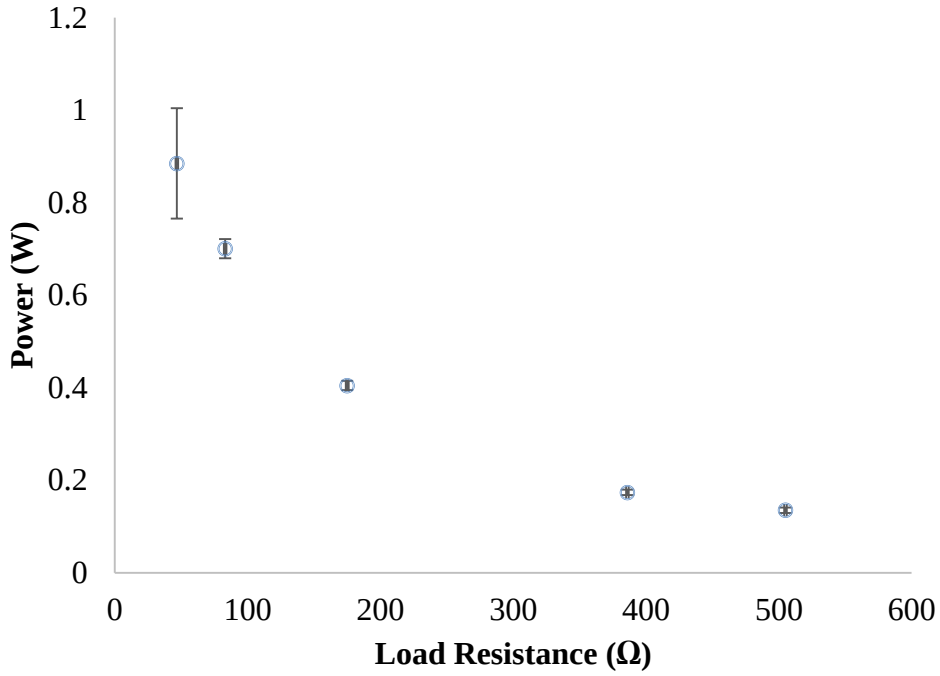

(a) Peak power

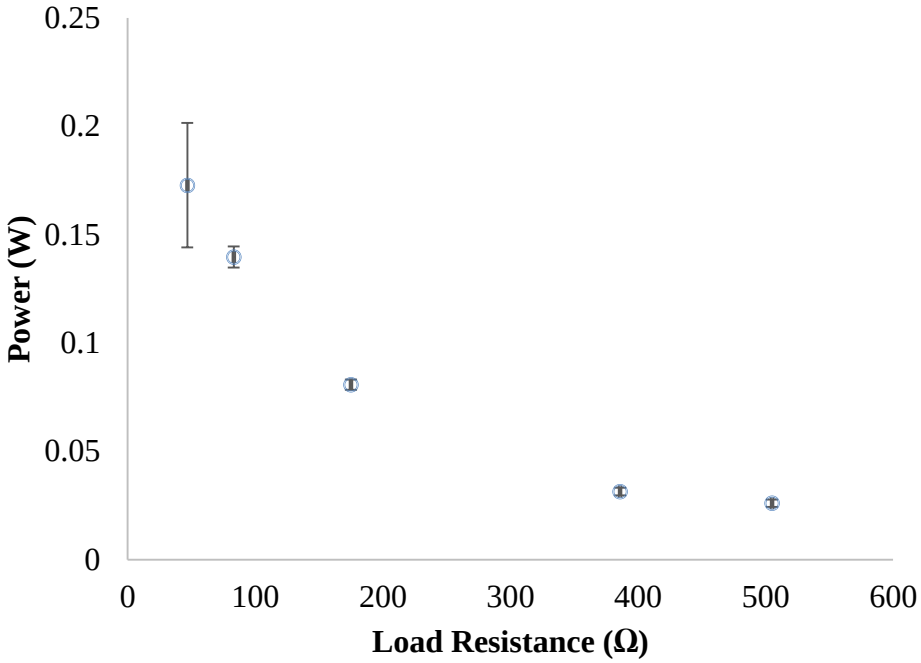

(b) RMS power

Figure 4.32 LPG power for varying electrical load.

4.2 Energy and Exergy Efficiencies

The energy and exergy values of the PDE-LPG facility are presented in this section, and are obtained from further analysis of the pressure displacement, current and voltage measurements presented above in section 4.1. Fuel energy and exergy values are obtained by relating the fuel lower heating value (LHV) and the fuel chemical exergy to the fuel mass flow rate into the engine. Table 4.1 below presents the fuel lower heating value, chemical exergy, and stoichiometric hydrogen fuel mass with the PDE tube fully-filled. The fully-filled mass corresponds to a fill-fraction of unity, and the fuel energy and exergy values for the varying fill-fraction are scaled by the fill-fraction values.

Table 4.1 Lower Heating Value (LHV), chemical exergy ξ_{ch}), and stoichiometric fuel mass (m_{fuel}) for fully-filled PDE tube

Fuel	LHV (mJ/mg)	ξ_{ch} (mJ/mg)	m_{fuel} (mg)
Hydrogen (g), H_2	119,703	116,436	18.27

The pressure work done by the PDE with nozzle on the piston is calculated from the stagnation pressure transducer measurements at the piston center and the linear displacement of the piston measured by the LVDT. The spring work is computed from the piston displacement data which also corresponds to the change in length of the compression spring, and with the spring constant predetermined through separate experiments presented in Chapter 3. The electrical energy per pulse is calculated from the numerical integration of the electrical power plots over the period of piston motion shown in Figure 4.26. The energy and exergy transferred across the various subsystems are then further analyzed in order to compute the energy and exergy efficiencies across each energy transfer and for the entire PDE-LPG facility. The standard deviations of the average measured values from the various measurements are propagated for the various equations for energy, exergy, and efficiencies.

4.2.1 Piston-Spring System

This section presents the performance of piston spring system relative to the pressure work input from the PDE with nozzle. This could only be examined in the facility configuration 3, because the pressure transducer port at the piston center is also used to couple the LPG slider in configuration 4. Therefore, this facility design does not allow for measurements of the stagnation pressure at the piston center and the LPG slider to be

coupled to the piston simultaneously. The pressure work and the spring work on the piston for varying PDE tube fill-fraction are presented in Figures 4.33 and 4.34 respectively.

The pressure work presented in Figure 4.33 is computed by multiplying the time and radially averaged pressure, with the 10 in. diameter piston area, and the maximum displacement from each fill-fraction operation. The time and radially averaged pressure are computed by averaging the peak pressure of the reflected shockwave on the piston face, and the ambient pressure present at the piston radial edge, over the over-pressure duration time. The pressure work generally increases with increasing fill-fraction for the PDE with nozzle, although the performance appeared to peak at a fill-fraction of 130% and decreases for a fill-fraction of 160%. Higher fill-fraction experiments are not conducted in order to prevent large piston displacements that would cause the piston to be dislodged from its linear traverse. The error values of the spring work are computed by applying the propagation of error for the measured values of pressure and displacement.

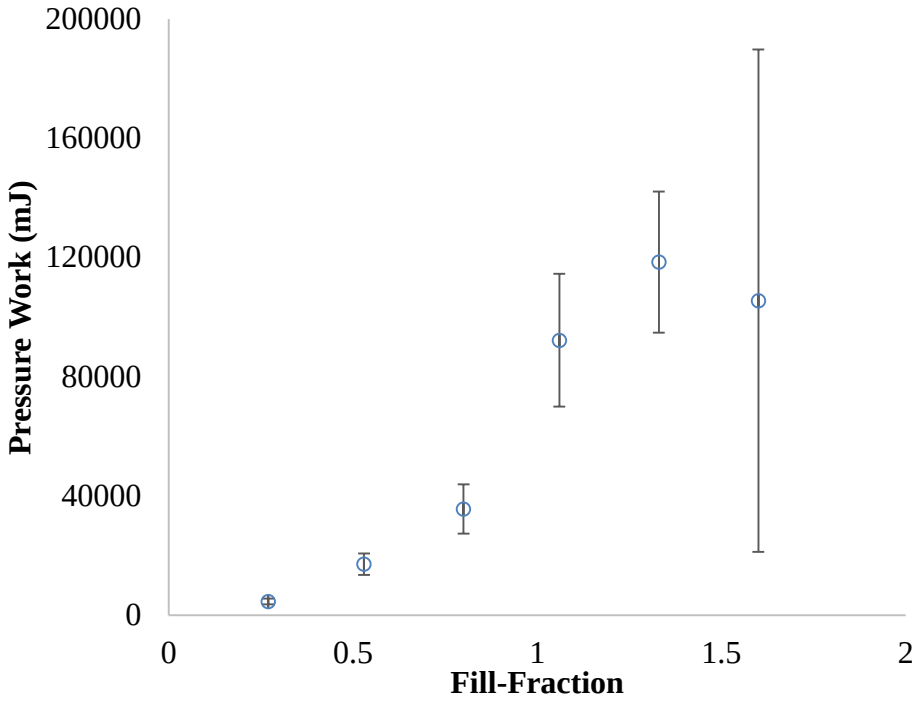

Figure 4.33 Pressure work for varying fill-fraction.

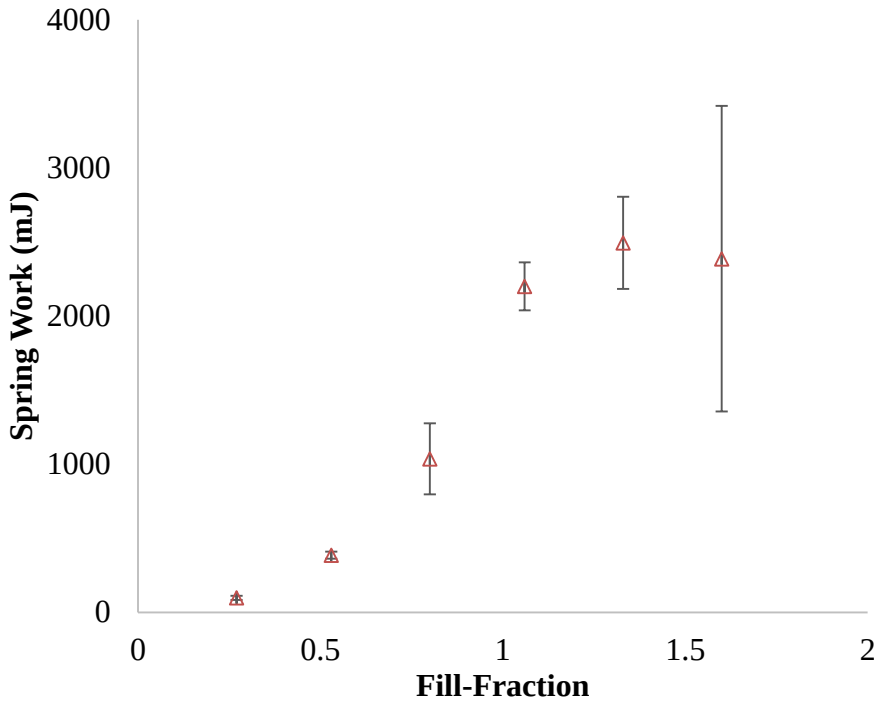

Figure 4.34 Spring work for varying fill-fraction.

The spring work presented in Figure 4.34 is computed by applying the simple Hooke's law equation for a SDOF system. The square of the maximum displacement values presented in Figure 4.21 are multiplied by the effective spring constants of the pair of spring that are in parallel and simply support the piston. The spring work generally increased with increasing fill-fraction. The error values of the spring work are computed from the propagation of error of the average displacement values.

The pressure work for equivalent fill-fractions is an order of magnitude higher relative to corresponding spring work values. This shows that the amount of energy that is reaching the piston as pressure work from the PDE with nozzle is being severely dissipated. The large dissipation could be due to poor confinement of the exhaust gases by the piston chamber, friction generated by the piston as it slid over the nozzle flange or the wave drag on the piston as it moves away from the nozzle flange at a high velocity. The difference in these energy values is reflected in Figure 4.35 which presents the efficiency of the pressure work to spring work $\eta_{II.SP}$.

This efficiency plot reveals that the performance of the piston in converting the pressure work from the PDE into spring work is invariant of the fill-fraction. Therefore, the inefficiencies of the piston-spring system scaled increasingly with fill-fraction, and reducing these inefficiencies would improve the operation of the piston-spring system irrespective of fill-fraction. The average pressure work to spring efficiency is $2.34 \pm 0.31\%$. The pressure work and spring work represented the work done by the PDE and the mechanical work done by the spring. Therefore the efficiencies presented in Figure 4.35 corresponded to the exergy efficiencies of the piston spring system, as they represent a

ratio of the work output in the spring to the maximum available work from the pressure of the PDE exhaust gases.

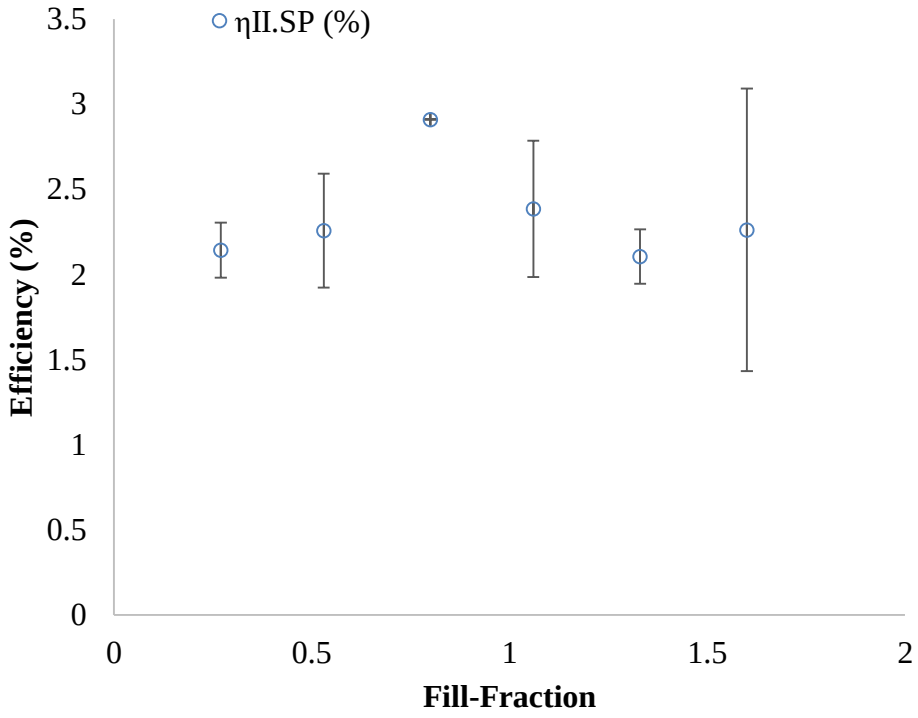

Figure 4.35 Efficiency of pressure work to spring work.

Figure 4.36 presents the energy and exergy efficiencies of the fuel energy to pressure work $\eta_{I.PF}$ and $\eta_{II.PF}$, which are the ratios of the pressure work to the fuel energy based on the lower heating value (LHV) and fuel exergy for equivalent fill-fraction. The plots shows that the fuel efficiency in generating pressure work increased linearly with fill-fraction in the partially-filled regime, is maximum at a fill-fraction of 1.33, and decreases for higher fill-fractions in the over-filled regime.

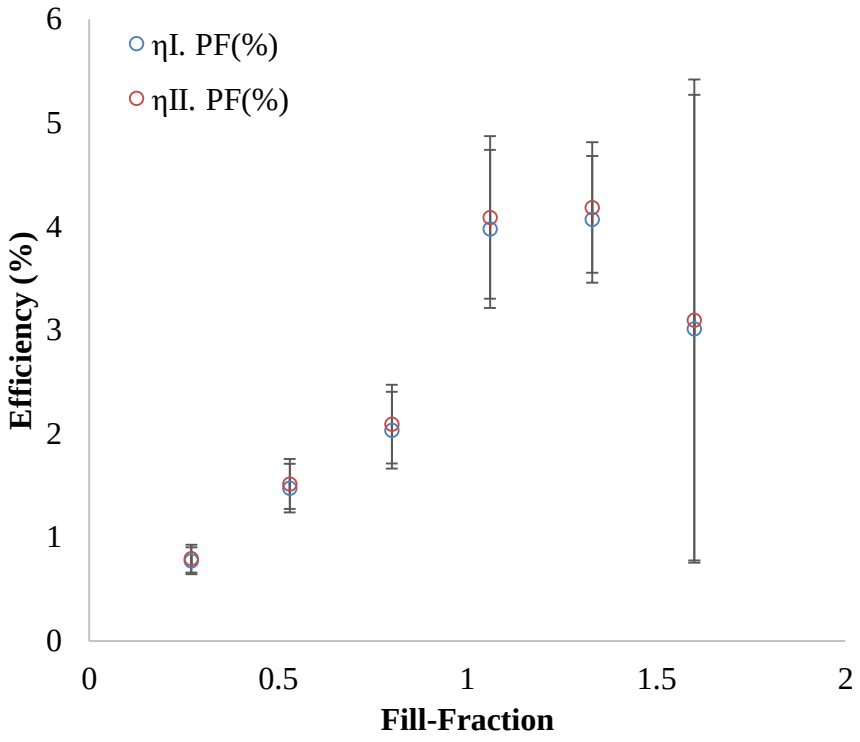

Figure 4.36 Energy and exergy efficiency of fuel energy to pressure work.

Figure 4.37 presents the energy and exergy efficiencies of the fuel energy to spring work $\eta_{I.SF}$ and $\eta_{II.SF}$, which are the ratios of the spring work to the fuel energy based on the lower heating value (LHV) and fuel exergy for equivalent fill-fraction. This plot reveals that the fuel efficiency of the facility in configuration 3 which consists of the PDE with nozzle, generally increases linearly with increasing fill-fraction in the partially-filled regime, is at a maximum for a fill-fraction of 1, and decreases linearly for fill-fractions in the over-filled regime. Comparing Figures 4.36 and 4.37 reveals that for optimally efficient piston pressure work generation, the facility should be operated in the slightly overfilled regime, while for optimally efficient spring work generation the facility should be operated fully-filled. However, since the primary goal in configuration 3 is the optimization of

spring work generation, it can be concluded that it is desired to operate the PDE with nozzle in the fully-filled condition.

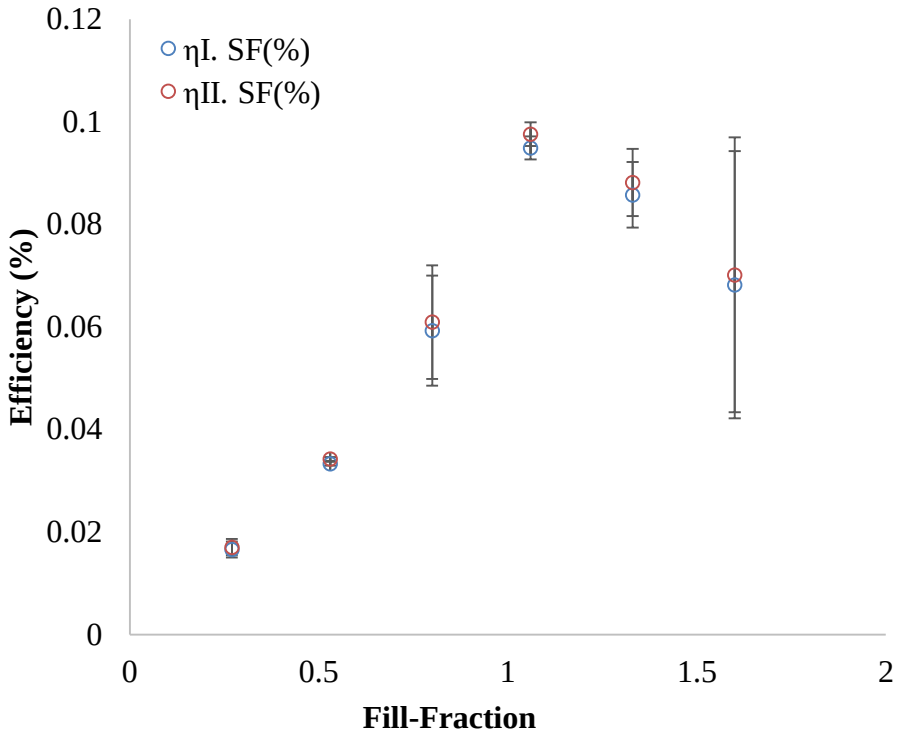

Figure 4.37 Energy and exergy efficiency of fuel energy to spring work.

4.2.2 PDE-LPG System with Varying Fill-fraction

This section presents the electrical performance of the PDE-LPG system relative to the spring work input from the piston for constant electrical load with varying fill-fraction in the partially-filled detonation tube operation regime. This performance is examined in configuration 4 described in Chapter 3, in the detailed experimental setup. The overall energy and exergy efficiencies for varying fill-fraction of the PDE-LPG facility are also presented here.

The spring work done by the piston-spring system and the electrical energy from the LPG for varying PDE tube fill-fraction are presented in Figures 4.38 and 4.39

respectively. The spring work presented in Figure 4.38 is computed similarly to the description presented in section 4.2.1. The measured displacement and the effective spring constant are used to compute the spring work. The spring work values generally increases linearly with increasing fill-fraction.

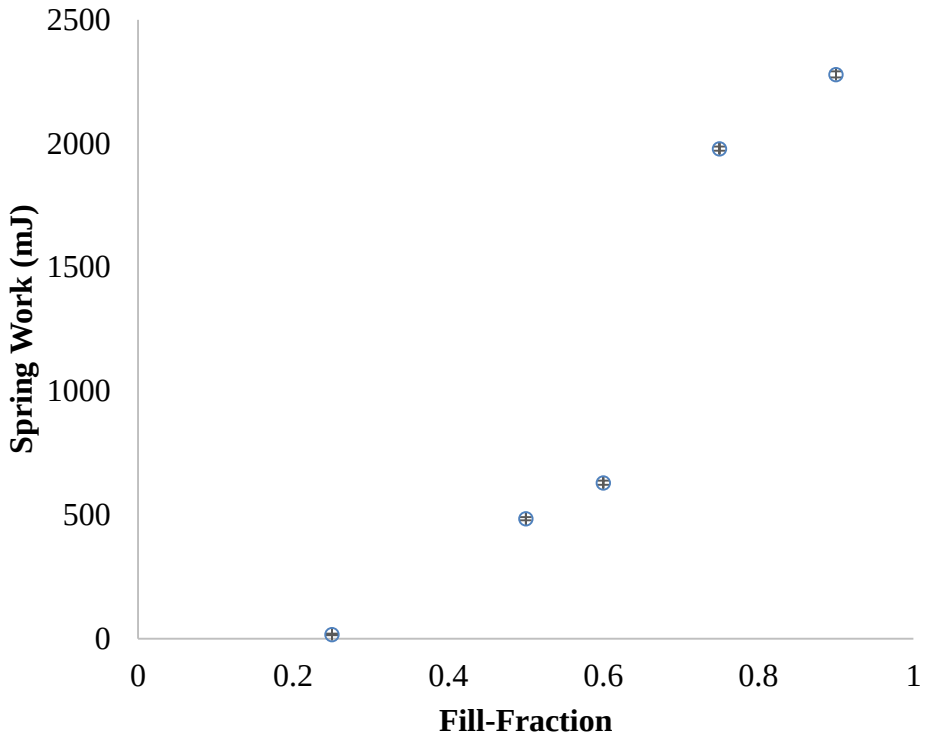

Figure 4.38 Spring work for varying fill-fraction

The electrical energy per pulse presented in Figure 4.39 is computed from the trapezoidal numerical integration of the time-varying electrical power over the period of the slider motion. The time varying electrical power is calculated from the product of the time-varying current and time-varying voltage measured from the LPG pair of terminals. These voltage and current measurements are conducted with a constant load resistance of 175 Ω, while the fill-fraction is varied. The electrical energy generally increases linearly for increasing PDE tube fill-fraction. The electrical energy represents the final desired

energy output of the PDE-LPG facility. The maximum energy of 4.50 ± 0.22 mJ is recorded at a fill-fraction of 90%. The electrical energy is about three orders of magnitude lower than spring work. This shows that the piston-spring system is strongly damped and that the LPG is highly inefficient in capturing the piston energy and converting it to electrical energy.

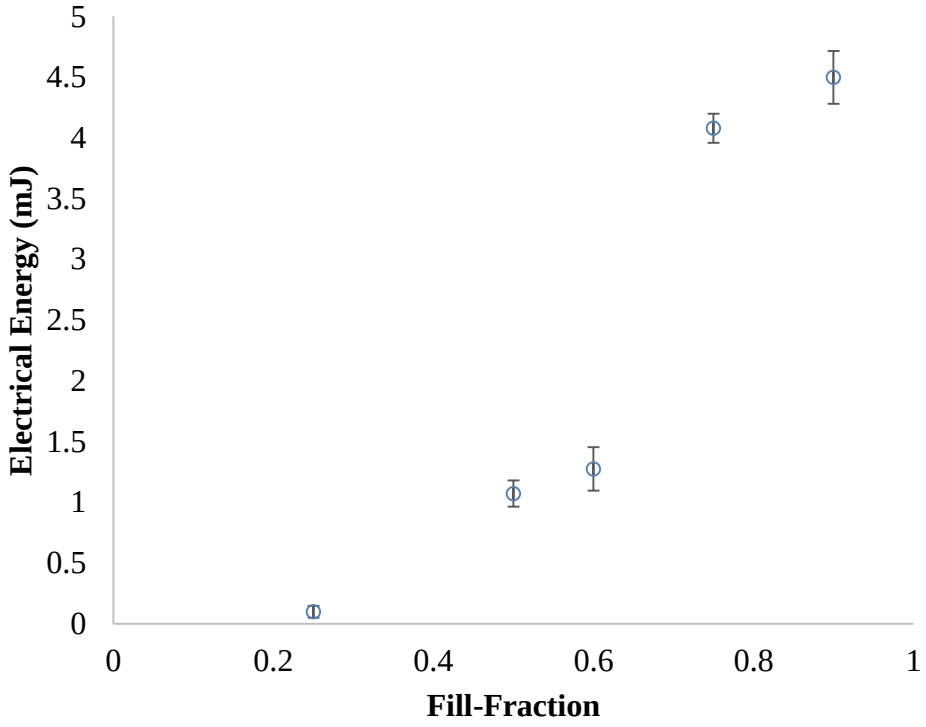

Figure 4.39 Electrical energy for varying fill-fraction.

The differences in these energy values are reflected in Figure 4.40 which presents the efficiency of the spring work to electrical energy $\eta_{II.ES}$ for varying fill-fraction. This efficiency plot reveals that the performance of the LPG in converting the spring work from the piston into electrical energy is relatively constant for fill-fractions greater than 50% with an average value of 0.21 ± 0.01 %. The efficiency effectively triples for a fill-fraction of 25% to a value of 0.585 ± 0.016 %. Therefore, it appears that for optimal electrical

energy generation, a low fill-fraction is desired. The spring work and electrical energy represented the mechanical work done by the spring and the electrical energy from the LPG. Therefore the efficiencies presented in Figure 4.40 corresponds to the exergy efficiencies of the piston-spring LPG system, as they represent a ratio of the work output from the LPG to the maximum available work from the motion of the piston-spring system.

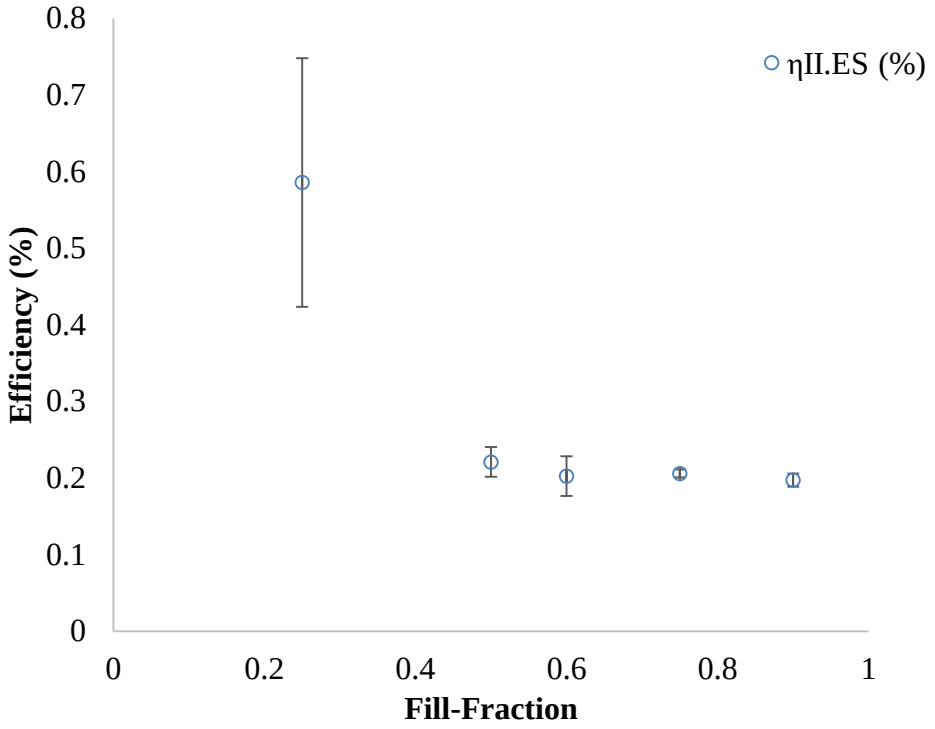

Figure 4.40 Efficiency of spring to electrical energy for varying fill-fraction.

Figure 4.41 presents the energy and exergy efficiencies of the fuel energy to spring work $\eta_{I.SF}$ and $\eta_{II.SF}$, which are the ratios of the spring work to the fuel energy based on the lower heating value (LHV) and fuel exergy for equivalent fill-fraction. In contrast to Figure 4.37 which also presents the fuel energy to spring work efficiencies and the values presented in Figure 4.41 are measured in configuration four that includes energy extraction by the LPG. The plot shows that the fuel efficiency in generating spring work increased

linearly with fill-fraction in the partially-filled regime, and reaches a maximum at a fill-fraction of 75%.

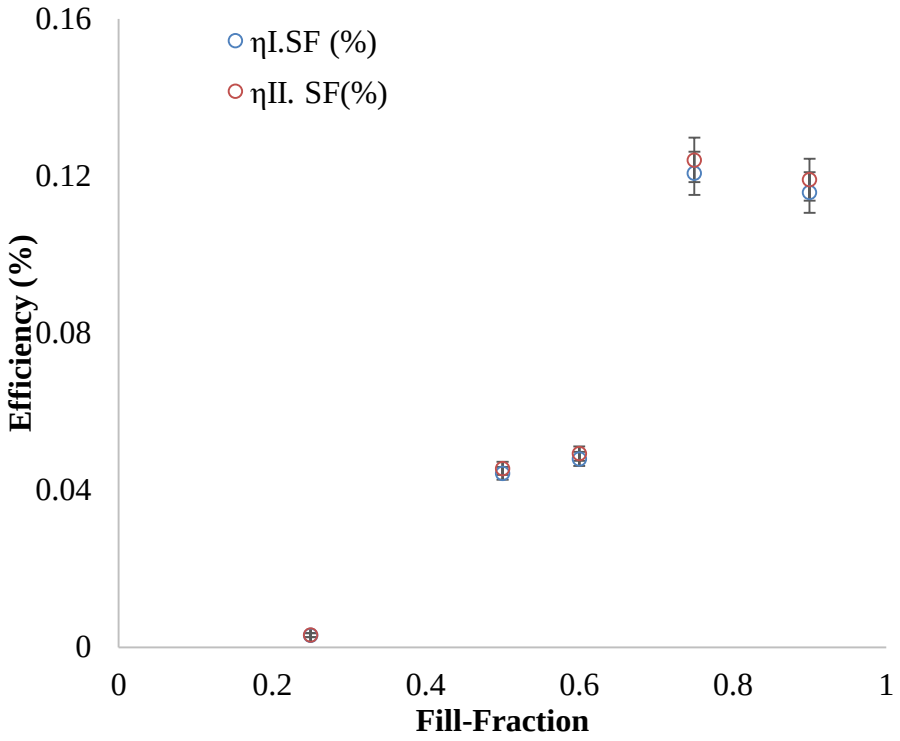

Figure 4.41 Energy and exergy efficiency of fuel energy to spring work for varying fill-fraction.

Figure 4.42 presents the energy and exergy efficiencies of the fuel energy to electrical energy $\eta_{I.EF}$ and $\eta_{II.EF}$, which are the ratios of the electrical energy to the fuel energy based on the lower heating value (LHV) and fuel exergy for equivalent fill-fraction. The plot shows that the fuel energy and exergy efficiency in generating electrical energy increased linearly with fill-fraction in the partially-filled regime, and reaches a maximum at a fill-fraction of 75% with a value of 0.000249 ± 0. 000005 % and 0.000255 ± 0.00004 % respectively. These values represent the overall energy and exergy efficiencies of the PDE LPG facility in converting fuel energy to electrical energy for varying fill-fraction.

These extremely low fuel-to-electrical efficiencies are expected because of the power mismatch between the 2 kW PDE and 5 W LPG for 1 Hz operation, presented in the LPG calibration data discussed in Chapter 3.

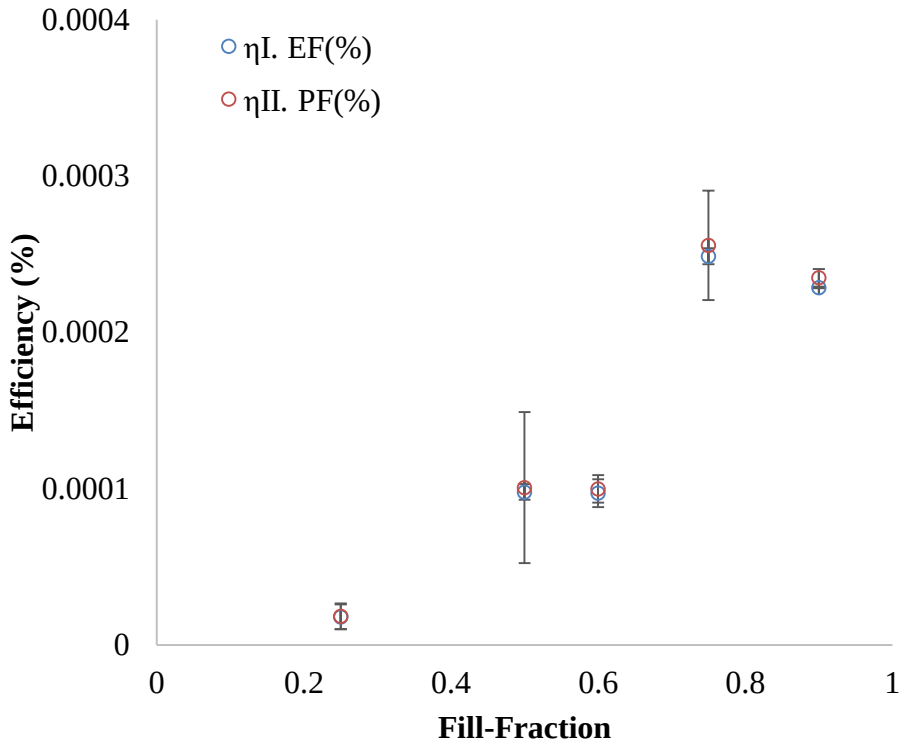

Figure 4.42 Energy and exergy efficiency of fuel energy to electrical energy for varying fill-fraction.

4.2.3 PDE-LPG System with Varying Resistive Loads

This section presents the electrical performance of the PDE-LPG system relative to the spring work input from the piston, for varying electrical load with a constant fill-fraction of 75% in the partially-filled detonation tube operation regime. Similar to section 4.2.2 these results are obtained in facility configuration 4 described in the experimental setup of Chapter 3. The overall energy and exergy efficiencies for varying electrical loads of the PDE-LPG facility are also presented here.

The spring work done by the piston-spring system and the electrical energy from the LPG for varying PDE tube fill-fraction are presented in Figures 4.43 and 4.44 respectively. The spring work presented in Figure 4.43 is computed similarly to the description presented in section 4.2.1. The measured displacement and the effective spring constant are used to compute the spring work. The spring work values appear to peak at a load resistor value of 175 Ω. A decrease in spring work is more notable for large resistor values. This may be due to the LPG electrical circuit acting as a motion damper to the LPG slider whose displacement is directly related to the spring displacement. The variation of the spring work due to load resistance was not significantly large as all the experiments are conducted at a constant fill-fraction of 75%.

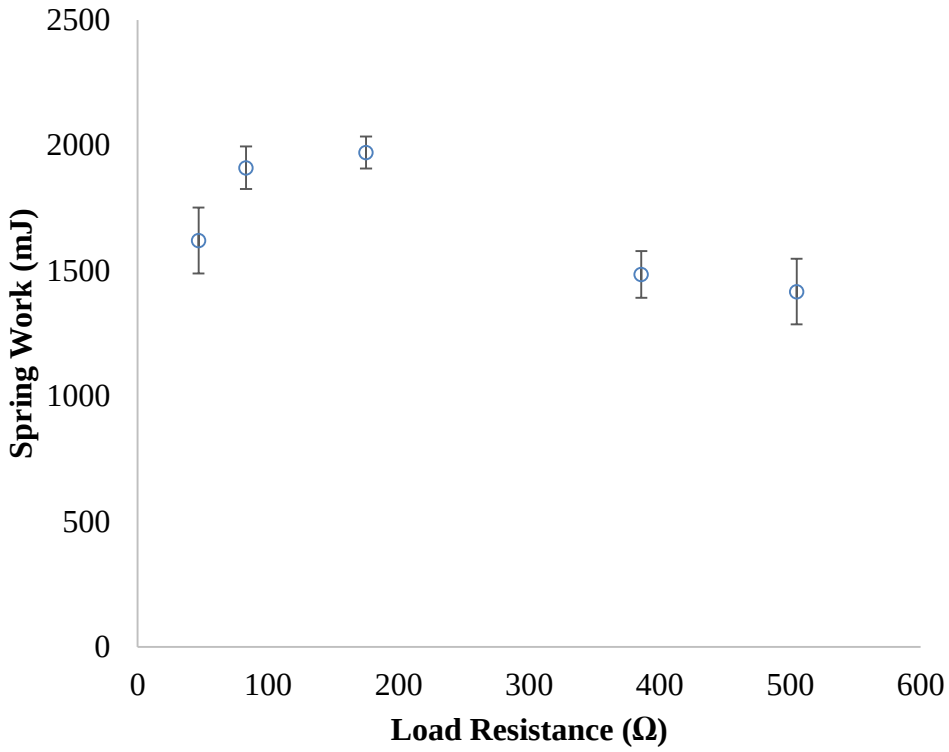

Figure 4.43 Spring work for varying resistive load.

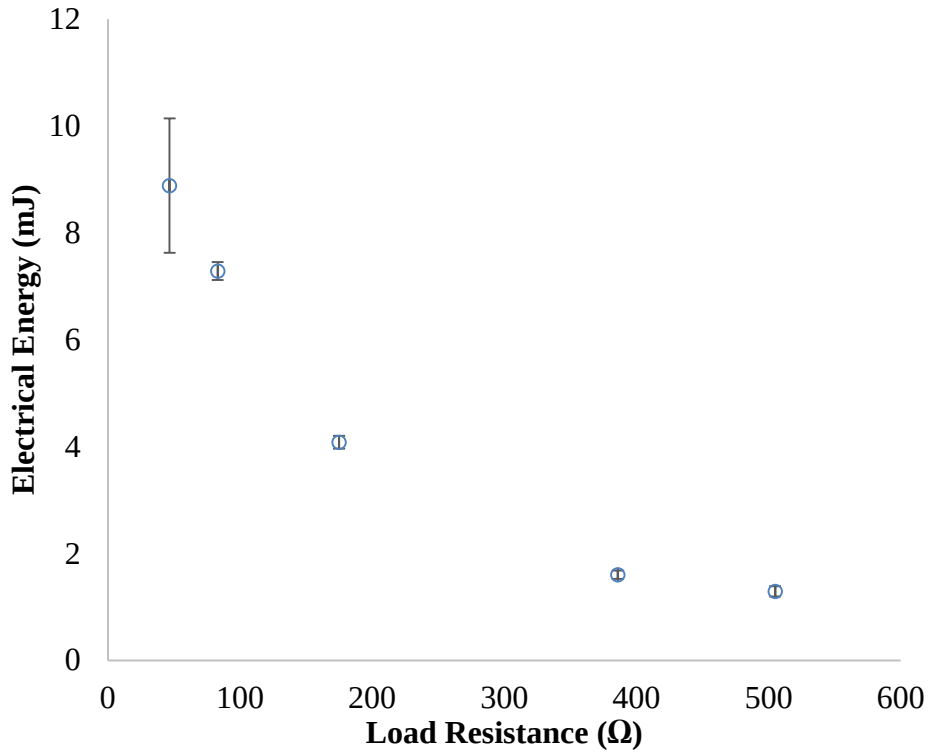

Figure 4.44 Electrical energy for varying resistive load.

Similarly to the electrical energy per pulse presented in Figure 4.39 for varying fill-fraction, the electrical energy is presented in Figure 4.44 for varying resistive load, and is obtained from the trapezoidal numerical integration of the time varying electrical power over the period of the slider motion. The electrical power is calculated from the product of the time varying current and time varying voltage measured from the LPG pair of terminals. These voltage and current measurements are conducted with load resistance ranging from 47 to 505 Ω while the fill-fraction is held constant at 75%. The electrical energy decreases logarithmically with increasing load resistance. The electrical energy represents the final desired energy output of the PDE-LPG facility. The maximum energy of 8.88 ± 1.26 mJ is recorded at a resistive load 47 Ω. The electrical energy output is about three orders of magnitude lower than spring work input.

The differences in these energy values are reflected in Figure 4.45 which presents the efficiency of the spring work to electrical energy $\eta_{II.ES}$, for varying resistive loads. This efficiency plot reveals that the performance of the LPG in converting the spring work from the piston into electrical energy increased logarithmically with decreasing resistive loads with a peak value of 0.548 ± 0.033 mJ at the load resistance of 47 Ω. Therefore, it appears that for optimal electrical energy generation, a low load resistance is desired. The spring work and electrical energy represent the mechanical work done by the spring and the electrical energy from the LPG. Hence, the efficiencies presented in Figure 4.45 corresponds to the exergy efficiencies of the piston-spring LPG system for varying resistive loads.

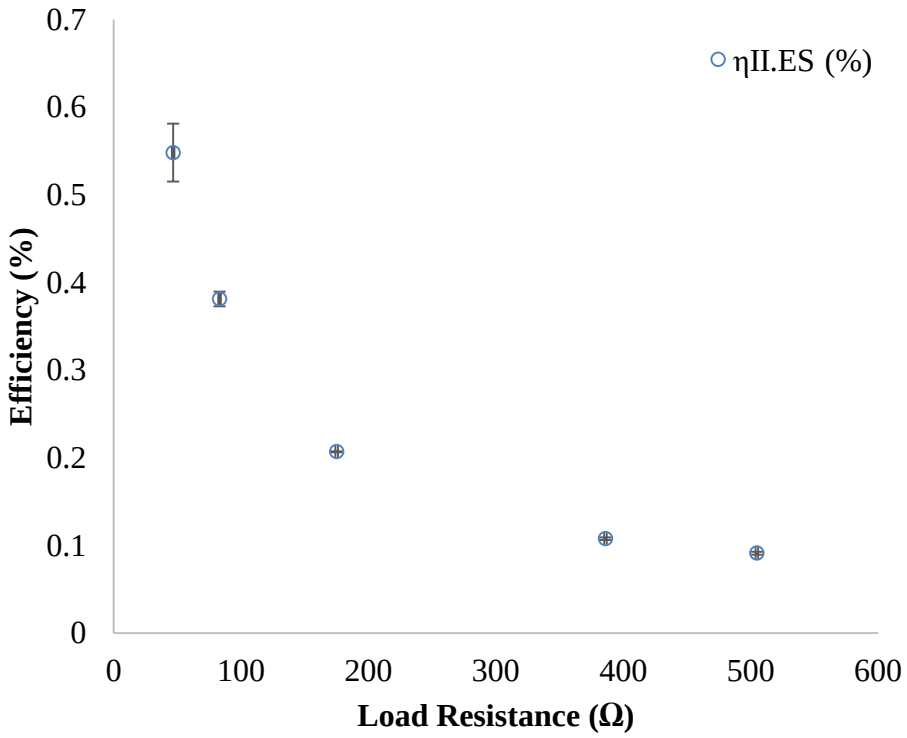

Figure 4.45 Efficiency of spring to electrical energy for varying resistive load.

Figure 4.46 presents the energy and exergy efficiencies of the fuel energy to spring work, which are the ratios of the spring work to the fuel energy based on the lower heating value (LHV) and fuel exergy for a constant fill-fraction of 75%. In contrast to Figure 4.41 which also presents the fuel energy to spring work efficiencies for varying fill-fraction, the values in Figure 4.46 are presented for varying load resistor. Therefore, the damping effect of the LPG circuit can be seen for higher load resistance. The plot shows that the fuel efficiency in generating spring work followed a similar trend as described for the measured spring work shown in Figure 4.43.

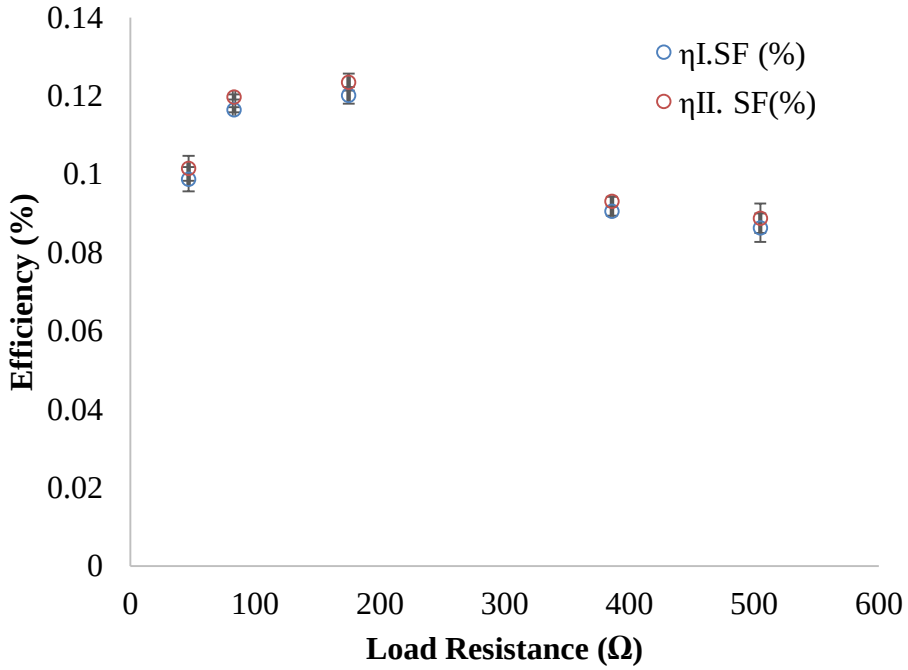

Figure 4.46 Energy and exergy efficiency of fuel energy to spring work for varying resistive load.

Figure 4.47 presents the energy and exergy efficiencies of the fuel energy to electrical energy, which are the ratios of the electrical energy to the fuel energy based on the lower heating value (LHV) and fuel exergy for a constant fill-fraction of 75%. The plot

shows that the fuel efficiency in generating electrical energy followed a similar trend as described for the measured electrical energy shown in Figure 4.44. The maximum facility fuel-to-electrical energy and exergy efficiency occur at 47 Ω with values of 0.000542 ± 0.00005% and 0.000557 ± 0.00005 % respectively. These values represent the overall energy and exergy efficiencies of the PDE-LPG facility in converting fuel energy to electrical energy for varying electrical load.

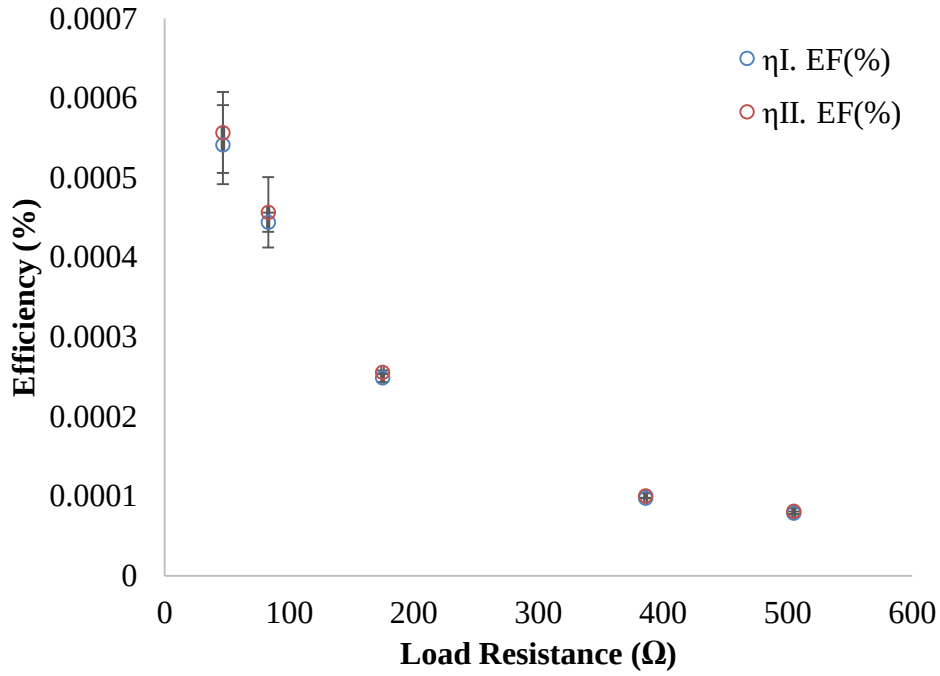

Figure 4.47 Energy and exergy efficiency of fuel energy to electrical energy for varying resistive load.

The energy and exergy efficiency values presented in this section indicate that the PDE-LPG facility still requires a lot of development in order to be an economically practical device for power generation. However, this section has presented a systematic method for examining the energy and exergy efficiencies for a system coupled with chemical, thermal, mechanical, and electrical subsystems.

CHAPTER 5

Conclusions and Future Work

A methodology for the characterization of the energy and exergy efficiencies of the PDE for power generation is studied with the development of a pulse detonation engine linear power generator (PDE-LPG) system. A one-dimensional model for the performance of a PDE for fully- and partially-filled operation was presented. The fully-filled PDE produces a simple wave diagram characterized by a detonation wave, Taylor rarefaction, and exhausting rarefaction. The partially-filled PDE produces a complex wave pattern that includes the detonation wave, Taylor rarefaction, incident shockwave, incident rarefaction, contact surface, exhausting rarefaction and several rarefaction reflections. The thrust wall pressure profiles for the fully- and partially-filled PDE are presented.

A new thermodynamic cycle referred to as the "PDE-LPG cycle" is proposed and developed for the general study of a pulse detonation engine configured with a piston at the typically open end of a PDE tube. The energy and exergy efficiency of the PDE-LPG cycle for a detonation engine is compared to the efficiencies of the Brayton, Otto, Diesel, and ZND cycles relative to the thermal efficiency of the ideal Carnot cycle for methane-air powered heat engines.

Detonation engines use a supersonic combustion process which holds promise for the development of higher power density generators over deflagration combustion generators. The PDE-LPG cycle models the detonation engine similarly to the ZND cycle as they both incorporate the supersonic flow processes of shock compression, and Rayleigh heat addition. However, a simplified pulse detonation turbine engine generator can be modeled by the ZND cycle which rejects heat through an isobaric process, while the piston

configuration of the PDE-LPG facility forces the system to reject heat through an isochoric process, and therefore requires the development of a novel thermodynamic cycle to describe the system performance.

For the PDE-LPG cycle, higher thermal efficiencies can be achieved for higher equivalent turbine inlet temperatures, but this generally decreases the second law efficiency for equivalent pressure ratio. Comparison of the engine cycles shows that for equivalent pressure ratios, the PDE-LPG cycle for a detonation engine produced superior thermal efficiency than the Brayton, Otto, and Diesel cycle heat engines, but performs about a maximum of 3% lower in efficiency compared to the ZND cycle while following a similar trend. However superior exergy efficiency of the PDE-LPG cycle than the Brayton cycle is limited to a CPR of 20.

A mobile PDE-LPG system is designed and developed to measure the system energy and exergy efficiency, while accounting for the chemical exergy, pressure work, mechanical work, and electrical energy transfers. This system incorporates a gas cart, a PDE, a diverging nozzle, a piston-spring resonator, and a LPG. The important parameters such as the spring constant and performance of the LPG system are independently characterized. The available LPG system is not sufficient to efficiently produce electricity from the PDE. Therefore the primary focus of this work is demonstrating the performance improvements of the developed techniques and a methodology for analyzing the system energy and exergy performance.

Experimental data collected from the PDE-LPG system are presented. These include the detonation pressure profiles along the PDE, the nozzle exhaust flow expansion performance, the thrust and specific impulse of the PDE with and without a nozzle, the

sound level from PDE exhaust, the effect of partial-filling on the piston-spring system displacement response, and the electrical voltage, current, and power generated by the PDE-LPG system for varying fill-fractions and varying resistive electrical loads.

Finally, these measurements are further analyzed to compute the chemical, thermal, mechanical, and electrical energy and exergy values for varying fill fractions and varying electrical loads. Overall the system efficiency values are very low due to the design decisions of operating with a non-airtight piston system, and the mismatch of the power output capability of the LPG. However, a key insight which is discovered from this experimental study, is that the piston-spring subsystem pressure work input to spring work output average efficiency of 2.34 ± 0.31%, is invariant of the fill fraction. Therefore, efficiency improvements of the thermomechanical energy conversion piston-spring subsystem of the PDE-LPG can be developed independently of the PDE, with a system which produces a similarly pulsed pressure input.

The experimental setup developed in this work demonstrated the repeatable operation of a PDE with one end closed by the thrust wall, and the other commonly open end confined by a piston. This presents the potential for the future development of a PDE piston system operating at a high fuel and oxidizer pre-compression ratio, in contrast to the current state-of-the-art PDEs which typically operate without pre-compression. The future development of an airtight piston system will also drastically improve the work output of the PDE-LPG system. This piston system could also be configured with a rotary crankshaft system, as long as the piston top dead center position is designed to not coincide with the impact of the detonation wave, preventing the transfer of infinite jerk to the crankshaft.

A key challenge of the developed PDE-LPG system is the low specific impulse improvement of the diverging nozzle on the PDE performance. This lies within the fact that the nozzle is designed for steady flow, while the nature of PDE flow is intrinsically dynamic. Similarly, to how the PDE-LPG couples the dynamic PDE with a dynamic LPG in an attempt to produce power more efficiently. Future developments can involve the design of a dynamic nozzle capable of changing its area ratio to match the exhaust pressure, therefore preventing over-expansion, and operating with a response time on the timescales of detonation wave propagation.

APPENDIX A

Fill-Fraction Wave Diagram MATLAB® Program

The MATLAB® program below was developed for the one-dimensional analysis of PDE performance for partially and fully-filled PDE.

```
%% Raheem Bello
%% Wave-Diagram for Partially Filled PDE

% plot graph in x-t space reflecting all the wave patterns present in a
% PF-PDE of stoichiometric H2-O2 detonable mixture with inert air. The tube
% length is considered to be 1m, and 50% of the tube is partially filled.
clc; clear;
%% Incident detonation wave
% The CJ velocity for H2-O2 phi=1 detonable mixture is ~2800m/s
uCJ=2835.7; xhalf=0.5;%% Fill-fraction
l=40; xend=1;  x_Idw=linspace(0,xhalf, l);
t_Idw=x_Idw*1000/uCJ;
%Detonation Parameters from cea for p1=1atm T=300K phi=1
MCJ= 5.2562; % detonation Mach number
PCJ_0=18.657; %P3/P0
T3_0=12.253; %T3/T0
TCJ= 3675.81; % K
aCJ= 1542.5; %sonic velocity m/s
g3= 1.1288; %gamma3
g3R= aCJ^2/TCJ; % gamma3 * R

P0=101325; g0=1.4014; PCJ=PCJ_0*101325;  % from cea
ki=(g3+1)/(2*g3); kii=(g3-1)/(2*g3); kiii=ki/kii; %from Endo
p3w=(ki^kiii/2)*(g0/g3)*MCJ^2*P0; %from endo

pcj= P0*PCJ_0; P3w_CJ= p3w/PCJ;
t_CJ= t_Idw(l);

plot(x_Idw, t_Idw/t_CJ,'k','LineWidth',4);
xlabel('\bf l / l_t_u_b_e');ylabel('\bf t / t_C_J ');

%title('\bf Wave Diagram of Partially filled PDE');
hold on;
%% Taylor Expansion behind det. wave
a3= (aCJ^2* (P3w_CJ)^((g3-1)/g3) )^.5;
u3=0; u_TE= a3-u3; % The expansion waves are mach waves
x_TE=linspace(0,.5*(1-xhalf)+xhalf, l); %TaylorWave to CS
t_TE= x_TE*1000/u_TE;
plot(x_TE, t_TE/t_CJ,'r--','LineWidth',2);        hold on;

%% Reflection of Taylor Expansion (Rarefaction Wave) at gas interface
```

```
%simple region assumption mach wave1=-1/a3;
u3=0; u_RTE= -a3+u3; % The expansion waves are mach waves
t_RTE= (x_Idw-x_Idw(l))*1000/u_RTE   + t_Idw(l);
plot(x_Idw, t_RTE/t_CJ,'r.','LineWidth',2);        hold on;



%% Transmission of ShockWave in inert region
P3_1=PCJ_0; P1=P0; %since p0=p1=1atm
c1=347.2; g1=1.4;  %speed of sound in air at 300K
c1_CJ= c1/aCJ;
%Reiman Problem with c1=/=c3 and g1=/=g3
%P3_1=P2_1* (1-c1_3*(g3-1)*(P2_1-1)/(2*g1*((g1+1)*P2_1+(g1-1)))^.5)^(-2*g3/(g3-
1));
syms Px Mx %Px= P2_1
P21= solve(Px* (1-c1_CJ*(g3-1)*(Px-1)/(2*g1*((g1+1)*Px+(g1-1)))^.5)^(-2*g3/(g3-
1))==P3_1);
P2_1= double(P21); P2=P2_1*P1;
Msx=solve((2*g1*Mx^2)/(g1+1)-(g1-1)/(g1+1)==P2_1); %Normal shock Rel.
Ms=double(Msx(1));  %Mach 3.0184

u_Ms = Ms*c1;  a2=555.4; g2=1.3543;  %m/s from cea
x_Ts=linspace(xhalf,xend, l);

t_Ts= (x_Ts-xhalf)*1000/u_Ms + t_Idw(l) ;
plot(x_Ts, t_Ts/t_CJ,'k--','LineWidth',2);        hold on;
%% Second expansion wave to define region 4
u2= c1*(P2_1 - 1) *(2/(g1*( (g1+1)*P2_1+(g1-1) ) ))^.5;
P2_3= P2_1/P3_1;  P4_3=P2_3; % pressure in region 2 and 4 are equal.
u4= 2*a3/(g3-1)*(1-P4_3^((g3-1)/(2*g3)));
% Hence the computed value for u2 and u4 are equal
%Md= %Molar mass of burned mixed.
Rg= 8.3145; % molar gas constant
%a4=(g3*Rg*T4/ Md)^.5
a4= (a3^2* (P4_3)^((g3-1)/g3) )^.5;         % u4=u2;
%% Second expansion wave to define region 4
 u_RTE2= -a4+u4; % The expansion waves are mach waves

%% Interface betweeen burned det. gas and inert gas
t_IDI= (x_Ts-xhalf)*1000/u4 + t_Idw(l) ;
plot(x_Ts, t_IDI/t_CJ,'b:','LineWidth',2);   hold on;

%% Strong expansion due to %shock exit
u_SE=  u_RTE2;      x_SE= linspace(0,xend, 2*l);
```

```
t_SE= (x_SE- xend)*1000/ u_SE  + t_Ts(l);
plot(x_SE,  t_SE/t_CJ,'r.-','LineWidth',2);        hold on;

%% Second expansion wave to define region 4 -%second%
 u_RTE2= -a4+u4; % The expansion waves are mach waves
t_RTE2= (x_Idw-x_Idw(l))*1000/u_RTE2   + t_Idw(l);
plot(x_Idw, t_RTE2/t_CJ,'r.','LineWidth',2);       hold on;


%% Reflection of Rarefaction Wave at Thrust Wall
% J1p= 2*a3/(g3-1); J2p=J1p; J2m= u4-2*a4/(g3-1);  %MOC
x_RRW= linspace(0,xend, 2*l); u_RRW=a4+u4;
t_RRW= (x_RRW)*1000/ u_RRW  + t_RTE(1);
%plot(x_RRW, t_RRW/t_CJ,'b--','LineWidth',2);        hold on;

%% Conditions above Reflected  Rarefaction MOC
a5=a4-(g3-1)*u4/2;         u_RRW2=a5+u4;

t_RRW2= (x_RRW)*1000/ u_RRW2  + t_RTE2(1);
%plot(x_RRW, t_RRW2/t_CJ,'b--','LineWidth',2);        hold on;
P5= p3w*(a5/a3)^(2*g3/(g3-1));

legend('Detonation wave','Taylor Rarefaction','Interface Rarefaction','Shock
wave','Contact Surface','Exhaust Rarefaction');

%% Transmission an reflection of Expansion wave into inert gas
% Not considered since these are weak mach waves


%% Reflection of Rarefaction Wave  from the shock wave
% critical since this weakens the shock


% reflection off contact surface
xe_CS=x_TE(l);   x_CS= linspace(0,xe_CS, 2*l);
t_CS= (x_CS- xe_CS)*1000/ u_SE  + t_TE(l);
plot(x_CS,  t_CS/t_CJ,'r--','LineWidth',2);        hold on;


P6=P0;      P6_5=P6/P5;
a6= (a5^2* (P6_5)^((g3-1)/g3) )^.5;
u_SE2= -a6+2.7*c1;%
t_SE2= (x_SE- xend)*1000/ u_SE2  + t_Ts(l);
plot(x_SE,  t_SE2/t_CJ,'r.-','LineWidth',2);        %hold on;
```

```
%-------------------------------------------------------------------------
%% Pressure history at the thrust wall---------------------------------
P0=101325; g0=1.4014; g3= 1.1288;PCJ=PCJ_0*101325;  %from cea
ki=(g3+1)/(2*g3); kii=(g3-1)/(2*g3); kiii=ki/kii;   %from Endo
p3w=(ki^kiii/2)*(g0/g3)*MCJ^2*P0;                   %from endo
kiv= 2*((g3*ki)^kiii -1)/(g3*kii);                  %from endo
kv = 2*ki^(-kiii/2);                                %from endo
KI = kiv*((.5*g0/g3)^kii*ki^ki *MCJ^(2*kii) -1) +kv;

A= (g0*MCJ^2+g3)/(g0*MCJ^2+1);   dA2=2*(g0*MCJ^2)/(g0*MCJ^2+g3);
t_rf= t_CJ* (A*ki)^(-kiii/2) ;
% plateau region
  tplateau= t_RTE(1);
texhaust= t_RTE2(1);
tplat= linspace(0,tplateau, l);    te=KI*t_CJ;
Pw1=p3w* ones(size(tplat));         tp= 2*t_rf;
%texhaust = te;

%isentropic region
t_is = linspace(tplateau, texhaust,l);
Pw2  = p3w*(kiv*t_CJ./ ((t_is - tplateau) + kiv*t_CJ*2) ).^(1/kii);

%partial filling stagnation
t_exh2= t_SE(1);
t_pfs = linspace(texhaust, t_exh2,l);
P_pfs=Pw2(l)* ones(size(t_pfs));

%isentropic region 2
t_is2 = linspace(t_exh2, .84*t_SE2(1),l);
Pw_is2  = Pw2(l)*(kiv*t_CJ./ ((t_is2 - t_exh2) + kiv*t_CJ) ).^(1/kii);


t_Tw = [tplat t_is t_pfs t_is2];        %super position of time history
P_Tw = (1/P0)*[Pw1  Pw2 P_pfs Pw_is2];   %super position of pressure history
```

APPENDIX B

PDE-LPG Cycle Analysis MATLAB® Program

The MATLAB® program below was developed for the drawing of the proposed PDE-LPG thermodynamic p-v and T-s cycles.

```
% AbdulRaheem Bello
% 9/6/2015
% PDE-LPG Plots

clc; clear;
T1= 300; T3=2000; %Kelvin
T3=1158.4; %Kelvin Higher T result in hyperbolic shape. lower -> square
R=0.287058*1000;  % J/(kg*K) Steam (Plot shape is the smae irrespective of R)
P1=1.013*100000;%pa
V1= R*T1/P1;%m^3/kg
cpr = 10; %compressor pressure ratio
rc=2; %Cut-off ratio

clc; clear;
T1= 300; T3=2000; %Kelvin
T3=1158.4; %Kelvin Higher T result in hyperbolic shape. lower -> square
R=0.287058*1000;  % J/(kg*K) Steam (Plot shape is the smae irrespective of R)
P1=1.013*100000;%pa
V1= R*T1/P1;%m^3/kg
cpr = 10; %compressor pressure ratio
rc=2; %Cut-off ratio

%cfP = 0.25; % pressure ratio P3/P2 for carnot cycle (high#-> small PV area)
S1 = 7288.75; S3=9356.915;% J/(kg*K entropy for air with T1=300K and T3=2000K
S3=2402.09; % corrected S3 due to material limitation on T3

% Note Isentropic heat addition and isochoric heat rejection
P2=cpr*P1;  V4=V1;
S2=S1; S4=S3; ds=S3-S2;  cp1=1010; cv=718; cp_1=1010; % J/(kg K)
g=1.4; g_=g-1;  gp=g+1;

% Isentropic from 1-2
%figure()
V2=V1*(cpr)^(-1/g);         T2=T1*(cpr)^(g_/g);
V2b = linspace(V1,V2,1000); % Connect 1-2b
P2b= P1*(V1./V2b).^g;       % Connect 1-2b w/ isentropic relation.

% ZND from 2-2' and RH from 2'-3CJ
[zR,zH1, zH2, zCJ, zi, zcj,zh] = ZND_CJ(P2, T2);
V3= zCJ(1); P3= zCJ(2)*101325;  T3= zcj(1);% CJ points

S2R = zi(5);  S3 = zcj(5);
T2R = zi(1);  T3 = zcj(1); %zcj =[T_1 ,P_1, R_1, V_1,S_1, CP_1, CV_1, Mcj];
```

```
cp=zcj(6); cv=zi(7);

zR1= zR(:,1);   zR2= zR(:,2);
IR = find( zR1<V3 & zR1 > min(zH1(:,1)));
zRv = zR1(IR);   zRp = zR2(IR);

% Isentropic from 3-4 (shorter expansion due to isochoric heat rejection)
T4=T3*(V3/V4)^(g_);
V4b = linspace(V3,V4,1000); % Connect 3-4
P4b= P3*(V3./V4b).^g;       % Connect 3-4 w/ isentropic relation.

% Isochoric from 4-1
P4 = R*T4/V4;  PV1 = [V1;P1]; PV4 = [V4;P4];          PV41=[PV1,PV4];

%%%%%%%%%%%%%%%%%% Combined ZND & Carnot PV cycle
%%%%%%%%%%%%%%%%%
%T3 =720;
T4c=T1; T2c=T3; T21c=T2c/T1;
g=1.4; g_=g-1;
C1=R*T1; C3=R*T3; %J/kg Isothermal constants

 figure ()
% Isentropic from 1-2c (Using isothermal temperature ratio)
P2=P1*(T21c)^(g/g_);
V2=V1*(T21c)^(-1/g_);
%S2=S1;

V2c = linspace(V1,V2,10000); % Connect 1-2c
P2c= P1*(V1./V2c).^g;       % Connect 1-2c w/ isentropic relation.

plot(V2c,P2c,'b--'); hold on; % Isentropic graph 1-2c

% Isentropic from 3-4c (Using isothermal temperature ratio)
P4=P3*(T21c)^(-g/g_);
V4=V3*(T21c)^(1/g_);
S4=S3;

V4c = linspace(V3,V4,100000); % Connect 3-4c
P4c= P3*(V3./V4c).^g;       % Connect 3-4c w/ isentropic relation.

plot(V4c,P4c,'b--', 'linewidth', 1); hold on; % Isentropic graph 3-4c

% Isothermals
%nu1 = linspace(.01*V1,V4,1000); nu2 = linspace(V2,6*V3,1000);
nu1 = linspace(V1,V4,10000); nu2 = linspace(V2,V3,1000);
P1c=C1./nu1;
```

```
P3c=.81*C3./nu2;

plot(nu1,P1c,'r--', nu2,P3c,'r--'); hold on; % Isothermals
set(gca,'YTick',[]); set(gca,'XTick',[]); %Remove numbers on axis
xlabel('\bf \nu');  ylabel('\bf P');
axis([0 1.08*PV41(1,2) -7*P1 ( zH1(end,2)*1.05*101325)]);
% title('\bfResponse of Two mass system')
%Diesel
plot(V2b,P2b,'-k'); hold on; % Isentropic graph 1-2
plot(zH1(:,1),zH1(:,2)*101325, '-k'); hold on; % Shock from 2-2'
plot(zRv,zRp*101325, '-k'); hold on; % RH from 2'-3
plot(V4b,P4b,'-k'); hold on; % Isentropic graph 3-4
plot(PV41(1,:),PV41(2,:), '-k'); hold on; % Isobaric from 4-1

str1 = ' 1';   text(V1,P1,str1,'VerticalAlignment','top')
str2 = '2  ';   text(min(V2b),max(P2b),str2,'HorizontalAlignment','right')
str2 = '  2h';   text(min(zRv),max(zRp)*101325,str2,'HorizontalAlignment','left')
str3 = '  3';   text(V3,P3,str3,'HorizontalAlignment','left')
str4 = ' 4';   text(PV41(1,2),PV41(2,2),str4,'VerticalAlignment','bottom')

plot(min(V2b),max(P2b),'-ro','MarkerSize',2); plot(V1,P1,'-ro','MarkerSize',2);
plot(min(zRv),max(zRp)*101325,'-ro','MarkerSize',2); plot(V3,P3,'-ro','MarkerSize',2);
plot(PV41(1,2),PV41(2,2),'-ro','MarkerSize',2);


%Carnot Efficiency
nC=1-1/T21c;

%% %%%%%%%%%%%%%%%%%% ZND T-S Plot
%%%%%%%%%%%%%%%%%%%%%%
figure()
% Isentropic from 1-2b
TS1 = [S1;T1]; TS2 = [S2;T2];       TS12b=[TS1,TS2];
plot(TS12b(1,:),TS12b(2,:), '-b');hold on; % Isentropic from 1-2b

% Reactant Hugoniot from 2-2'
T2h=zh(4,:); S2h=zh(3,:);
T2He = zh(4,end);       S2He = zh(3,end);% points for 2' end
plot(S2h,T2h,'-k'); hold on; % Hugoniot from 2-2'

%  Rayleigh Heating from 2' - 3
cp

M = linspace (0.31672,1,1000);
T3r = T3*(gp./(1+g*M.^2)).^2.*M.^2;
dS3 = 0.884255*cp* log(M.^2.*( gp./(1+g*M.^2)).^(gp/g));
```

```
S3r = S3 + dS3;
T3c = max(T3r);
plot(S3r,T3r,'-k'); hold on; %Rayleigh Heating plot from 2' - 3

% Isentropic from 3-4
TS3 = [S3;T3]; TS4 = [S4;T4];       TS34b=[TS3,TS4];
plot(TS34b(1,:),TS34b(2,:), '-b');hold on;

% Isobaric from 4-1
S4b = linspace(S1,S4,1000); ds4=S4b-S1; % Connect 1-2c
cv4= ds4(end)/(log(T4/T1));
T4b= T1.*exp(ds4/cv4);       % Connect 1-2c w/ isentropic relation.
plot(S4b,T4b,'-r'); hold on; % Isentropic graph 1-2c


%% %%%%%%%%%%%%%%%%%% Carnot T-S Plot w/ ZND T-S
Plot%%%%%%%%%%%%%%%%
%figure(),clf,
% Isentropic from 1-2c
TS1 = [S1;T1]; TS2 = [S2;T3c]; TS3 = [S3;T3c]; TS4 = [S4;T1];

TS12=[TS1,TS2]; TS23=[TS2,TS3];     TS34=[TS3,TS4]; TS41=[TS4,TS1];

plot(TS12(1,:),TS12(2,:), 'b--',TS23(1,:),TS23(2,:), 'r--');hold on;
plot(TS34(1,:),TS34(2,:), 'b--',TS41(1,:),TS41(2,:), 'r--');
set(gca,'YTick',[]); set(gca,'XTick',[]);% 'box', 'off');Remove numbers on axis
xlabel('\bf S');  ylabel('\bf T');

str1 = '1  ';   text(S1,T1,str1,'HorizontalAlignment','right')
str2 = '2  ';   text(S2,T2,str2,'HorizontalAlignment','right')
str2h = '2h  ';   text(S2He,T2He,str2h,'HorizontalAlignment','right')
str3 = ' 3';   text(S3,T3,str3,'HorizontalAlignment','left')
str4 = ' 4';   text(S4,T4,str4,'HorizontalAlignment','left')

plot(S1,T1,'-ro','MarkerSize',2); plot(S2,T2,'-ro','MarkerSize',2);
plot(S2He,T2He,'-ro','MarkerSize',2);
plot(S3,T3,'-ro','MarkerSize',2); plot(S4,T4,'-ro','MarkerSize',2);

% Plot configuartions
axis([ S1-400 400+S4 T1-400 400+T3c]);

% Brayton T-S
plot(TS12b(1,:),TS12b(2,:), '-k');hold on;    % Isentropic from 1-2b
%plot(S3b,T3b,'-k'); hold on;                % Isobaric from 2-3

plot(zh(3,:),zh(4,:),'-k'); hold on;         % Hugoniot from 2-2'
```

```
plot(TS34b(1,:),TS34b(2,:), '-k');hold on;    % Isentropic from 3-4
plot(S4b,T4b,'-k'); hold on;                  % Isobaric from 4-1

%
%% %%%%%%%%%%% 1st and 2nd law efficiency for ZND as fcn(cpr)
%%%%%%%
figure()
n=100;
cpr1 = linspace(1,50,n);
% CAS efficiency
f=17.23852; %mass ratio for stoic CH4-Air
h= 1174.34; % enthalpy(heat) of rxn. from CEA for P2, T2
q=f*h/(cv4*T1);

%
gn=cp/cv4;
q=5/gn; %q=f*hpr/(Cp*T0)
hpr=q*cp*T1/f; % BackSolve
T2=T1*(cpr1).^(g_/g);

T21=T2./T1;
a =gp*(q./T21)+1;
MCJ2= a+(a.^2-1).^0.5; %MCJ^2= a+(a^2-1)^0.5
nD1 = 1 - (1./(MCJ2).*((1+g.*MCJ2)/gp).^(gp/g) -1)/q;

plot(cpr1,nD1, '-k'); hold on;

% Second law efficiency for T3 fixed at 1400 K
nD2 = nD1/nC;
plot(cpr1,nD2, '-r');
xlabel('\bf \pi_c');  ylabel('\bf \eta _Z_N_D');
legend('\bf \eta _I_-_Z_N_D','\bf \eta _I_I_-_Z_N_D', 'Location', 'east')

axis([1 50 0 1]);
```

REFERENCES

[1] Kailasanath, K., “Review of Propulsion Applications of Detonation Waves,” *AIAA Journal*, Vol. 38.9, 2000, pp. 1698–1708.

[2] Petela R., “Application of Exergy Analysis to the Hydrodynamic Theory of Detonation in Gases.” *Fuel Processing Technology*, Vol. 67, 2000.

[3] Lindstedt, R. and Michels. H., "Deflagration to Detonation Transitions and Strong Deflagrations in Alkane and Alkene Air Mixtures." *Combustion and Flame*, Vol. 76.2, 1989, pp. 169–81.

[4] Rasheed, A., Anthony H. F., and Anthony J. D., "Experimental Investigations of the Performance of a Multitube Pulse Detonation Turbine System." *Journal of Propulsion and Power*, Vol. 27.3, 2011, pp. 586–96.

[5] Camberos, J.A. and Doty, J.H., “Fundamentals of Exergy Analysis,” in *Exergy Analysis and Design Optimization for Aerospace Vehicles and Systems*, edited by Camberos, J.A. and Moorhouse, D.H., pp. 77–140, AIAA, Reston, VA, 2011.

[6] Doty, J.H., Camberos, J.A. and Moorhouse, D.J.. “Benefits of Exergy-Based Analysis for Aerospace Engineering Applications—Part I.” *International Journal of Aerospace Engineering*, Article ID 409529, 2009.

[7] Doty, J.H., Camberos, J.A. and Moorhouse, D.J., “Benefits of Exergy-Based Analysis for Aerospace Engineering Applications: Part 2,” *AIAA Paper* 2009–1598, 2009.

[8] Bejan, A., *Advanced Engineering Thermodynamics*, 3rd ed., Wiley, 2006.

[9] Bellini, R., and Lu, F.K., "Exergy Analysis of a Hybrid Pulse Detonation Power Device." *Journal of Propulsion and Power* Vol. 26.4, 2010, pp. 875–78.

[10] Wall, G., "Exergy, Life and Sustainable Development." Web. 25 Apr. 2016. http://www.exergy.se/ftp/elsd.pdf.

[11] Lee, J. H. S. *The Detonation Phenomenon. Cambridge*: Cambridge UP, 2008. Print.

[12] Zipf, R.k., Gamezo, V.n., Sapko, M.j., Marchewka, W.p., Mohamed, K.m., Oran, E.s., Kessler, D.a., Weiss, E.s., Addis, J.d., Karnack, F.a., and Sellers, D.d. "Methane–air Detonation Experiments at NIOSH Lake Lynn Laboratory." *Journal of Loss Prevention in the Process Industries,* Vol. 26.2, 2013, pp. 295-301.

[13] Friedman, R. "Kinetics of the Combustion Wave." *Journal of the American Rocket Society* Vol. 23.6, 1953, pp. 349-54.

[14] Gavrikov, A.i., Efimenko, A.a., and Dorofeev, S.b., "A Model for Detonation Cell Size Prediction from Chemical Kinetics." *Combustion and Flame, Vol.*120.1-2, 2000, pp. 19-33.

[15] Denisov, Yu.N., and Troshin, Ya.K., "Structure of Gaseous Detonation in Tubes." *Sov. Phys. Tech. Phys*., Vol. 5.4, 1960, pp. 419-431.

[16] Guirao, C.M., Knystautas, R., Lee, J., Benedick, W., and Berman, M., "Hydrogen-Air Detonations." *In 19th Symp. Int. Combust. Proc.*, 1982, pp. 583-590.

[17] Bauer, P., "Contribution a l'etude de la Detonation des Melanges Explosifs Gazeux a Pression Initiale Elevee." *PhD thesis, Universite de Poitiers,* 1985.

[18] Moen, I.O., Funk, J.W., Ward, S.A., Rude, G.M., and Thibault, P.A. "Detonation Length Scales for Fuel-Air Explosives." *In Prog. Astronaut. Aeronaut*. Vol. 94, 1984, pp. 55-79.

[19] Peraldi, O., Knystautas, R., and Lee. J.h. "Criteria for Transition to Detonation in Tubes." *Symposium (International) on Combustion,* Vol. 21.1, 1988, pp. 1629-637.

[20] Bello, R., “High-Enthalpy Characterization of the UTA Hypersonic Shock Tunnel,” *Masters’ thesis, University of Texas at Arlington*, 2013.

[21] Li, J., Lai, W.h., Chung, K., and Lu, F.k., "Experimental Study on Transmission of an Overdriven Detonation Wave from Propane/oxygen to Propane/air." *Combustion and Flame* Vol. 154.3, 2008, pp. 331-45.

[22] Roy, G.D., Frolov, S.M., Borizov, A.A. and Netzer, D.W., “Pulse Detonation Propulsion: Challenges, Current Status, and Future Perspective,” *Progress in Energy and Combustion Science*, Vol. 30.6, 2004, pp. 545–717.

[23] Kailasanath, K., “Recent Developments in the Research on Pulse Detonation Engines.” *AIAA Journal*, Vol. 41.2, 2003, pp. 145-159.

[24] Kasahara, J., Akira, H., Toyoshi N., Hiroyuki, Y., Takashi Y., and Takayuki, K. "Thrust Demonstration of a Pulse Detonation Rocket "TODOROKI"" 43rd *AIAA/ASME/SAE/ASEE Joint Propulsion Conference & Exhibit* (2007).

[25] Barr, L., "Pulsed Detonation Engine Flies into History." *Pulsed Detonation Engine Flies into History. 88th Air Base Wing Public Affairs*, 15 May 2008. Web. 25 Apr. 2016. http://www.afmc.af.mil/news/story_print.asp?id=123098900

[26] Bussing, T., “Pulse Detonation Electrical Power Generation Apparatus with Water Injection.” *U.S. Patent No*. 6,062,018. May 16, 2000.

[27] Lu. F.K., Wilson, D.R., “Scalable Power Generation Using a Pulsed Detonation Engine.” *U.S. Patent No*. 7,340,903. March 11, 2008.

[28] Panicker, P.K., Lu, F.K., Chui, K.F., New, T.H., and Tsai, H.M., “Experimental Study on Deflagration-to-Detonation Enhancement Methods in a PDE,” *AIAA Paper* 2006–7958, 2006.

[29] Cambier, J.L., Tegner, J., "Strategies for PDE Performance Optimization." *33rd Joint Propulsion Conference and Exhibit* (1997).

[30] P. Panicker, "The Development and Testing of Pulsed Detonation Engine Ground Demonstrators," *PhD Dissertation, University of Texas at Arlington*, 2008.

[31] Sato, S., Akiko M., Endo, T., and Kasahara, J., "Numerical Studies on Specific Impulse of Partially Filled Pulse Detonation Rocket Engines." *Journal of Propulsion and Power,* Vol. 22.1, 2006, pp. 64-70.

[32] Endo, T., Tomoaki Y., Shiro T., Akiko M., Inaba, K. and Kasahara. J., "Homogeneous-Dilution Model of Partially Fueled Simplified Pulse Detonation Engines," *Journal of Propulsion and Power*, Vol. 23.5, 2007, pp. 1033–1041.

[33] Braun, E., Lu, F., Sagov, M., Wilson D., and Grubyi, P., "Proof-of-Principle Detonation Driven, Linear Electric Generator Facility", *Joint Propulsion Conference & Exhibit*, 2010.

[34] Chapman, S.J., *Electric Machinery and Power System Fundamentals*. Boston: McGraw-Hill, 2002. Print.

[35] Polinder, H., Mecrow, B.c., Jack, A.g., Dickinson, P.g., and Mueller, M.a., "Conventional and TFPM Linear Generators for Direct-Drive Wave Energy Conversion." *IEEE Transactions on Energy Conversion IEEE Trans*. *On Energy Conversion*, Vol. 20.2, 2005, pp. 260-67.

[36] Blarigan, P.V., "Advanced Internal combustion Electrical Generator", *Proceed of the 2001 DOE Hydrogen Program Review*, NREL/CP-570-30535, Sandia National Laboratories Livermore, CA 94550.

[37] Kentfield, J.A.C., “Thermodynamic Cycle Analysis of Pulse Detonation Engine,” *Journal of Propulsion and Power*, Vol. 18.1, 2002, pp. 68–76.

[38] Hutchins, T.E., and Metghalchi, M., “Energy and Exergy Analyses of the Pulse Detonation Engine,” *Journal of Engineering for Gas Turbines and Power*, Vol. 125.4, 2003, pp. 1075–1080.

[39] Heiser, W.H., and Pratt, D.T., “Thermodynamic Cycle Analysis of Pulse Detonation Engine,” *Journal of Propulsion and Power*, Vol. 18.1, 2002, pp. 68–76

[40] Maeda, S., Kasahara, J., Matsuo, A., and Endo. T., "Analysis on Thermal Efficiency of Non-Compressor Type Pulse Detonation Turbine Engines." *Trans. Japan Soc. Aero. S Sci.* Vol. 53.181, 2010, pp. 192-206.

[41] Sakurai, T., and Yuasa, S., "Development of a Hydrogen-fueled Pulse Detonation Combustor for 1 KW-class Micro Gas Turbine." *46th AIAA/ASME/SAE/ASEE Joint Propulsion Conference & Exhibit* (2010).

[42] Moran, M.J. *Availability Analysis: A Guide to Efficient Energy Use.* New York: ASME, 1989. Print.

[43] Craig, R.R., Kurdila, A., *Fundamentals of Structural Dynamics*. Hoboken, NJ: John Wiley, 2006. Print

[44] Landau, L.D., and Lifshitz, E.M., “The Propagation of a Detonation Wave.” *Fluid Mechanics, Pergamon*, 1979, pp. 487–293.

[45] Moran, M.J., and Shapiro, H. N., *Fundamentals of Engineering Thermodynamics*. New York: Wiley, 2000. Print.

[46] Strehlow, R. A., *Combustion Fundamentals*, McGraw–Hill, New York, 1984, pp. 127–138, 302–307.

[47] Shapiro, A. H., *The Dynamics and Thermodynamics of Compressible Fluid Flow*, Ronald, New York, 1953, pp. 193–211.

[48] Joshi, D.D., and Lu, F.K., "Unsteady Thrust Measurement for Pulse Detonation Engines." *Journal of Propulsion and Power,* Vol. 32.1, 2016, pp. 225-36.

[49] McBride, B.J., and Gordon, S., "Computer Program for Calculation of Complex Chemical Equilibrium Compositions and Applications Analysis (CEA)," Cleveland, OH, Oct. 1994.

[50] AFS Global, "Gs Series Injector Installation Guide AFS Document No . 50-01199-01," 2008.

[51] Joshi, D.D., "Unsteady Thrust Measurement Techniques for Pulse Detonation Engines," *Ph.D. dissertation, University of Texas at Arlington*, 2014.

[52] "LT1010 - Fast 150mA Power Buffer - Linear Technology." Web. 08 Apr. 2016. http://www.linear.com/product/LT1010.

[53] Linmot, *LinMot_Data_Book_e_recent*, LinMot, USA, 2014, pp. 70

[54] Colombo, P., and Rossetto, L., "Analysis and Design of a Linear Tubular Electric Machine for Free-piston Stirling Micro-cogeneration Systems", 2014.

BIOGRAPHICAL INFORMATION

Raheem Bello was born in Lagos, Nigeria. He was inspired to study astronomy from gazing at the night sky, and aspired to become an astronaut. In February 2006, he moved to the U.S. and resumed at Westbury High School in Houston in the 9th grade. He graduated in spring 2008, and enrolled in college at University of Texas at Austin. At UT Austin, He worked in the magnetism and superconductivity group for 2 years studying "Thermal conductivity due to magnon heat transport." He graduated from UT Austin in spring 2012 with a Bachelor of Science in Astronomy and a Bachelor of Science in Physics with honors. He enrolled at University of Texas at Arlington in Fall 2012, and conducted research at the Aerodynamics Research Center (ARC). He later earned a MSc. in Aerospace Engineering in December 2013. He began his PhD program in Spring 2013. He hopes to focus on commercializing detonation engine technologies in order to help enable a world of abundance.